INFORMATION TO USERS

The most advanced technology has been used to photograph and reproduce this manuscript from the microfilm master. UMI films the text directly from the original or copy submitted. Thus, some thesis and dissertation copies are in typewriter face, while others may be from any type of computer printer.

The quality of this reproduction is dependent upon the quality of the copy submitted. Broken or indistinct print, colored or poor quality illustrations and photographs, print bleedthrough, substandard margins, and improper alignment can adversely affect reproduction.

In the unlikely event that the author did not send UMI a complete manuscript and there are missing pages, these will be noted. Also, if unauthorized copyright material had to be removed, a note will indicate the deletion.

Oversize materials (e.g., maps, drawings, charts) are reproduced by sectioning the original, beginning at the upper left-hand corner and continuing from left to right in equal sections with small overlaps. Each original is also photographed in one exposure and is included in reduced form at the back of the book. These are also available as one exposure on a standard 35mm slide or as a 17" x 23" black and white photographic print for an additional charge.

Photographs included in the original manuscript have been reproduced xerographically in this copy. Higher quality 6" x 9" black and white photographic prints are available for any photographs or illustrations appearing in this copy for an additional charge. Contact UMI directly to order.

U·M·I

University Microfilms International
A Bell & Howell Information Company
300 North Zeeb Road, Ann Arbor, MI 48106-1346 USA
313/761-4700 800/521-0600

Order Number 9000043

The universality of kinetic colloid aggregation

Lin, Min Yue, Ph.D.

City University of New York, 1989

U·M·I
300 N. Zeeb Rd.
Ann Arbor, MI 48106

THE UNIVERSALITY OF KINETIC COLLOID AGGREGATION

by

MIN YUE LIN

A dissertation submitted to the Graduate Faculty in Physics in partial fulfillment of the requirements for the degree of Doctor of Philosophy, The City University of New York.

1989

This manuscript has been read and accepted for the Graduate Faculty in Physics in satisfaction of the dissertation requirement for the degree of Doctor of Philosophy.

January 1987 — Date

Chair of Examining Committee

January 1987 — Date

Executive Officer

Dr. D. A. Weitz

Prof. H. Z. Cummins

Prof. M. Lax

Prof. M. Sarachik

Prof. A. Genack

Supervisory Committee

The City University of New York

To My Family

Abstract

THE UNIVERSALITY OF KINETIC COLLOID AGGREGATION

by

Min Yue Lin

Adviser: Dr. David A. Weitz

In this thesis the process of kinetic colloid aggregation is studied. We show that the structure of colloidal aggregates can be quantitatively described as *fractals*. Two kinetic regimes have been identified as universal regimes, each of them exhibits different yet distinct behavior in many key features: the fractal dimension, the cluster mass distribution, and aggregation kinetics.

Using colloidal gold, the fractal dimension and the cluster mass distribution are measured by transmission electron microscopy (TEM) analysis and scattering techniques. For DLCA, $d_f \approx 1.85$, the cluster mass distribution exhibits a bell shape. For RLCA, $d_f \approx 2.1$, and the cluster mass distribution has a power–law dependence $N(M) \sim M^{-3/2}$. For both regimes the cluster mass distribution obeys dynamic scaling. These properties are further studied and verified using light scattering techniques. Static light scattering is used to probe the fractal structure of aggregates, thus measuring the fractal dimension, d_f. In addition, it is used to probe

and verify the static structure factor of the aggregates. Dynamic light scattering is used to verify these key features of the aggregation process, including also the anisotropy of the aggregates reflected in the effects of their rotational diffusion, and the aggregation kinetics. Excellent agreement is found between the scattering results and the predictions based on the previous finding from colloidal gold. In addition, the aggregation kinetics measured are distinct for the two regimes: for DLCA, the characteristic cluster mass grows linearly with time; for RLCA, it grows exponentially.

A method is developed to scale dynamic light scattering data onto a master curve, whose shape depends critically on these key features, but is independent of the specific details of the colloid system. It is therefore used to demonstrate the universality of colloid aggregation. For several completely different colloids the master curves from the two regimes are markedly different; however, for each regime they are strikingly identical for these colloids. In addition, static light scattering also measures the same fractal dimension from the colloids for each regime. This provides strong evidence for the universality of the two regimes of colloid aggregation, and proves the successful application of the modern statistical theories of kinetic growth.

Acknowledgements

I wish to acknowledge many people who have helped and encouraged me during the preparation of the thesis, as well as during my thesis research at the Exxon Corporate Research labs and my graduate course work at the City College of New York. Dr. Dave Weitz, who is my thesis advisor, taught me not only how to grab the Physics, but also to write scientific English correctly. I have enjoyed collaborating with Drs. H. M. Lindsay, J. S. Huang, R. C. Ball, P. Meakin, C. J. Sandroff, and Prof. R. Klein during various periods of my thesis research. I also wish to thank Drs. T. A. Witten, S. K. Sinha, H. W. Deckman, and J. P. Stokes, and Profs. D. Pine and P. M. Chaikin for many fruitful discussions, suggestions and encouragement.

In 1984, it was not at all easy for me, a Mainland Chinese student, to come to an industrial lab like Exxon to do thesis research. Dave certainly helped, because he likes to work with and teach students. Thanks also go to Profs. M. Sarachik and M. Arons, then the Graduate Advisor and Department Chairman at CCNY, who encouraged and supported the idea of carrying out my thesis work at Exxon. At Exxon, I want to thank Dr. A. N. Bloch, who was then the Group Leader and later Lab Director. I thank J. Dunsmuir, D. P. Goshorn, M. S. Alvarez and J. Sung for many technical assistances. I appreciate the financial support from the City College, the City University of New York, and Exxon Research and Engineering Company.

I would like to thank the faculty of the Physics Department of CCNY. Especially, I want to thank the members of my dissertation committee, among

whom are Prof. H. Z. Cummins, who taught me Solid State Physics, Prof. J. Gersten, who taught me E&M, and Prof. M. Lax, who taught me Quantum Optics.

Finally, I should acknowledge my indebtedness to my wife, Zhenhong Li, for her patience, selfless care and encouragement. Without these my life would be rather miserable.

New York, New York
Annandale, New Jersey
December, 1988

CONTENTS

List of Tables

List of Figures

CHAPTER 1

INTRODUCTION

Kinetic aggregation has historically been one of the most widely studied subjects within colloid science, as it represents a problem in classical statistical physics of fundamental interest as well as a widely exploited phenomenon of great technological importance. However, there are many new developments in recent years that have lead to significant advances in our understanding of kinetic aggregation, and have spawned a revival of interest in the field. These developments are closely related to recent work in the statistical physics of random kinetic growth processes, of which colloid aggregation is a prime example. The key to these advances is the recognition that the random, tenuous clusters that are produced when colloids aggregate have a well–defined symmetry, as their structure remains invariant under a change in length scale. This is called dilation symmetry, and objects that possess it are called fractals.[1] Hence, the structure of colloidal aggregates can be quantitatively characterized, despite their very random and disordered appearance, thus resolving one of the major problems that had limited the study of kinetic colloid aggregation. Knowledge of the structure now makes it possible to determine the physical properties of the aggregates as they grow, as well as their mutual interactions which determine the growth process itself. Furthermore, the study of colloid aggregation represents one of the major applications, and experimental tests, of the modern statistical theories of kinetic growth.

Since colloid aggregation is a kinetic, non–equilibrium growth process, the structure of the aggregates is inherently related to the kinetics of the aggregation, which in turn, is reflected by the time evolution of the cluster mass distribution. The traditional technique to describe the aggregation kinetics and the shape of the cluster mass distribution has been the use of a coupled set of integrodifferential rate equations, commonly known as the generalized Smoluchowski equations.[2] The utility of these equations to describe colloidal aggregation can now be substantially extended using our ability to characterize the structure of the colloidal aggregates. In addition, a second concept of modern statistical physics, that of dynamic scaling, or the invariance of the form of the solution in time, can be successfully applied to the description of colloid aggregation in terms of the Smoluchowski equations.

In this volume, we present a detailed study of how these modern concepts of statistical physics can be used to greatly improve our understanding of colloid aggregation. Our emphasis is on those features of the aggregation process that are universal, rather than the details of the specific surface chemistry that also plays a significant role in the stabilization of many colloidal systems. Thus, we first study a prototypic colloid system, aqueous gold colloids, for which we are able to both monitor and control the surface chemistry. We show that the aggregates that are formed are indeed well described as fractals whose structure is intrinsically related to the aggregation kinetics. These kinetics can be divided into two limiting kinetic regimes, determined by the details of the interparticle interactions which in turn control the sticking probabilities for two colliding clusters. These limiting regimes represent two universal classes of kinetic aggregation. In one case, the clusters stick immediately upon contact, so that the aggregation is extremely fast, limited only by the diffusion of the clusters. In the other case the aggregation is very slow because there is a considerable energy barrier which prevents the clusters from actually sticking to each other when they collide. The resultant clusters produced in each

regime have distinctly different structures, with different fractal dimensions. We show that each regime results in a distinct cluster mass distribution, which exhibits dynamic scaling. In both cases, we are able to model the aggregation kinetics in a relatively simple fashion, and can determine the appropriate description of the cluster interactions for use in Smoluchowski equations. These two universal regimes appear to be sufficient to describe all the regimes of the homogeneous aggregation of colloid systems.

Light scattering has been widely and successfully used in studying the structure of the colloidal aggregates, and their dynamics. In this volume, we present a detailed description on how static and dynamic light scattering results are related to the behavior of colloidal aggregates and the aggregation process. We show that while static light scattering can be successfully used to measure the fractal dimension, it is also sensitive to the finite size effects of the aggregates—how their fractal structure is bounded, when their size is comparable to the inverse of the scattering wavevector, q^{-1}. When their size is larger than q^{-1}, dynamic light scattering can probe their structure anisotropy, reflected in the effects of rotational diffusion. By properly including these effects and the effects of the cluster mass distribution, our predictions are in excellent agreement with the light scattering measurements for both regimes.

We also present an experimental demonstration of the universality of colloid aggregation. Since light scattering is a sensitive measure of many key features of the aggregation process, a technique is developed to use light scattering to compare the behavior of completely different colloids. We show that by taking advantage of the dynamic scaling of the cluster mass distribution and the scaling properties of the fractal aggregates, we can scale the dynamic light scattering data onto a single master curve. The shape of the master curve depends critically on the details of the aggregation process, including the aggregate structure, the cluster mass distribution,

and the aggregation kinetics, but not on any specific colloid system. We show that the master curves for the two regimes exhibit distinct shapes. Therefore master curves from entirely different colloids can be directly compared to critically evaluate the proposed universality of the aggregation processes.

To test the universality of colloid aggregation, we measure the behavior of three completely different colloidal systems: gold, silica and polystyrene latex. Each colloid can be made to aggregate either very rapidly, under diffusion–limited kinetics, or very slowly, under reaction–limited kinetics. We demonstrate that the behavior for each colloid is identical in each of the two limiting regimes. In each regime, the master curves for the colloids are indistinguishable. In each regime, the fractal dimensions of the aggregates are identical. In each regime, the aggregation kinetics for the colloids are the same. These results provide convincing experimental evidence proving that colloid aggregation is a universal process.

The work presented in this thesis shows that it is both possible and fruitful to apply the concepts of fractals and scaling to kinetic aggregation and demonstrates some of the techniques and methods that greatly take advantages of these concepts. The ability to quantitatively characterize the structure of the aggregates makes it possible to describe their physical properties, as well as other effects of their environment, on their structure. Furthermore, since colloid aggregation is a universal phenomenon, the results obtained in studying one colloid can be similarly applied to a wide range of colloid systems.

The remainder of this volume is structured as follows. Chapter 2 provides a review of both historic and and modern approaches to the understanding of kinetic colloid aggregation. We also present some basic evidences of the fractal nature of colloidal aggregates. In addition, experimental details for the whole volume are discussed.

Chapter 3 presents the results of the cluster mass distributions measured

using colloidal gold aggregates for both DLCA and RLCA regimes. We demonstrate the dynamic scaling behavior of the distributions, and discuss its consequences.

Chapter 4 is a study of static light scattering from colloidal aggregates. A detailed description on how to probe the static structure factor of individual aggregates with polydispersity present is given. For each regime, a form for the structure factor is shown to best describe the experimental observations. In addition, an experimental result using static light scattering to demonstrate the restructuring of the fractal aggregates under external stress is presented.

Chapter 5 and 6, each devoted to one regime, DLCA and RLCA, present our study of colloid aggregation and its universality using both static and dynamic light scattering. We give a detailed, self–consistent description on how the behavior of colloid aggregation is observed using the scattering techniques, and compare our predictions with experimental measurements. We then show how a master curve can be obtained from calculation and from experimental data. For RLCA, we emphasize that the power–law cluster mass distribution plays an important role in dynamic light scattering, and the shape of the master curve can be specifically used to determine the distribution exponent. For DLCA, while the effects of the cluster mass distribution is relatively minimal, we show that rotational diffusion of the aggregates plays an important role in the scattering measurements. We then present the experimental measurements for three different colloids, which provide convincing evidences for the universality of the two regimes of colloid aggregation.

REFERENCES

[1]B. B. Mandelbrot, *The Fractal Geometry of Nature* (Freeman, San Francisco, 1982).

[2]M. von Smoluchowski, *Phys. Z.* 17, 593 (1916).

CHAPTER 2

BACKGROUND AND EXPERIMENTAL DETAILS

ABSTRACT

We review traditional and modern approaches to the understanding of kinetic colloid aggregation. We present some basic experimental measurements of the fractal dimension of colloidal aggregates. Two limiting regimes of colloid aggregation are introduced: diffusion–limited (DLCA) and reaction–limited colloid aggregation (RLCA). Colloidal gold, which is used as a prototypic colloid system in our experiments, and two other colloids also used, are introduced and described. The methods of aggregating them in both regimes are discussed. In addition, the experimental details of transmission electron micrography (TEM) and light scattering are described.

2.1 COLLOID AGGREGATION: TRADITIONAL APPROACH

The key to the traditional understanding of both colloid stability and colloid aggregation is the determination of the energy of interaction between two colloidal particles as a function of their center–to–center separation. We consider the important case of aqueous colloids, consisting of identical spherical particles of radius a. The theory for the energy of interaction was developed over 40 years ago and has come to be known as the Derjaguin–Landau–Verwey–Overbeeck, or DLVO, theory,[1] and is illustrated schematically in Fig. 2.1. The energy diagram shown results from the sum of three separate forces. At the shortest distances, there is the hard sphere repulsion which prevents the particles from coming closer than $r=2a$ and occupying the same region of space. At slightly larger distances there is an attractive potential well that results from the van der Waals attraction between two particles, but can be augmented by any chemical bonds formed when the two particles touch. The repulsive energy at larger separations is caused by the Coulombic repulsion between the charges on the surface of the particles which is screened by the counterions in solution. The resultant energy barrier is the origin of the stability of the colloid against aggregation. We represent its height as E_b and its width, which is the familiar Debye–Huckel screening length, as κ^{-1}. In a diffusion–induced collision two particles will approach to within $\sim \kappa^{-1}$, but will only overcome the energy barrier and stick together with a probability $P \sim \exp(-E_b/k_BT)$ where k_B is Boltmann's constant and T is the temperature. Thus, a stable colloid requires $E_b >> k_BT$. We note that while we consider only aqueous colloids here, the form of the interaction potential can be applied to most colloidal systems, although it will be caused by interactions specific to the particular system.

Aggregation occurs when the height of the energy barrier, E_b, is reduced. For aqueous colloids, this has traditionally been accomplished by adding electrolyte to the solution, thereby increasing the screening of the surface charge and reducing

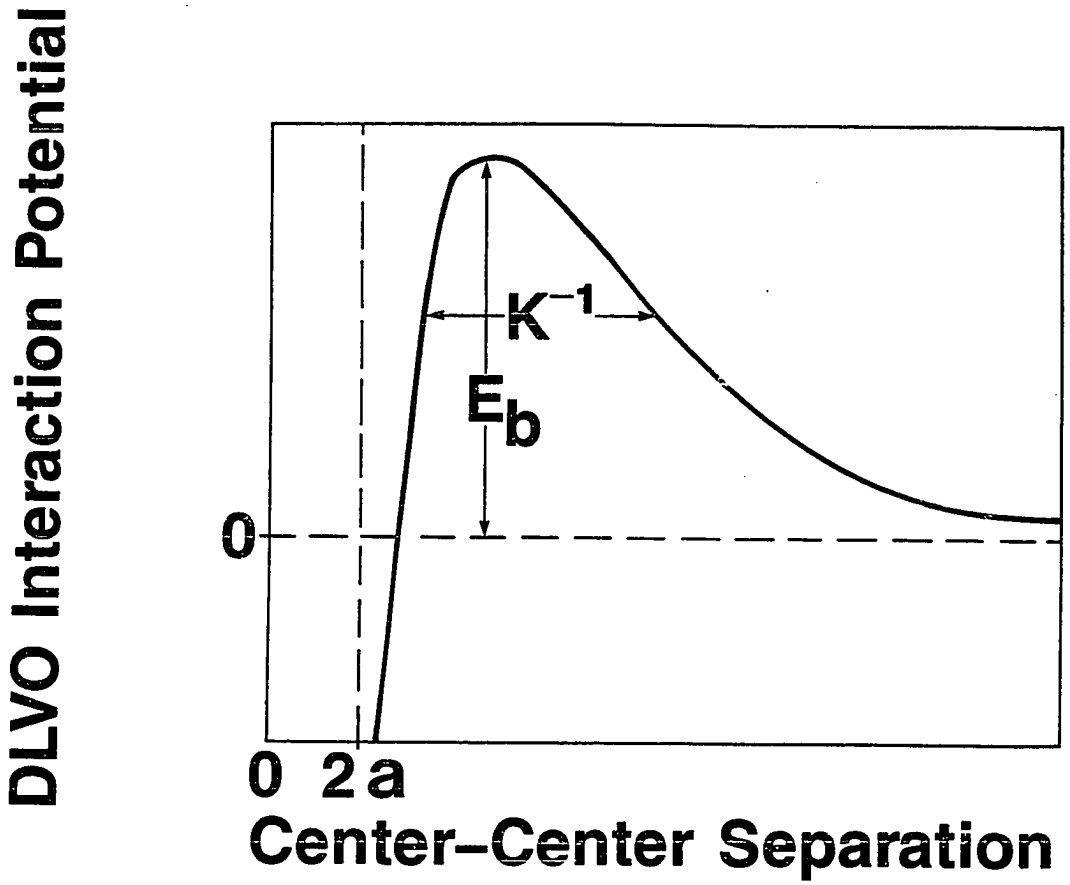

Fig. 2.1 The potential energy between two spherical colloidal particles as a function of their separation as predicted by the DLVO theory. The energy barrier E_b leads to a stabilization of the colloids, while the screening length, κ^{-1}, determines the range of the repulsive interaction. Initially, for the gold colloids, $E_b >> K_B T$, while $\kappa^{-1} \sim 2a$.

κ^{-1}. If E_b is reduced to much less than k_BT, very rapid aggregation results, limited only by the diffusion of the particles leading to their collisions. If, on the other hand, E_b remains comparable to or larger than k_BT, the aggregation rate is reduced, and slow coagulation results. The initial aggregation rate can be determined by calculating the flux of diffusing particles onto a given colloidal particle, which is also allowed to move, in the presence of the interparticle interaction energies.[1] This rate determines a characteristic time, t_0, for the aggregation process. When $E_b = 0$, $t_0=(8\pi DaN_0)^{-1}$ where D is the diffusion constant of the particles and N_0 is their concentration. As E_b increases, this characteristic time is also increased by an amount that is called the stability factor $W\sim\exp(E_b/k_BT)$, and reflects the increased repulsive barrier.[1] Much of the traditional discussion of colloid aggregation is in terms of the stability factors.[2] In particular, the DLVO theory has been reasonably successful in accounting for the effect on W of some of the parameters which control aggregation.[3]

While this approach can be used to determine the initial rate of aggregation, the subsequent aggregation kinetics are more complicated as the clusters themselves also diffuse and grow. In order to follow the statistics of this process, the traditional approach has been to use a set of rate equations or the generalized Smoluchowski equations.[4] These equations express the time (t_a) evolution of the cluster mass distribution, $N_i(t_a)$, and can be written as

$$\frac{dN_i}{dt_a} = \frac{1}{2}\sum_{j=1}^{i-j} K_{j,i-j}\, N_j N_{i-j} - \sum_{j=1}^{\infty} K_{ij}\, N_i N_j, \qquad (2.1)$$

Here, N_i is the number of clusters of mass i while the kernel of the equations, K_{ij}, reflects the rate of aggregation of a cluster of mass i with one of mass j. The first term on the right–hand side is simply the rate of formation of clusters of mass i due to the aggregation of two smaller clusters of the appropriate mass, while the second term is the rate of loss of clusters of mass i due to their aggregation to form yet

larger clusters. The key to the use of these equations is the determination of the kernel, K_{ij}. At the very early stages, K_{ij} is simply obtained from the solution of the diffusion equation for the flux of particles onto a single diffusing sphere as was discussed above. Thus, when $E_b=0$, $K_{ij}=4\pi(D_i+D_j)(R_i+R_j)$, which was in fact first determined by Smoluchowski himself. While this kernel results in reasonably good agreement with experiment for rapid aggregation, the extension of these equations to describe slow aggregation by attempting to include the stability factor has been considerably less successful in accounting for experimental observations.[3]

The most glaring deficiency of the traditional approach to colloid aggregation has been the lack of a description of the structure of the aggregates. This has precluded any successful extension of the theory to later times in the aggregation process. It is just this deficiency that the modern approach has addressed.

2.2 COLLOID AGGREGATION: MODERN APPROACH

The modern approach to colloid aggregation has been specifically concerned with the structure of the aggregates, and has tried to account for the fluctuations that produce the highly disordered structure of the aggregates. Thus, computer simulation has been a primary theoretical technique. In fact, much of the current interest was stimulated by a computer simulation by Witten and Sander[5] who considered a growing cluster to which new particles were added, one at a time. Each particle underwent random diffusion until it touched the cluster, whereupon it was permanently added at the point of contact. The resultant cluster was found to possess dilation symmetry. Although this model is important for many other kinetic growth processes, it is unlikely to find widespread importance in applications to colloid aggregation. More realistic models allow the clusters themselves to diffuse via Brownian motion and growth occurs when two clusters aggregate. These cluster–cluster aggregation models are a better representation of the actual

experimental situation in colloid aggregation.[6,7]

To date, most of the emphasis of the theoretical work has been on the structure of the clusters that result.[8] The most significant conclusion of this work is that the aggregates appear universally to possess dilation symmetry. There are two natural length scales that can be associated with each aggregate, the radius of the individual particles, a, and the size of the whole cluster, R. However, between these two length scales, $a<r<R$, the dilation symmetry means that there are no other characteristic lengths and that, in a statistical sense, the structure of the aggregates is invariant under a change of length scale. As an immediate consequence, the mass of the clusters scales with their characteristic size as $M \sim R^{d_f}$, where the fractal dimension, d_f, is typically not an integer and is less than the Euclidean dimension of space, d, in which the aggregate is embedded. In addition, the mass–mass correlation function within the cluster also exhibits power law behavior, $g(r) \sim r^{-\alpha}$ where $\alpha = d - d_f$. Thus, the fractal dimension of the clusters offers a quantitative characterization of their structure, and allows us to distinguish rather subtle differences which can result from different types of aggregation. All the computer models use simple, well defined rules to determine the type of motion, or trajectory, of the clusters, as well as the fashion by which the clusters stick to one another. A fairly large variety of situations has been investigated, providing a reasonable degree of insight into the aggregation process. The computer simulations emphasize the random fluctuations which are the key to the highly disordered structures formed in kinetic aggregation. However, to date very little analytic theory has been developed to explain the origin of the dilation symmetry which the aggregates possess. Indeed, this is one of the outstanding theoretical challenges in our current understanding of kinetic aggregation.

Since the aggregation process is inherently kinetic, the structure of the aggregates is intrinsically related to the dynamics of their formation. The dynamics

have been studied through computer simulations of the time evolution of the cluster mass distribution, $N_i(t_a)$. The results suggest that the generalized Smoluchowski equations, which are a mean–field approximation in that they average over spatial fluctuations in the concentration, give a reasonable representation of the behavior of $N_i(t_a)$ predicted by the computer simulations.[9-12] This result is perhaps somewhat surprising, given the importance of the local concentration fluctuations in determining the exact structure of the highly disordered aggregates, and suggests that, when averaged over a large number of clusters, the aggregation rate or kernel, K_{ij}, approaches some scaling form with the mass of the clusters. The details of the form of K_{ij}, and its intrinsic dependence on the fractal structure of the aggregates, as well as their mutual interactions, must be determined for each type of kinetic aggregation of interest. This is the key to the use of the rate equations to properly describe the dynamics.

The success of the Smoluchowski equations in describing the dynamics of the aggregation has also stimulated a resurgence of interest in their solutions. Both computer simulations[13] and analytic approximations[14,15] have been employed to solve these equations for a wide variety of kernels. Of particular interest is the realization that the solutions of the Smoluchowski equations can exhibit dynamic scaling for many kernels. Thus, the solutions can be reduced to a single function,

$$N_i(t_a) = s^2 \psi(i/s) \tag{2.2}$$

Here $\psi(x)$ is this scaling function and $s(t_a)$ represents some average mass which reflects the time dependence of the cluster mass distribution. Physically, the existence of this type of solution implies that the shape of the distribution has reached a steady–state form, independent of the initial conditions. The existence of such a scaling solution is not entirely new, as it was predicted by Freidlander[16] about twenty years ago for a particular form of K_{ij}, the Smoluchowski diffusion kernel.

A fundamental goal of the experiments reported in this thesis is to investigate the application of these modern theoretical concepts to colloid aggregation. Thus, we illustrate how the structure of the aggregates can be characterized as a fractal and how the fractal dimension can be quantitatively determined. We also study the effect of the kinetics of the aggregation on this structure and on the fractal dimension. Since the actual kinetics are described by the Smoluchowski equations, we measure the time evolution of the cluster mass distribution to determine the appropriate kernel, and present simple arguments to account for the observed scaling. Furthermore, we show that scaling behavior plays a key role in light scattering experiments, so that the scattering results can be used to critically evaluate many key features of the aggregation process, as well as to compare the behavior of different colloids.

2.3 COLLOID SYSTEMS

Colloidal gold is one of the most traditional and widely studied of all colloids. It is distinguished by its very deep, wine–red color, which is caused by an optical resonance within the metallic particles, resulting in the very strong absorption of green light. Upon aggregation, the electromagnetic interactions between these resonances cause them to be shifted to lower energies, with the result that the color changes dramatically, from wine–red to blue. This provides a clear and simple method for monitoring, at least qualitatively, the aggregation.

Colloidal gold has a long history. It was known to alchemists at least as far back as the twelfth century, and its wine–red color prompted its widespread use in stained glass windows, a use that continues to this day. The first scientific study of colloidal gold was done by Faraday[17] over 100 years ago, and these experiments were instrumental in the establishment of the discipline of colloid science. The explanation of the color of colloidal gold in terms of an optical resonance was one of

the initial successes of the theory, due to Mie, for the scattering of light from small metallic or dielectric particles.[18] The original development[19] by Smoluchowski of the equations that now bear his name was also inspired by observations of the aggregation of gold colloids.[20] Many of the concepts of colloid stability predicted by the DLVO theory were tested using colloidal gold. With development of the transmission electron microscope (TEM), more detailed study of the properties of small metallic colloids became feasible, and colloidal gold was one of the first and most widely studied examples.[21] More recently, colloidal gold has found widespread application as a marker material for TEM studies of biologically important samples.[22] Finally, the unique optical properties of colloidal gold have been re–examined when it was discovered that the Raman scattering cross section of molecules on the surface of the particles is anomalously enhanced.[23] Indeed, the surface–enhanced Raman scattering (SERS) exhibited by molecules adsorbed on the particle surface can be used to monitor the changes in the surface chemistry and thereby determine the effects of this on the aggregation properties.[24]

We draw heavily on the large body of knowledge that has been accumulated for colloidal gold, both for the preparation of the colloid, as well as for the control of its aggregation properties. We follow a recipe due to Turkevich to make the colloids.[25] 5 ml of a 10^{-3} M sodium tetrachloroaurate solution is mixed with 90 ml of water and heated to 90^{o}C for ~5 minutes. To this, 5 ml of a 0.05% (by weight) solution of sodium citrate is added while stirring vigorously. The mixture is then kept at 90^{o}C for 30 minutes while constantly stirring. During the first 10~15 minutes, the citrate reduces the gold, and the colloid undergoes a series of changes in color, finally attaining its characteristic wine–red color. It is necessary to keep the colloids at 90^{o} for another 15~20 minutes to ensure an even distribution of the surface charges on the particles. The colloids thus produced are extremely stable and very reproducible in their properties. The particles are reasonably spherical in

shape and highly uniform in size. The average radius of the particles is 7.5 nm with an rms deviation about the mean size[25] of roughly 10%. The concentration is about 1.7×10^{12} particles/cc.

Colloidal gold prepared in this way is initially very stable against aggregation because citrate ions, which have a negative charge of 3, are adsorbed on the surface of the gold particles. The screening length of the solution as prepared is $\kappa^{-1} \sim 10$ nm, or roughly one particle radius. The surface potential of these gold colloids has been measured[25] to be ~25 mV, and we estimate that $E_b > 18 k_B T$, thus the colloid remains stable almost indefinitely. Aggregation can be induced by the addition of electrolyte. For a monovalent counterion, the critical concentration, or the onset of the diffusion–limited regime where E_b is reduced to much less than $k_B T$, is about 10^{-2} M. However, the use of salt seems to result in somewhat anomalous behavior when the stability factor, or time of aggregation, is determined as a function of salt concentration.[25] This may be due to the fact that the salt ions also adsorb on the surface of the gold particles, resulting in two competing effects. The addition of the electrolyte collapses the double layer, thus decreasing E_b, while the salt ions can also adsorb on the surface, thus increasing the charge and consequently E_b. Furthermore, in the presence of a high concentration of salt, the large charge on the colloid particles results in the formation of a dipole layer near the surface, and the interaction of these dipole layers upon collision of the particles will complicate any modeling of the interactions. To avoid all of these potential problems, we use an alternate method to induce the aggregation. We add a small concentration of a neutral organic molecule, pyridine, which is preferentially adsorbed on the surface of the colloid, displacing the citrate ions and thereby reducing the surface charge and E_b. This technique is both highly reproducible and simple to control. In addition, we can monitor the surface adsorbates directly using surface–enhanced Raman scattering to measure both the amount of pyridine on the

surface and the rate at which it is adsorbed.[24]

Using this technique to induce the aggregation, we obtain the same classical behavior[2] expected for aggregation of colloids with an electrolyte, as shown in Fig. 2.2. Here we have plotted the inverse of the initial aggregation rate, as a function of the pyridine concentration, on a logarithmic graph. The initial aggregation rate is determined from the time taken for the color of the colloid to change from wine–red to blue after addition of the pyridine. At pyridine concentrations above 10^{-3} M, the aggregation rate becomes independent of the amount of pyridine, indicating that the energy barrier has been reduced to much less than k_BT, and the aggregation is diffusion limited. At this point, the stability factor is by definition equal to 1, and the change in W is also plotted on the right of the graph. At lower concentrations, the initial aggregation rate is decreased, reflecting the increased W, and indicating that E_b remains on the order of, or larger than, k_BT. In all cases, SERS measurements show that the pyridine is adsorbed onto the surface of the gold colloids on a time scale much shorter than the aggregation time.

In our studies of the aggregation process, our emphasis is on the two limiting regimes of aggregation shown in Fig. 2.2. We study the very fast aggregation by making the solution 10^{-2} M in pyridine, in which case $E_b \sim 0$ and the aggregation is purely diffusion limited. We name this regime as diffusion–limited colloid aggregation (DLCA). We also study very slow aggregation by making the solution $\sim 10^{-5}$ M in pyridine. In this case E_b is considerably greater than k_BT, and the rate limiting step in the aggregation is the time taken for two particles to actually stick to one another, and we label this regime the reaction–limited colloid aggregation (RLCA). Both regimes are also alternately called cluster–cluster aggregation due to their nature of the aggregation.

In addition to colloidal gold, we also study the behavior of two other colloids which are very different from colloidal gold: colloidal silica and polystyrene latex.

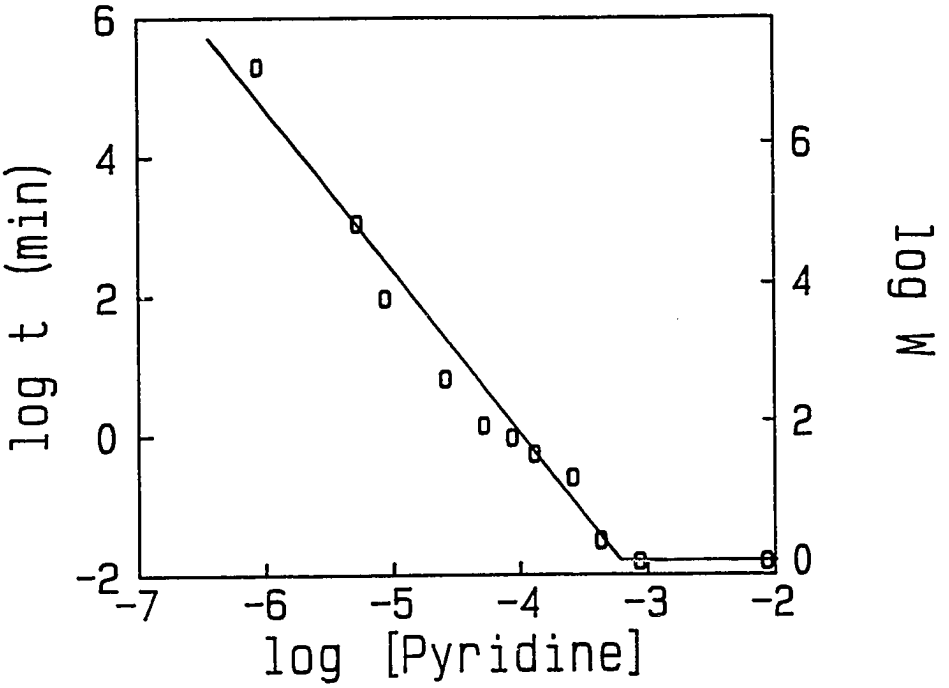

Fig. 2.2 Aggregation time (left) and stability factor (right) of colloidal gold as a function of the pyridine concentration in molarity, on a logarithmic (base 10) scale.

Colloidal silica is available from DuPont under the commercial name of Ludox. We use two types of Ludox in our experiments: TM and SM. TM has colloidal silica particles of average radius a=11 nm. SM has smaller particles with a=3.5 nm. Both are initially stabilized by SiO^- groups on the surface of the particles. The concentration is diluted to $\phi_0=10^{-3}$ to 10^{-6} for the experiments. During the dilution, the Ph of the solution is reduced from >10 to ~7. However, high concentration of OH^- ions is needed to catalyze the formation of particle–particle bonding during the aggregation. Thus the Ph is increased to $\geq$11 by addition of NaOH. Aggregation can be initiated by addition of NaCl, which decreases the Debye–Hückel screening length, reducing the repulsive barrier between the particles. For DLCA, we use Ludox–TM, and the final salt concentration is 1.7 M. For RLCA, Ludox–SM is used, and the final salt concentration is less than 0.6 M. The interparticle bonds of the aggregates are believed to be siloxane bonds.

The polystyrene latex was commercially available from Dow Diagnostics. The polystyrene has a=19 nm and is diluted to $\phi_0=0.8 \times 10^{-6}$. The polystyrene is stabilized by charged carboxylic acid groups on their surface. For DLCA, aggregation is initiated by adding HCl to a concentration of 1.2 M which both neutralizes the surface charges and decreases the Debye–Hückel screening length. For RLCA, the aggregation is initiated by adding NaCl to a concentration of about 0.2 M. The interparticle bond of the aggregates are due to Van der Waals interactions.

The two limiting regimes are achieved with cares by carefully monitoring the aggregation process. For RLCA, we ensure that the aggregation rate is very slow. This invariably results in an exponential growth rate of the aggregates, and leads to a fractal dimension measured by static light scattering, of ~2.1. Nevertheless, RLCA is relatively easy to produce, as it only requires that E_b/k_BT is not too large,

while its value can still vary. A reaction–limited process can last from a few hours to several days. We have tried to adjust our experimental conditions so that the aggregates grow up to $\sim$ 10 μm in about 8 to 10 hours, during which time we make the measurements continuously.

To achieve a diffusion–limited aggregation kinetics requires the barrier height between the colloidal particles to be $E_b \approx 0$. This is a more strict condition. If the barrier height is larger than zero, because of remaining surface charges, or sizable screening length κ^{-1}, the aggregation kinetics will exhibit RLCA behavior initially, and then cross–over to DLCA. This can result in a fractal dimension larger than 1.9. Therefore, precautions are taken in preparing for the aggregation of each colloid. Distilled, deionized and filtered water is used in every step for diluting the solutions to avoid possible surface contamination. Only the water is filtered, not the colloids, since going through the filter may induce some pre–aggregation and possibly change the particle surface chemistry and concentration. For colloidal gold, aged water seems to cause difficulties in the complete displacement of the surface ions, resulting in aggregation kinetics that are not in the DLCA regime but are rather in the crossover regime, even though the aggregation rate is quite fast. For colloidal silica, it is crucial to have enough OH^- ions in the solution to catalyze an irreversible, permanent bond when the particles stick.

2.4 EXPERIMENTAL TECHNIQUES

Transmission Electron Micrography (TEM) We use TEM to visually analyze the structure and the cluster mass distribution of colloidal gold aggregates. Carbon–coated copper grids are prepared by placing them in an oxygen discharge just before being used. This makes the grids hydrophilic and readily wet by the aqueous colloid solution. A few $\mu\ell$ of sample solution of the aggregating colloid is placed on a grid and allowed to dry. The surface of the water is nearly parallel to

that of the grid as the fluid evaporates. Thus we believe that the relatively strong surface tension will pull the gold cluster straight down to the grid, causing only a small distortion of the true geometric projection. By using only ~3 $\mu\ell$ of the solution, we ensure that the clusters are widely separated on the grid so that no further aggregation occurs during the preparation. Each grid contains many clusters of varying sizes and represent a snapshot of the aggregating colloid. The TEM pictures taken from these grids are very clear with high contrast. The magnification of TEM can vary from X6K to X600K as needed. An example of these TEM pictures is shown in Fig. 2.3.

Light Scattering Light scattering techniques are used to probe many key features of the aggregation process of the colloids and to compare their behavior. The experimental setup is shown schematically in Fig. 2.4. It consists of an index matching fluid bath in the center of a goniometer, a laser, and the detector optics on the rotating arm of the goniometer. A cylindrical glass sample cell of about 5 mm in diameter is placed in the center of the bath. To minimize the flare caused by the reflection of the laser beam, an absorber is placed in the bath near the beam exit window. The scattered light from the sample is collected by the main detector optics (MDO) on the rotating arm, which can move from θ=0^{o} to θ=150^{o}. A schematic draw of the detector optics is shown in Fig. 2.5. It has two collimating lenses, three slits, and an interference filter wheel, all inside a cylindrical housing, which is connected to a photomultiplier tube (PMT). Slit s_1 is used to control the detected sample volume, and s_2 and s_3 are used to control $\Delta\theta$, the angular range that is seen by the detector at any angle θ. The output of PMT, after an amplifier and a discriminator, is sent to a correlator, which computes the temporal autocorrelation function of the received signals. The whole setup is controlled by a MC–5500 computer, via IEEE cables. A comprehensive program is constructed to control the experiments, including data taking, changing experimental parameters

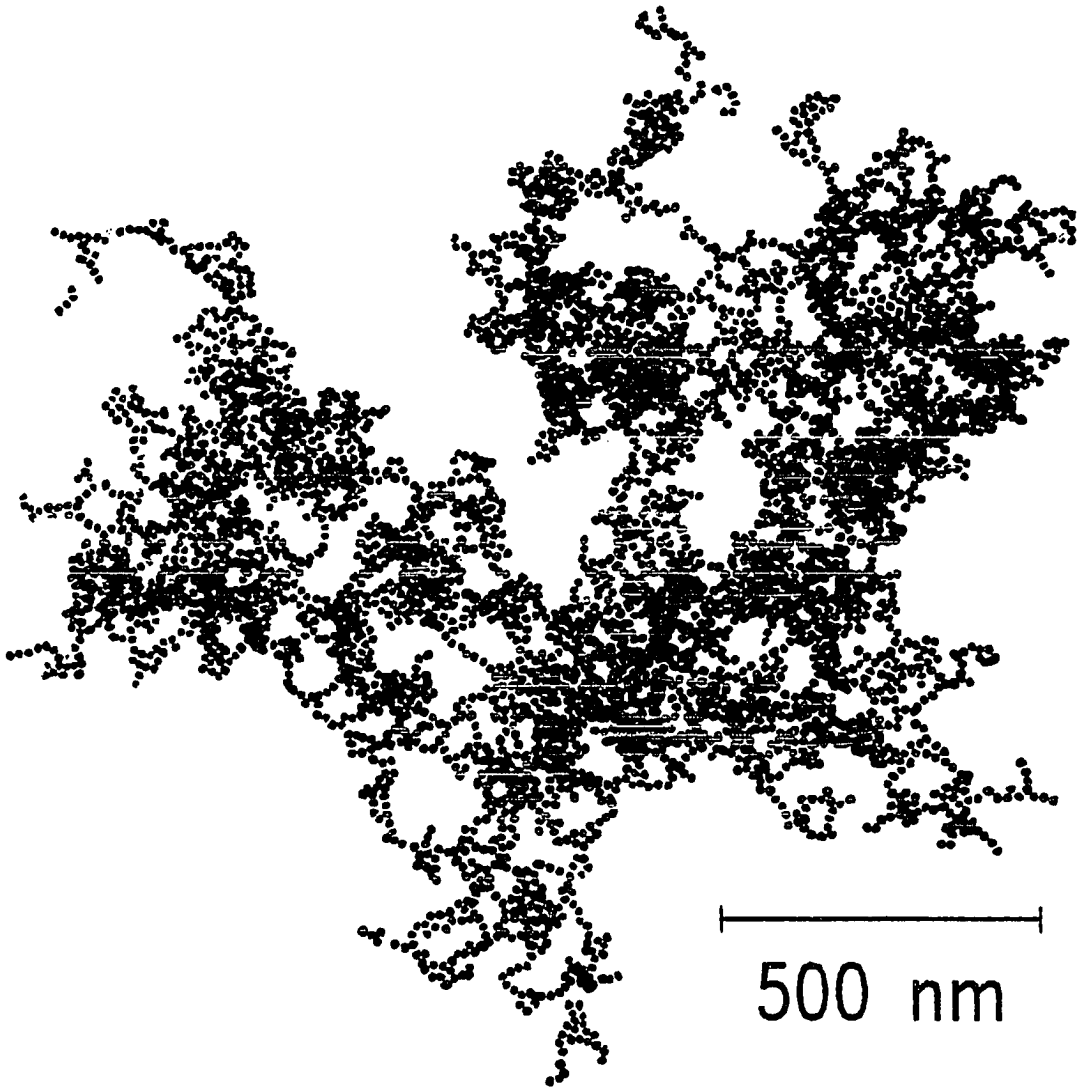

Fig. 2.3 TEM picture of a typical fractal gold colloid aggregate. This cluster is called "4739" in honor of the number of gold particles it contains.

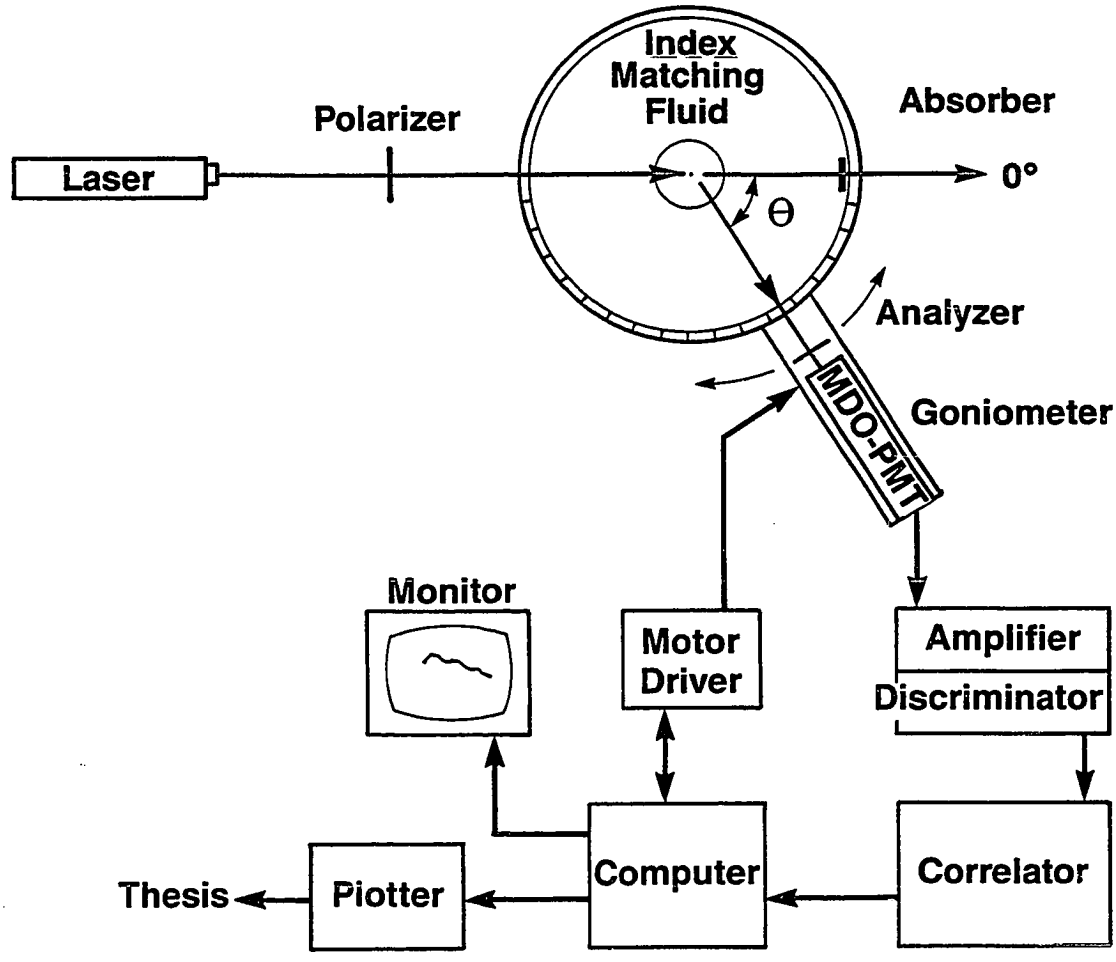

Fig. 2.4 A schematic draw of the setup for light scattering experiments. On the rotating arm is the main detector optics and the photomultiplier tube (MDO–PMT).

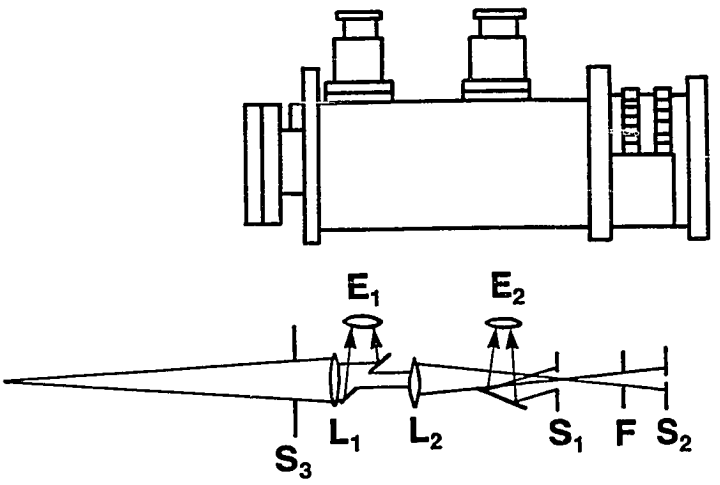

Fig. 2.5 A schematic draw of the main detector optics (MDO). L_1 and L_2 are the collimating lenses; E_1 and E_2 are eyepieces for making alignment; F is an interference (wavelength) filter; slit S_1 is used to control the sample volume detected; and, slits S_2 and S_3 are used to fine adjust θ and $\Delta\theta$.

(sample time, prescale, angle, etc.), analyzing data, and plotting results.

We use static light scattering to measure the total intensity scattered from colloidal aggregates as a function of the scattering wavevector

$$q = |\mathbf{k}-\mathbf{k}'| = \frac{4\pi n}{\lambda}\sin\frac{\theta}{2} \tag{2.3}$$

where $\mathbf{k}$ and $\mathbf{k}'$ are the wavevectors of the incident and scattered waves, λ is their wavelength, n is the index of refraction of water, and θ is the scattering angle.

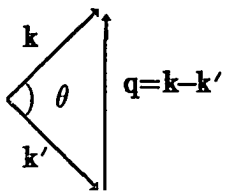

Fig. 2.6 A schematic representation of the wavevectors in the scattering plane.

Because of the overlap between the volume imaged by the collection optics with the incident laser beam, the scattering volume is proportional to $(\sin\theta)^{-1}$.[33] After this correction, the static scattering intensity $I(q(\theta))$ from Rayleigh scatterers (isotropic scatterers) should be independent of θ. We check this periodically to ensure there is no angular dependence in the measured $I(q)$ due to goniometer misalignment. We use toluene as the Rayleigh scatterers. An acceptable $I(q)$ measurement from toluene is shown in Fig. 2.7. It has random fluctuation of less than ±3%, but has no obvious trend except at $\sim 10^{\circ}$, where in practice, a small amount of flare cannot be avoided due to the finite size of the laser beam and of the sample cell. For fractal objects, the scattering at small q is usually very strong (typically more than 100 times larger than that from toluene), so that we can still make measurements at $\theta \approx 10^{\circ}$.

Dynamic light scattering is also used in our experiments. We use homodyne scattering, which measures the temporal autocorrelation function of the scattering intensity,

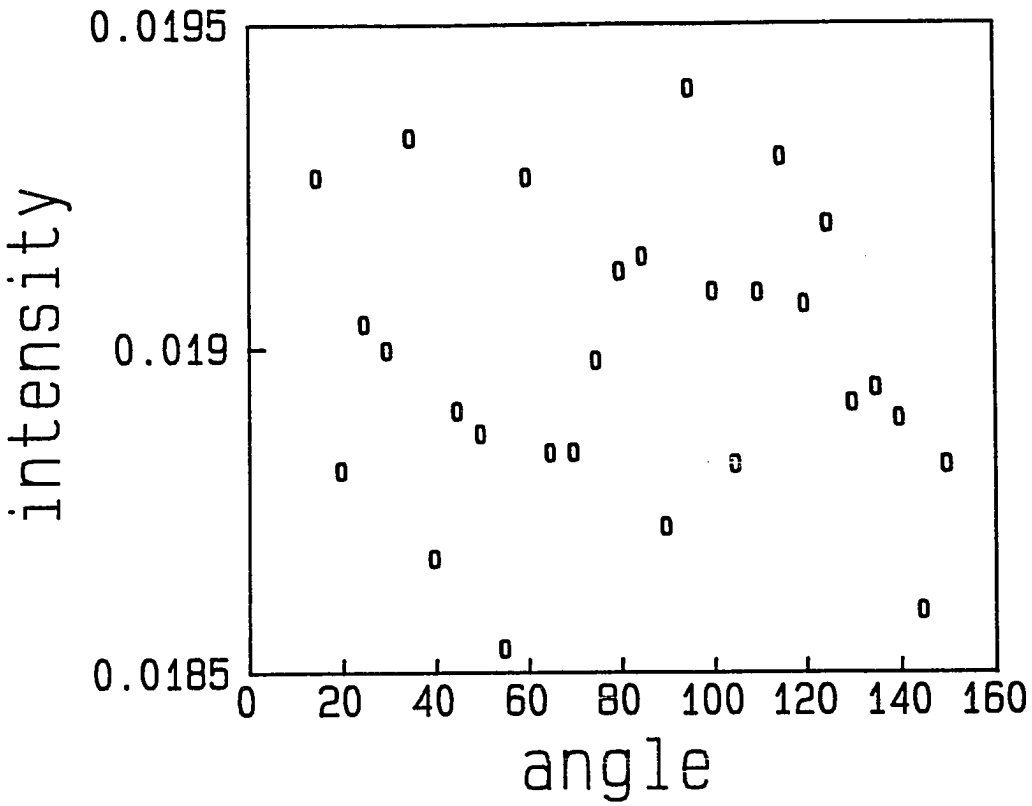

Fig. 2.7 The static scattering intensity from toluene (Rayleigh scatterers) when the goniometer is well aligned. It exhibits random fluctuations of ±3%. The intensity is in arbitrary units.

$$G_2(t) = < I(t') \; I(t'+t) > \tag{2.4}$$

where t is the delay time and the brackets represent an average over time t'.

With our experimental setup, we can measure both static and dynamic scattering concurrently as function of the scattering angle θ, and hence the scattering wavevector, q. We use an Argon ion laser with a wavelength λ=488 nm as the incident source. For the colloidal gold samples, which absorb the incident light, the incident intensity is maintained at less than 1 mw before entering the sample cell to avoid heating effects. A 256–channel correlator and a rotating arm goniometer carrying the detecting optics are used to measure the scattered intensity, $I(q)$, and the intensity autocorrelation function, $G_2(t)$. At each angle, the sample time of the correlator (the time interval of each channel) is adjusted so that the magnitude of the measured autocorrlation function decays by about one decade over the 256 channels. The baseline, B, of the autocorrelation function is determined both from the measured average intensity and from the correlator baseline channels which is delayed an additional 1028 sample times. While the two methods usually agree to within 0.5%, the average intensity is always used in the analysis.

2.5 FRACTAL STRUCTURE OF COLLOIDAL AGGREGATES

The key to much of our recent progress in understanding kinetic aggregation has been our ability to quantitatively characterize the highly disordered structure of the aggregates in terms of fractals. In this section, we discuss the experimental techniques to determine both the dilation symmetry of the clusters and their fractal dimension. For concreteness, in this section, we consider the structure of aggregates all prepared under identical conditions of diffusion–limited colloid aggregation.

Ideally, the best way to study the structure of the highly disordered colloidal aggregates would be to visualize them in three dimensions. However, the very small size of the gold particles makes it necessary to use TEM to attain sufficient

resolution to measure the structure down to length scales of the order of the individual particles.[26] The colloidal gold are ideally suited for this because the gold presents such a high contrast for the electron beam. The use of TEM has the disadvantage that the image is a two–dimensional projection of the three–dimensional cluster, and the analysis must take this into account. Furthermore, the clusters must be removed from the solution and dried, leading to some distortion of their structure. Nevertheless, TEM imaging remains the most direct and convenient method to actually see and analyze the structure.

A TEM picture of a typical cluster is shown in Fig. 2.3, illustrating the highly disordered structure of the aggregates. The individual gold particles can be clearly resolved, and their high degree of uniformity is apparent. An important feature to note about this picture is that the regions where particles overlap represent only a few percent of the total area of the image. Despite the fact that this is a two–dimensional projection of a three–dimensional object, it is at least partially transparent to light, signifying that $d_f<2$.

The most straightforward form of analyzing the fractal symmetry is based on the definition of a fractal object in terms of the scaling of the mass with its linear dimension, $M \sim R^{d_f}$. Thus, we consider a number of different clusters and measure how their mass scales with their size. The mass is determined by counting the number of gold particles in each cluster. The radius is determined by the geometric mean of the longest distance across the cluster and the length perpendicular to this. We plot the mass in terms of number of particles as a function of the size, scaled to $2a$, for nearly 100 different clusters on a logarithmic graph in Fig. 2.8. The linear behavior that is observed confirms the fractal scaling, and the slope of the line, determined from a least–squares fit, gives the fractal dimension directly, $d_f=1.7\pm0.1$. It is important to emphasize that this analysis measures the cluster–to–cluster scaling of mass as a function of size.

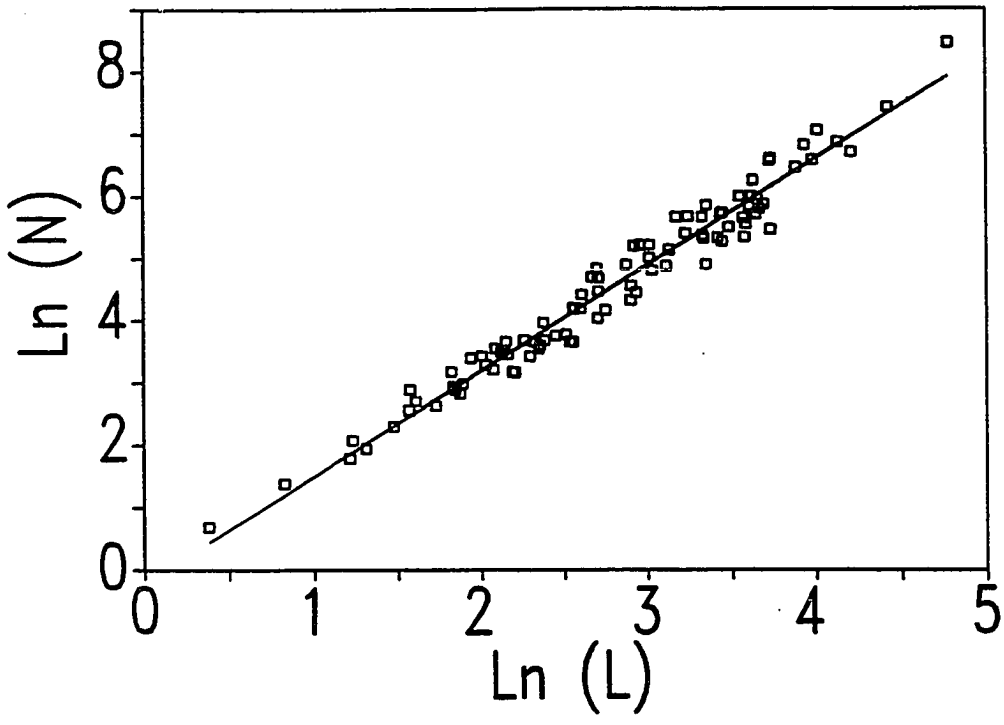

Fig. 2.8 The scaling of the number of gold particles as a function of size, normalized to that of single particle, for many different DLCA clusters. The slope gives d_f=1.70.

We can also investigate the correlations of the particles within a single cluster. This is done by digitizing the coordinates of the centers of each of the gold spheres that comprise a cluster such as the one shown in Fig. 2.3. From these, we compute the two–point correlation function, $g(r)$. There are, however, two important points that must be considered.[27] The first of these is the fact that the picture is really a two–dimension projection of the three–dimensional cluster, and therefore, the computed $g(r)$ is a correlation function of the projected object. For a fractal object, $g(r) \sim r^{-\alpha}$ where the codimension relates the fractal and Euclidean dimensions, $\alpha = d - d_f$. For a geometric projection, one can show[28] that $g(r) \sim r^{-\alpha'}$ where $\alpha' = \alpha - 1$. Thus, the object remains fractal, with the same fractal dimension. Of course this is only reasonable if $d_f < d-1$ so that α' is still a positive quantity. If this were not the case, the projected object would appear solid rather than having the tenuous appearance shown in Fig. 2.3.

A second point that must be considered is that the predicted power law behavior for $g(r)$ applies only to fractal objects of infinite extent. For an object of finite extent, corrections must be applied to the scaling form.[29] These are particularly important for a projected fractal object, where these additional, nonscaling corrections decrease very slowly with size.[26] We must, therefore, account for the finite edge effects when we compute the correlation function. To calculate $g(r)$, an arbitrary gold sphere is taken as the center and the probability of finding a second sphere a distance r away is determined. This is then averaged over the cluster by taking each sphere in the cluster as the center, and averaging all the probabilities. When the particles near the edge of the cluster are used as the center, there is a probability of finding a second particle only in directions toward the middle of the cluster. This edge effect will strongly distort $g(r)$. Thus, we include correlations from each sphere as center only as far as the nearest edge of the cluster. This reduces the statistics somewhat, but provides at least some edge effect

correction to the measured $g(r)$. Quantitatively, the calculated correlation function is

$$g(r) = \frac{1}{M(R-r)} \sum_{r'} <\rho(r')\rho(r'+r)> \qquad (2.6)$$

Here the density is $\rho(r)=1$ at the center of a sphere and is zero elsewhere. In addition, R is the radius of the cluster, while $M(r)$ is the mass of the cluster within a radius r, measured from the center of the cluster. The brackets represent a radial averaging.

The results calculated using Eq. (2.6) for the cluster in Fig. 2.3 are shown on the upper curve of the logarithmic plot in Fig. 2.9. For comparison, the lower curve shows the $g(r)$ that is calculated with no corrections made for the edge effects. Fractal behavior, as exemplified by the linear behavior of $g(r)$, is only seen when the edge corrections are included. The straight line through the data is a least–squares fit to those data in the linear regime. The slope of the line gives the value of α' directly, $\alpha' \sim 0.26$, from which a fractal dimension can be determined, $d_f=1.74\pm0.1$. This value is in excellent agreement with that determined from the cluster–to–cluster variation of the mass with size.

We have analyzed the correlations of several other clusters by measuring $g(r)$ and find that they all give the same value of d_f within our experimental accuracy. In addition, we have used other image analysis techniques to test for the scale invariance of these clusters,[26,27] and find the same value for d_f. Finally, we have tested all of our techniques by generating a random fractal in three dimensions, with a known d_f, on a computer. This was then projected onto a plane, and the same algorithms were used to measure its fractal dimension, and were found to accurately determine d_f. Thus, all the TEM analysis gives consistent results, with $d_f=1.75\pm0.05$, where the error represents our best estimate of the experimental variations based on the measurements of many clusters using several techniques.[26]

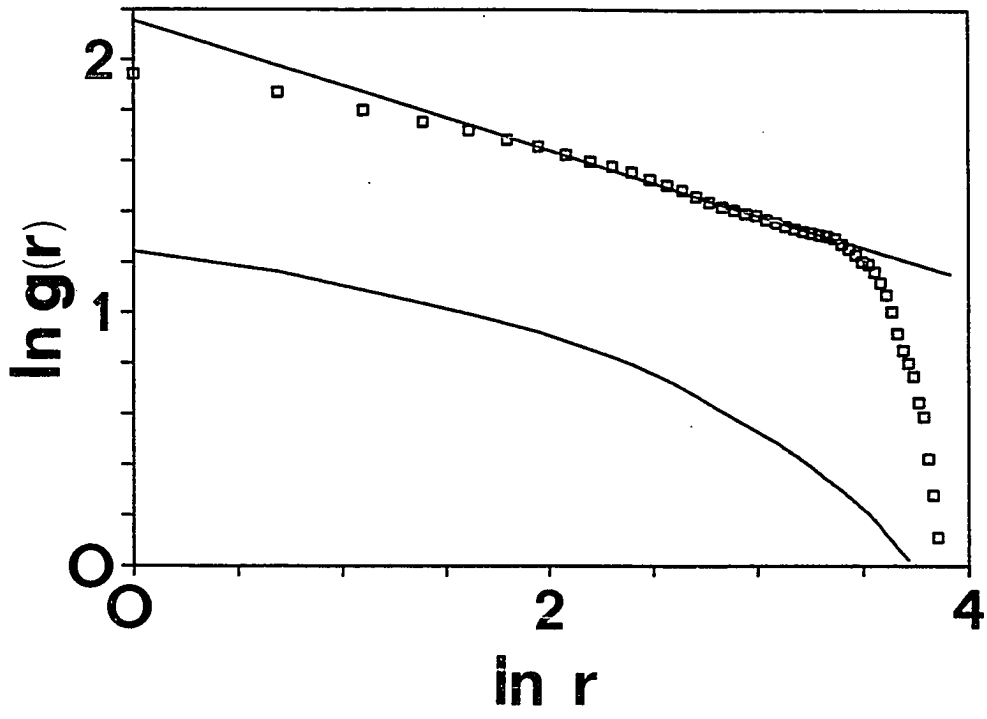

Fig. 2.9 The mass–mass correlation functions for the cluster in Fig. 2.3. The upper curve is corrected for finite cluster edge effects, while the lower curve is not. The slope of the upper curve gives $\alpha'=0.26$, so that $d_f=1.74$.

In addition, we again emphasize that the two techniques of determining d_f, by measuring the variation of the mass of different clusters as a function of their size, and by measuring the internal correlations within a single cluster, are indeed different measures of the fractal scaling of the aggregates. Furthermore, it seems unlikely that any distortion to the shape of the cluster incurred on drying would still result in the same d_f being measured using these two very different techniques, giving us confidence that the d_f obtained by TEM analysis reflects that of the clusters in solution.

While TEM analysis of the clusters provides the only available technique to directly visualize the structure of the aggregates, it has two major drawbacks. First, the clusters must be removed from solution and dried, and secondly, the techniques to measure d_f based on the determination of the mass correlations within a single cluster can only be used if $d_f<2.0$. An alternate probe of the structure that overcomes these problems is the use of scattering techniques.[29-31] These techniques are based on the fact that, in the limit of weak scattering, the intensity, $S(q)$, of the scattered beam is simply a fourier transform of $g(r)$, from real space into momentum space, where q is the scattered wavevector. This relationship is true for all types of scattering, including, for example, light, x–rays, and neutrons. Thus, one has, in principle, a method to make an in situ measurement of the correlation function, and hence the fractal dimension. However, caution must be exercised in interpreting scattering data. The measured $S(q)$ will reflect the Fourier transform of the complete mass–mass correlation function of the aggregates. Thus, it will exhibit not only the scale invariant correlations of the fractal regime, but also the effects of the fact that these fractal correlations extend only over a finite regime. As a consequence, at large q, where short–length scale correlations are probed, $S(q)$ will reflect the scattering from the individual gold spheres themselves, while at low q, where long–length scale correlations are probed, $S(q)$ will reflect the finite extent of

the clusters. In addition, the measured scattering intensity $I(q)$ is an average of $S(q)$ over the cluster distribution, so that the finite size effect must be averaged over the clusters of all sizes in the distribution. Scattering experiments from fractal objects are further complicated by the very nature of these correlations. A detailed description of $S(q)$ and $I(q)$ measured in light scattering experiments is presented in Chapter 4 of this volume.

REFERENCES

[1]E. J. W. Verwey and J. T. G. Overbeek, *Theory of the Stability of Lyophobic Colloids* (Elsevier, Amsterdam, 1948).

[2]H. Reerink and J. T. G. Overbeek, *Discuss. Faraday Soc.* **18**, 74 (1954).

[3]J. T. G. Overbeek, *J. Coll. Interface. Sci.* **58**, 408 (1977).

[4]S. Chandrasekhar, *Rev. Mod. Phys.* **15**, 1 (1943).

[5]T. A. Witten Jr. and L. M. Sander, *Phys. Rev. Lett.* **47**, 1400 (1981).

[6]P. Meakin, *Phys. Rev. Lett.* **51**, 1119 (1983).

[7]M. Kolb, R. Botet and R. Jullien, *Phys. Rev. Lett.* **51**, 1123 (1983).

[8]*Kinetic Aggregation and Gelation*, ed. F. Family and D. P. Landau (Elsevier, Amsterdam, 1984).

[9]R. Jullien, M. Kolb and R. Botet, in *Kinetics of Aggregation and Gelation*, ed. F. Family and D. P. Landau (Elsevier, Amsterdam 1984) p. 101.

[10]M. Kolb, *Phys. Rev. lett.* **53**, 1653 (1984).

[11]P. Meakin, T. Vicsek and F. Family, *Phys. Rev.* **B31**, 564 (1985).

[12]P. Meakin, Z.–Y. Chen and J. M. Deutch, *J. Chem. Phys.* **82**, 3786 (1985).

[13]R. Botet and R. Jullien, *J. Phys. A: Math. Gen.* **17**, 2517 (1984).

[14]P. G. J. Van Dongen and M. H. Ernst, *Phys. Rev. Lett.* **54**, 1396 (1985).

[15]F. Leyvraz, *Phys. Rev.* **A29**, 854 (1984).

[16]S. K. Friedlander and C. S. Wang, *J. Coll. Interface Sci.* **22**, 126 (1966).

[17]M. Faraday, *Phil. Trans. Roy. Soc.* London **A147**, 145 (1857).

[18]G. Mie, *Ann. Physik* **25**, 377 (1908).

[19]M. Von Smoluchowski, *Phys. Z*, **17**, 593 (1916).

[20]F. Kirchner and R. Zsigmondy, *Ann. Physik* **15**, 573 (1904).

[21]J. Turkevich, P. C. Stevenson and J. Hillier, *Trans. Discuss. Faraday Soc.* **11**, 55 (1951).

[22]M. Horisberger, *Gold Bull.* **14**, 90 (1981).

[23]J. A. Creighton, C. G. Blatchford and M. G. Albrecht, *J. Chem. Soc. Faraday Trans. II* **75**, 790 (1979).

[24]D. A. Weitz, M. Y. Lin and C. J. Sandroff, *Surf. Sci.* **158**, 147 (1985).

[25]B. V. Enustun and J. Turkevitch, *J. Am. Chem. Soc.* **85**, 3317 (1963).

[26]D. A. Weitz and M. Oliveria, *Phys. Rev. Lett.* **52**, 1433 (1984).

[27]D. A. Weitz and J. S. Huang, in *Kinetics of Aggregation and Gelation*, ed. F. Family and D. P. Landau (Elsevier, Amsterdam 1984) p. 19.

[28]B. B. Mandelbrot, *The Fractal Geometry of Nature* (Freeman, San Francisco, 1982).

[29]see Chapter 4, this volume.

[30]S. K. Sinha, T. Freltoft and J. Kjems, in *Kinetic Aggregation and Gelation*, ed. F. Family and D. P. Landau (Elsevier, Amsterdam 1984) p. 87.

[31]D. W. Schaefer, J. E. Martin, P. Wiltzius and D. S. Cannell, *Phys. Rev. Lett.* **52**, 2371 (1984).

[32]B. J. Berne and R. Pecora, *Dynamic Light Scattering* (Wiley, New York, 1976).

[33]*Instruction Manual Laser Light Scattering Goniometers* (BIC, Ronkonkoma, New York, 1984).

CHAPTER 3

DYNAMIC SCALING OF CLUSTER MASS DISTRIBUTIONS IN KINETIC COLLOID AGGREGATION

ABSTRACT

The cluster mass distributions produced in the kinetic aggregation of aqueous gold colloids are measured over an extended range of masses for two limiting kinetic regimes, diffusion–limited (DLCA) and reaction–limited aggregation (RLCA). Markedly different distributions are found, with DLCA having a peaked distribution, while RLCA has a power–law distribution. In both cases the distributions are shown to exhibit dynamic scaling, as has recently been predicted. The data are interpreted with the Smoluchowski equations, and are used to determine the form of the appropriate kernel for each regime.

3.1 INTRODUCTION

The study of the kinetic aggregation of small particles to form larger clusters has achieved new prominence[1,2] with the discovery that the structures of colloidal aggregates exhibit dilation symmetry, and thus are well described as fractals.[3,4] In an effort to develop a more fundamental understanding of these kinetic growth processes, attention has now turned to the dynamics, which are intrinsically related to the resultant structures. These dynamics are most clearly embodied in the cluster mass distribution, $N(M)$, and its time dependence. The shape of the cluster mass distribution has a profound effect in determining the dominant reaction events which ultimately strongly influence the structure of the resultant clusters. Furthermore, it now appears that cluster–cluster aggregation can fall into two distinct regimes of behavior, each belonging to a separate universality class.[5-7] Knowledge of the cluster mass distribution is crucial both to distinguish and identify each regime, and to develop any fundamental understanding of the kinetic behavior characterizing that regime. Finally, since many studies of colloid aggregation rely on scattering measurements, a knowledge of $N(M)$ is indispensable for proper interpretation of the results.

A convenient, and widely used description of the cluster mass distribution is through the use of the generalized Smoluchowski equations.[8-11] While these equations themselves can not predict the shape of the aggregates, the effects of the structure, as well as most of the other important physics of the aggregation process, must be included in the kernel or reaction matrix used in their solution. It has recently been demonstrated that the solutions for a broad class of commonly encountered kernels exhibit a dynamic scaling[12,13] and can be classified into three general categories,[11] thus providing an important framework for the description of the aggregation dynamics. However, the key to the successful application of the Smoluchowski equations is the choice of the appropriate kernel, and this has been

severely hampered by the lack of experimental data.

In this chapter, we present measurements of the cluster mass distribution, $N(M)$, and its time dependence, produced by the kinetic aggregation of aqueous gold colloids, and show that the shape of the cluster mass distribution depends critically on the aggregation kinetics. We study two limiting kinetic regimes,[5] diffusion–limited (DLCA) and reaction–limited cluster–cluster aggregation (RLCA), each of which have their own characteristic dynamics, and produce aggregates with different fractal dimensions, d_f. We show here that the cluster mass distributions are also markedly different, with $N(M)$ for DLCA exhibiting a reasonably well defined peak, while for RLCA, it is more nearly described as a power law. Furthermore, we show that the cluster mass distributions exhibit dynamic scaling in both cases, and we suggest the appropriate form of the kernels for a Smoluchowski equation description of the dynamics.

3.2 EXPERIMENT RESULTS

We measure $N(M)$ by analyzing transmission electron microscope (TEM) images of the clusters on TEM grids prepared at several times as the aggregation proceeds.[3] A sampling of the clusters is obtained from several low magnification micrographs of random regions on a grid. The mass, M, of every cluster in the micrograph is determined by counting the number of gold particles in the cluster, i. Sufficient clusters are counted to obtain a representative sampling of $N(M)$ at each time, and the data are compiled in histograms, whose bins are divided evenly on a logarithmic scale, with the results normalized by the bin width. Thus the accuracy with which we must measure the cluster mass is reduced as the mass increases. While this measurement technique provides somewhat limited statistical accuracy, it is both simple and provides results over a very large range of cluster masses.

Typical TEM images showing clusters produced in each regime are shown in

Fig. 3.1. Initially, the colloid is stabilized against aggregation by the large charge on the surface of the particles, and by controllable reducing this charge to varying degrees, aggregation is induced with a wide range of rates. In Fig. 3.1(a), the clusters were produced by DLCA, and the sample was prepared one minute after the aggregation was initiated. Since all the charge has been displaced, the clusters stick to each other immediately upon collision, and the aggregation rate is limited solely by diffusion. The screening of the cluster interior due to the diffusive trajectory leads to the open, tenuous structure evidenced in the figure, with $d_f \approx 1.8$. Furthermore, while there is a broad distribution of cluster masses, no one size predominates. In contrast, Fig. 3.1(b) shows clusters produced by RLCA, and was prepared 2 hours after the aggregation was initiated. The slow rate is a consequence of the remaining surface charge, which provides a Coulombic repulsion between the particles and results in a very low probability of sticking upon collision. Thus the diffusive trajectory no longer affects the cluster structure, but rather they can interpenetrate to a greater extent, leading to the denser structures evidenced by the larger clusters in the figure, and consistent with the higher fractal dimension, $d_f \approx 2.1$. Furthermore, the cluster mass distribution is clearly substantially different, as evidenced by the preponderance of clusters with very small masses.

A histogram analysis of the cluster mass distribution for DLCA is shown in a logarithmic plot in Fig. 3.2 for data collected 3 different times after the initiation of the aggregation. Each data set is normalized to the total number of single gold particles actually counted, $N_0 = \Sigma MN(M)$. As time increases, the number of clusters of a given mass decreases, while the mass of the largest clusters increases. The sample error bars shown reflect the statistical errors due to the number of clusters counted, normalized by the bin width. At the later times, most of the bins at low mass contain, at most, only one cluster. Empty bins are shown by the points below the axis break, while bins containing a single cluster have the very large error bars.

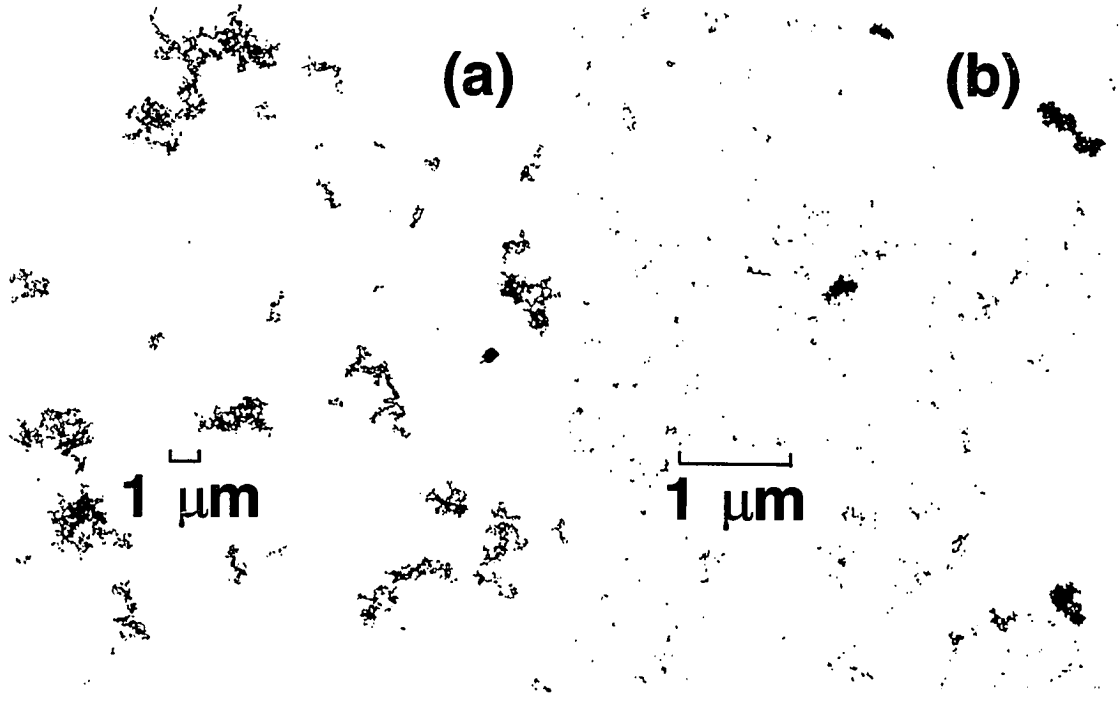

Fig. 3.1 Typical TEM images of clusters formed by (a) diffusion–limited and (b) reaction–limited cluster–cluster aggregation. The aggregate's fractal dimensions and the cluster mass distributions are clearly different for the two regimes.

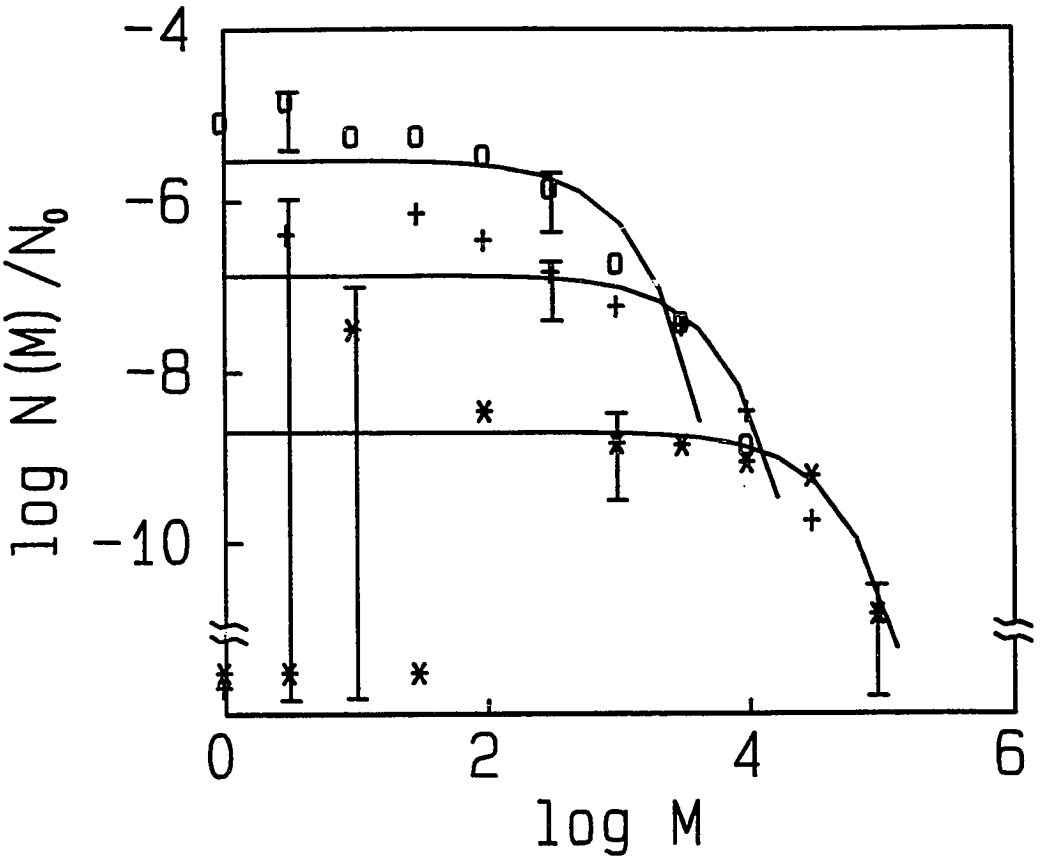

Fig. 3.2 Histogram analysis of the cluster mass distributions for DLCA for samples prepared 1 minute (squares), 10 minutes (pluses) and 30 minutes (stars) after the aggregation was initiated. The points below the break of the y axis represent empty histogram bins in the logarithmic plot, while the very large error bars reflect bins containing only one cluster. Over 100 clusters, comprising about 10^5 gold balls are included in each of the first two data sets, while 25 clusters, comprising about 5×10^5 gold balls, are included in the last.

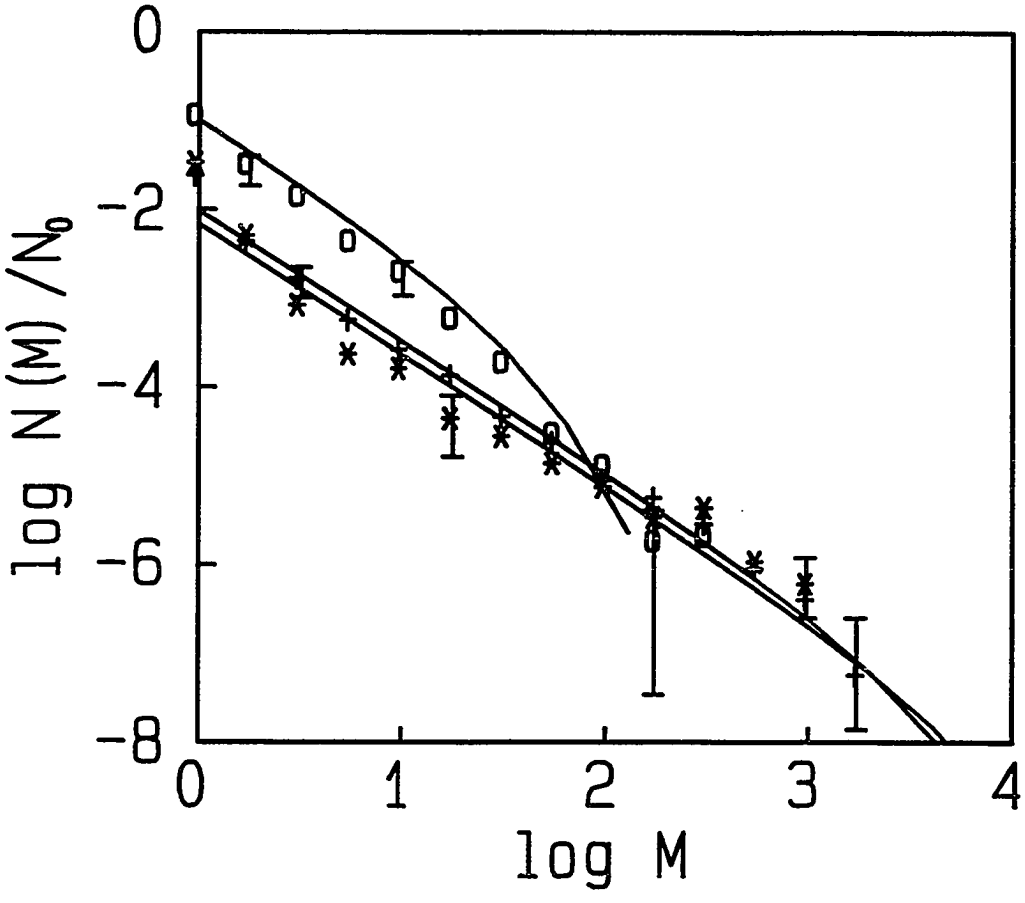

Fig. 3.3 Histogram analysis of the cluster mass distributions for RLCA for samples prepared 2 hours (squares), 6 hours (pluses) and 8 hours (stars) after the aggregation was initiated. About 500 clusters are included in each data set.

The histograms of the cluster mass distributions for reaction–limited aggregation are shown in a logarithmic plot in Fig. 3.3, again for 3 different times after the aggregation is initiated. Each data set is again normalized by N_0. The data can be approximately characterized as a power law, $N(M) \sim M^{-\tau}$, up to some cutoff mass, which increases with time, and with $\tau = 1.5 + 0.1$.

3.3 DISCUSSIONS

We use the Smoluchowski equations[8] to describe the time (t_a) evolution of the cluster mass distribution,

$$\frac{dN_i}{dt_a} = \frac{1}{2}\sum_{j=1}^{i-j} K_{j,i-j}\, N_j N_{i-j} - \sum_{j=1}^{\infty} K_{ij}\, N_i N_j, \tag{3.1}$$

Here $N_i = N(M=i)$ is the number of clusters of mass i while the kernel of the equations, K_{ij}, reflects the rate of aggregation of a cluster of mass i with one of mass j. The first term on the right–hand side is simply the rate of formation of clusters of mass i due to the aggregation of two smaller clusters of the appropriate mass, while the second term is the rate of loss of clusters of mass i due to their aggregation to form yet larger clusters.

In discussing solutions to the Smoluchowski equations, we define the nth moment of the distribution,

$$M_n = S_n / S_{n-1}, \tag{3.2}$$

where

$$S_n = \Sigma\, M^n N(M), \tag{3.3}$$

and $S_1 = N_0$. If the solution exhibits dynamic scaling, it can be expressed as[11]

$$N(M, t_a) = M_n^{-2} \psi(M / M_n) \tag{3.4}$$

where $\psi(x)$ is the scaling function whose form is time independent. Here M_n is any moment of the distribution which reflects the time dependence, which in turn can be characterized by a dynamic exponent,[12,13] z, where $M_n \sim t^z$. Physically, a scaling solution implies that the distribution function attains a form whose shape is independent of time, while all the time dependence is reflected in the behavior of the moments of the distribution.

Many types of aggregation can be described with a class of homogeneous kernels which are characterized by $K_{ij} \sim i^{\mu} j^{\nu}$, for $j >> i$ and $K_{ai,aj} = a^{\lambda} K_{ij}$, so that $\lambda = \mu + \nu$. The solutions can be divided into several classes,[11] depending on the values of the exponents λ and μ, and each exhibiting dynamic scaling, with a characteristic behavior both for the shape of the cluster mass distribution and its time evolution. Thus we can use our measured $N(M)$ to attempt to identify the class of the solution and hence the form of the kernel.

We first consider the appropriate kernel for diffusion–limited aggregation, which has traditionally been taken as[8,14]

$$K_{ij} = 4\pi\sigma_{ij} (D_i + D_j) \tag{3.5}$$

where D_i is the diffusion constant of a cluster of mass i and σ_{ij} is the effective collision radius for clusters of mass i and j. As a consequence of the screening,[2] we take $\sigma_{ij} = R_i + R_j$, where R_i is the radius of a cluster of mass i. Furthermore, scaling arguments,[15] as well as numerical solutions of the hydrodynamic equations,[16] suggest that $D_i \sim R_i^{-1}$. Thus,

$$K_{ij} \sim 2 + (i/j)^{1/d_f} + (j/i)^{1/d_f}. \tag{3.6}$$

We note that this is a special form of the class of kernels we are considering, with

$\lambda=0$ and $\nu=-\mu=1/d_f$ (class III).[11] An analytic solution to the Smoluchowski equations does not exist for this kernel. However, except far off the diagonal, when $i<<j$, this kernel is well represented by a constant, for which an analytic solution does exist,[17]

$$N_i = \frac{N_0}{M_1^2}\left(1-\frac{1}{M_1}\right)^{i-1} \tag{3.7}$$

The solid lines in Fig. 3.2 represent the calculated distribution functions using the values obtained for N_0 and M_1 directly from the TEM analysis. The agreement with the data is satisfactory, except at small mass and long time.

To look for dynamic scaling, we have normalized each data set by M_1^2/N_0 and have plotted them as a function of M/M_1 in Fig. 3.4. Dynamic scaling is indeed observed, as all the data lie on a single curve, which in fact represents the shape of the scaling function $\psi(x)$. If the empty histogram bins had been included in the inset, $\psi(x)$ would tend toward zero at small x. The time dependence of M_1 is best described as a linear function of time, in accord with quasi–elastic light scattering measurements[18] which suggest that $z\approx 1$, as predicted by the constant kernel solution.[17]

The poor agreement between the analytic solutions and our data at low mass and long times most likely reflects the effects of the very large reaction rate far off the diagonal, where the approximation of a constant for the kernel fails badly. Physically, this large reaction rate is due to the small clusters with very large diffusion constants reacting with the large clusters with their large capture radii. This large off diagonal term can be expected to lead to a faster depletion of the concentration of the small clusters. In fact, consistent with our observations, a decrease in the number of particles at low mass and long times has been predicted

for aerosols,[19] as well as by a scaling analysis of the Smoluchowski equations.[11,13]

We now turn our attention to the data for RLCA. The observation of a power–law cluster mass distribution, with $\tau \approx 1.5$, immediately rules out a gelling kernel, with $\lambda > 1$, since this invariably results in a power law distribution with $\tau \geq 2$. Furthermore, it excludes kernels with $\mu < 0$ (class III), since these result in a peaked cluster mass distribution. Kernels with $\mu > 0$ (class I) can produce power law solutions, and require $\lambda = 0.5$ to give $\tau = 1.5$ at the early stages of aggregation. Similarly, kernels with $\mu = 0$ (class II) can also produce power–law solutions with $\tau = 1.5$, but are, in general, more difficult to characterize. However, Ball et al[20] has proposed a geometric scaling model which suggests that the appropriate kernel has $\mu = 0$ and $\lambda = 1$, which not only results in a power law solution with $\tau = 1.5$, but also predicts that the characteristic cluster size grows exponentially in time, in accord with quasi–elastic light scattering measurements for RLCA.[5] For monodisperse initial conditions, an analytic solution exists for the sum kernel, $K_{ij} \sim i+j$, which has similar scaling. In fact, this kernel was found to describe the cluster mass distributions measured, for $i \lesssim 40$, for antigen–antibody induced RLCA of polystyrene colloids.[21] The solid lines in Fig. 3.3 are a fit to the sum kernel solutions,

$$N_i = \frac{N_0 e^{-i\,b} (ib)^{i-1}}{M_1 i!}, \tag{3.8}$$

where $b = 1 - 1/M_1$, and demonstrate good agreement with our data.

To investigate dynamic scaling for the RLCA data, we must use M_2 or a higher moment to reflect the time dependence of the distribution. We obtain M_2 by integrating the sum kernel prediction using the fitted values of M_1 for each data set. We have plotted the 3 data sets, each normalized by M_2/N_0, as a function of M/M_2 in Fig. 3.5. The data all lie on a single curve, illustrating the dynamic scaling, and the shape of the curve represents $\psi(x)$. The time dependence of M_2 is exponential,

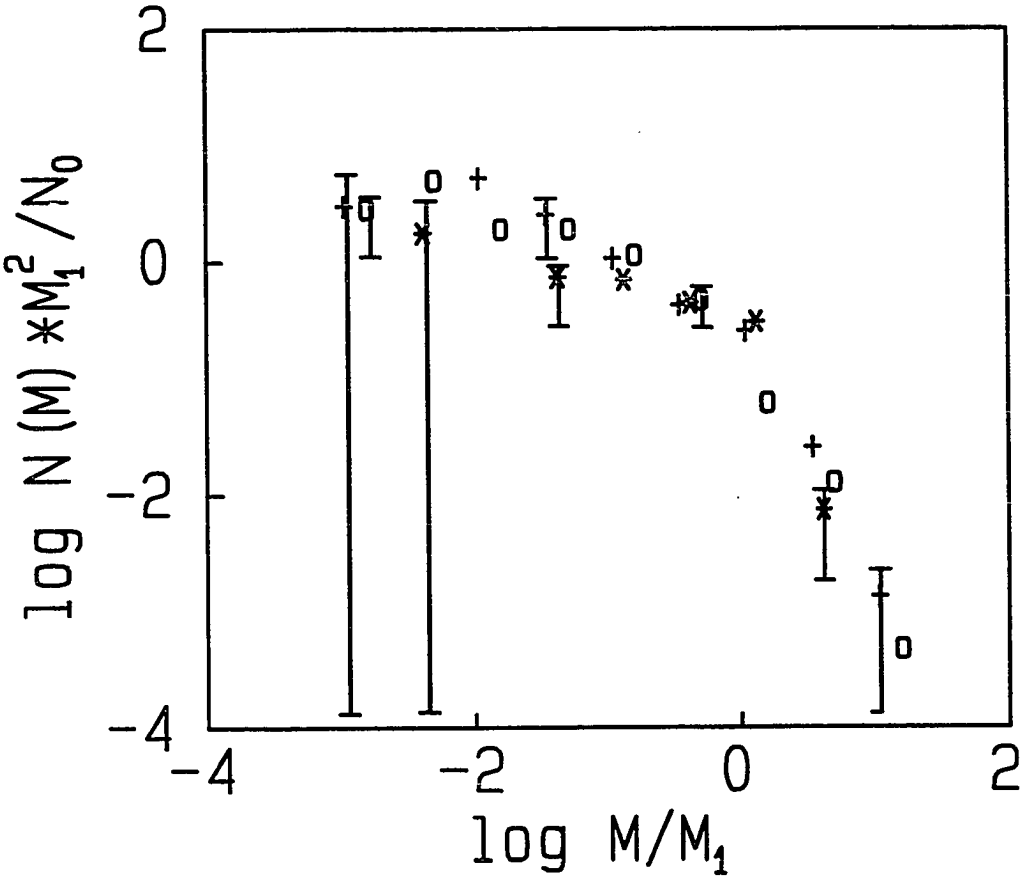

Fig. 3.4 Dynamic scaling of the cluster mass distribution of DLCA aggregates. They are normalized by the first moment of the distribution, M_1.

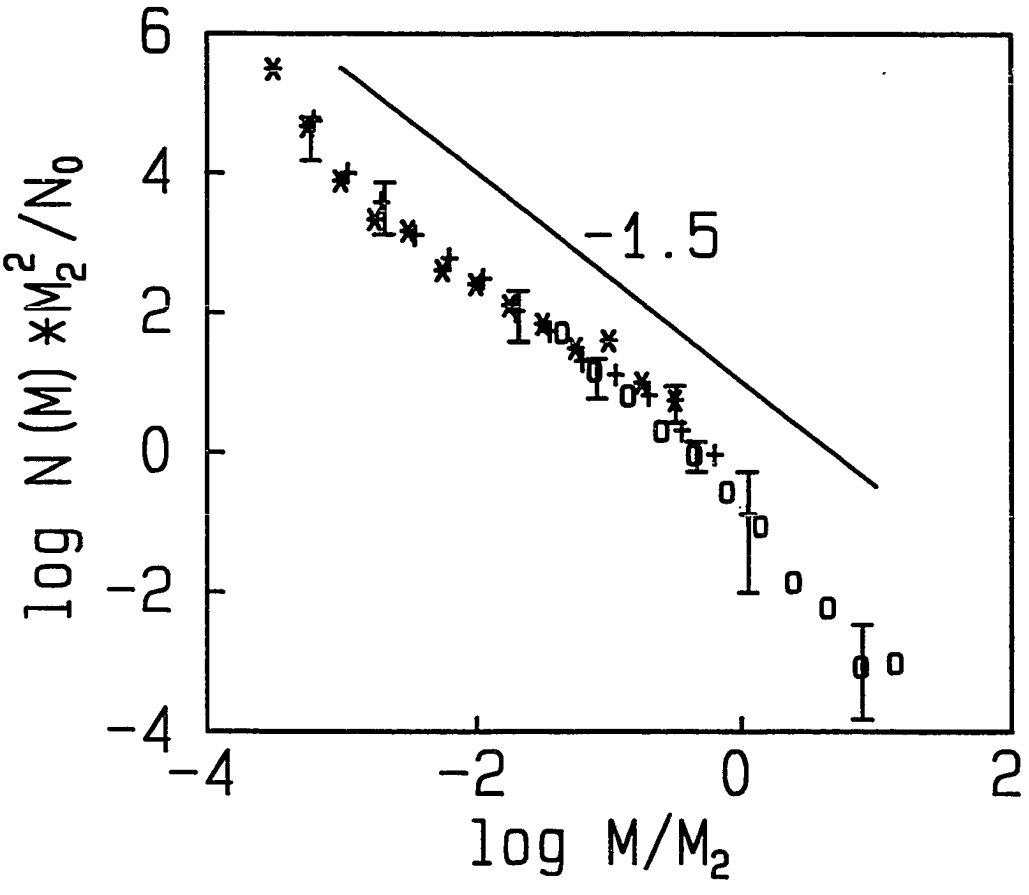

Fig. 3.5 Dynamic scaling of the cluster mass distribution of RLCA aggregates. The data are normalized by the second moment of the distribution, M_2. The solid line represents a slope of −1.5.

in accord with quasi–elastic light scattering measurements.[5] Thus, here z is not well determined here.

While the sum kernel solutions describe our data rather well at early times, the agreement is not as good for the data sets measured at long times. In fact, here our data might be described by two exponents, a larger one at small mass, and a smaller one at large mass. In deed, such behavior is predicted[11] by the scaling analysis of the Smoluchowski equations for class I kernels that are on the boarder of class II, having μ slightly greater than zero. Here, $N(M,t_a)$ is predicted to behave as for $\mu=0$ for an extended period of time, before reaching the steady–state solution, which has two distinct power–law regimes, with $\tau=1+\lambda$ at low mass and $\tau=\lambda$ at higher mass, until it is cut off exponentially. Furthermore, the dynamic exponent predicted is $z=1/(1-\lambda)$, which is very large for $\lambda\lesssim 1$, and, in practice, may not be distinguishable from the exponential growth measured. Thus, we conclude that the kernel which describes RLCA is consistent with $\mu\gtrsim 0$ and $\lambda\lesssim 1$, and thus may be either a class II kernel or a class I kernel that is very nearly class II.

In conclusion, we emphasize that all of these results were obtained with exactly the same colloid system. We merely changed the rate of aggregation by adjusting the surface charge on the particles. Nonetheless, we obtain two markedly different distribution functions, depending on the kinetics.

REFERENCES

[1]*Kinetics* of *Aggregation and Gelation*, ed. F. Family and D. P. Landau (Elsevier, Amsterdam, 1984).

[2]T. A. Witten Jr. and L. M. Sander, *Phys. Rev. Lett.* **47**, 1400 (1981).

[3]D. A. Weitz and M. Oliveria, *Phys. Rev. Lett.* **52**, 1433 (1984).

[4]D. W. Schaefer, J. E. Martin, P. Wiltzius and D. S. Cannell, *Phys. Rev. Lett.* **52**, 2371 (1984).

[5]D. A. Weitz, J. S. Huang, M. Y. Lin and J. Sung, *Phys. Rev. Lett.* **54**, 1416 (1985).

[6]P. Meakin, *Phys. Rev. Lett.* **51**, 1119 (1983); M. Kolb, R. Botet and R. Jullien, *Phys. Rev. Lett.* **51**, 1123 (1983).

[7]R. Jullien, M. Kolb and R. Botet, *J. Phys. Lett.* (Paris) **45**, L211 (1984).

[8]M. von Smoluchowski, *Phys. Z.* **17**, 593 (1916).

[9]M. Kolb, *Phys. Rev. Lett.* **53**, 1653 (1984).

[10]R. Botet and R. Jullien, *J. Phys.* **A17**, 2517 (1984).

[11]P. G. J. van Dongen and M. H. Ernst, *Phys,. Rev. Lett.* **54**, 1396 (1985).

[12]T. Vicsek and F. Family, *Phys. Rev. Lett.* **52**, 1669 (1984).

[13]P. Meakin, T. Vicsek and F. Family, *Phys. Rev.* **B31**, 564 (1985).

[14]S. Chandrasekhar, *Rev. Mod. Phys.* **15**, 1 (1943).

[15]P. G. deGennes, *Scaling Concepts in Polymer Physics* (Cornell Univ. Press, Ithaca NY, 1979).

[16]P. Meakin, Z–Y. Chen and J. M. Deutch, *J. Chem. Phys.* **82**, 3786 (1985).

[17]R. J. Cohen and G. B. Benedek, *J. Phys. Chem.* **86**, 3696 (1982).

[18]D. A. Weitz, J. S. Huang, M. Y. Lin and J. Sung, *Phys. Rev. Lett.* **53**, 1657

(1984).

[19]S. K. Friedlander and C. S. Wang, *J. Colloid Interface Sci.* **22**, 126 (1966).

[20]R. C. Ball, D. A. Weitz, T. A. Witten and F. Layvraz, *Phys. Rev. Lett.* **58**, 274 (1987).

[21]G. K. von Schulthess, G. B. Benedek and R. W. DeBlois, *Macromolecules* **13**, 939 (1980).

CHAPTER 4

STRUCTURE OF COLLOIDAL AGGREGATES STUDIED BY STATIC LIGHT SCATTERING

ABSTRACT

The structure of fractal colloidal aggregates formed in both the DLCA and RLCA regimes of aggregation is studied by static light scattering experiments. The focus is on the cross–over region of the static structure factor of these clusters, where the effect of finite size of the fractal structure plays an important role. With polydispersity of the cluster mass distribution present, it is found that the shape of the measured scattering intensity is very different from the structure factor of individual clusters. A form for the structure factor obtained from computer–simulated clusters is found to describe the structure factor of the colloidal aggregates very well, for both regimes. Other available models for the cross–over region are also discussed. Finally, using static light scattering, we demonstrate the restructuring of the structure of the colloidal aggregates when they are subjected to shear stress.

4.1 INTRODUCTION

The concept of fractal geometry has proven very successful in the description of the kinetic aggregation of colloidal systems. The highly disordered structure the colloidal aggregates has been shown to be scale invariant, therefore be quantitatively described as a fractal,[1] with the fractal dimension d_f. To date, various methods have been applied to experimentally determine d_f for aggregates formed in a kinetic aggregation process. Static light scattering is one of the most widely used methods.

For a fractal structure, its pair density correlation function $g(r) \propto r^{d_f - d}$, where d is the space dimension. In turn, its Fourier transform, or the static structure factor of the fractal, is $S(q) \propto q^{-d_f}$. The significance of the structure factor is that it is measurable in a scattering experiment. The static scattering intensity from a single cluster $I_M(q)$, is proportional to $S(q)$, where q is the scattering wavevector. The experimentally measured quantity, however, is $I(q)$, which reflects the contribution from all the aggregates in the sample volume. These aggregates are characterized by the cluster mass distribution $N(M)$. Although it is known that $I(q) \propto q^{-d_f}$ can still be observed if q is sufficiently large, there is generally no direct proportionality between $I(q)$ and $S(q)$. Instead, the measured scattering intensity reflects an averaged structure factor with the effect of the cluster mass distribution.

This effect is particularly significant in the crossover region of $I(q)$ where it neither scale as q^{-d_f}, nor is independent of q as it is when the light is scattered isotropically. Because of the effect of $N(M)$, this crossover shape of $I(q)$ can be very different from that of $S(q)$. It depends on both the shape of $S(q)$, and the shape of $N(M)$. An understanding of this crossover region is critical in order to properly interpret the results of both static and dynamic light scattering, and to obtain information of the cluster mass distribution, such as the average cluster mass or the average radius of gyration.

Therefore, a detailed understanding of the structure factor of the colloidal aggregates including the crossover region is crucial. Several studies of the structure factor have been reported in recent years. Freltoft et al reported an X–ray study of silica aggregates and proposed a model for the structure factor.[2] Dietler et al[3] and Wiltzius[4] did experiments with colloidal silica (Ludox) aggregates with and without gelation, and used a modified Fisher–Burford form for the structure factor. Recently Hurd and Flower proposed an overlapping sphere model for the crossover region, and used it to fit the data from fumed silica aggregates.[5] Unfortunately, these studies do not consider the effect of polydispersity. Although the fractal dimension can be obtained from the fitting, the forms used do not represent the structure factor of individual clusters. The effect of the polydispersity in many cases is not negligible, especially in colloidal aggregation. If individual clusters are considered, which are usually not available in real experiments, Mountain and Mulholland recently found that the Fisher–Burford form and the overlapping model do not fit the structure factor calculated from computer–simulated aggregates of cluster–cluster aggregation regime.[6]

In this chapter, we present a study of the structure factor of the colloidal aggregates and the static scattering intensity from them, using measurements from colloidal gold aggregates formed by both diffusion–limited (DLCA) and reaction–limited cluster aggregation (RLCA). We show that the structure factor has a rather narrow crossover, reflecting a sharp cutoff of the structure of the individual clusters. We obtain a form of the structure factor by fitting a polynomial to the structure factor calculated for clusters generated by computer simulations. This form, after being summed over the cluster mass distribution, agrees well with the shape of the experimentally measured scattering intensity. We show that although the forms of the structure factor for DLCA and RLCA are not very different, the scattering intensity at the crossover region is markedly distinct for

each regime, which reflects the different effects of the polydispersity of the two regimes.

The rest of the chapter is organized as follows: we first discuss the origin of the crossover region from a theoretical point of view, and compare the available models; we then describe our experimental results and compare these with the calculations. Finally, we demonstrate the restructuring of the structure of colloidal aggregates when they are subjected to shear.

4.2 THEORY

For an infinite fractal, its self–similarity can be expressed by the pair density correlation function

$$g(r) = < \rho(r'+r)\, \rho(r') > \propto r^{d_f - d} \tag{4.1}$$

where $< >$ represents average over all r', and d_f and d are the fractal dimension and space dimension. This density correlation function expresses the probability of finding another mass a distance r away from any mass in the fractal. The fractal objects of interest here, however, are finite, and the correlation function must go to zero as r goes to infinity. Thus the fractal correlation has to be bounded by some cutoff function when r reaches a certain size, for example, the radius of gyration, R_g. Therefore, the correlation function of a finite fractal can be written as

$$g(r) \propto r^{d_f - d} h(r/R_g). \tag{4.2}$$

The cutoff function $h(v)$ is equal to 1 for $v<<1$, and it must decay faster than a power law for $v>>1$. Thus for length scales $r<<R_g$, the object can be seen as an infinite fractal, characterized by the fractal dimension, d_f; however, for a length scales $r \sim R_g$, the boundary effect, or the form of $h(v)$ will dominate.

Usually, a set of fractal objects produced under the same conditions are self–similar among themselves. Not only is their fractal dimension the same, but they also have the same form of $h(v)$. Therefore, the cutoff function, which is a

function of r/R_g, scales with R_g, the size of the individual fractal objects. An important consequence of these properties is that their mass scales with size as

$$M(R_g) = (R_g/a)^{d_f} \tag{4.3}$$

where a is the radius of mass of unity. Statistically, colloidal aggregates produced by either DLCA or RLCA can be treated as a set of these self–similar fractals. In these cases, we use a as the radius of the constituent particles, while using a mass unit such that their mass $M(a)=m=1$. By this definition, Eq. (4.3) may not exactly be an equality, but the two sides should be proportional by a constant about unity. This is because that below the length scale a the fractal scaling no longer exists. However, since the typical radius of a colloidal particle is usually substantially less than the wavelength of the light, while the aggregates usually grow to sizes considerably larger than the wavelength, static light scattering does not probe this lower boundary a. It does, however, probe the fractal correlation characterized by d_f and the cutoff shape described by $h(v)$.

The static structure factor $S(q)$ probed in a scattering experiment is the Fourier transform of the density correlation function $g(r)$, where q is the momentum transfer or the scattering wavevector. It is related to the scattering intensity of a single cluster (aggregate) by $I_M(q)=BM^2S(q)$ where B depends on the experimental conditions and the scattering cross section of the colloidal particles. For three dimension,

$$S(q) = \frac{1}{M}\int d^3r\, g(r)\, e^{-i\mathbf{q}\cdot\mathbf{r}} \propto (qR_g)^{-d_f} f(qR_g) \tag{4.4}$$

where

$$f(x) = \int_0^\infty dz\, z^{d_f-2}\sin z\, h(z/x) \tag{4.5}$$

It can be shown that $f(x) \sim x^{d_f}$ for $x<<1$ and $f(x)$ = constant for $x>>1$. We can choose the constant in $g(r)$ such that the normalization is $S(0)=1$. We note that a normal definition of the structure factor is such that $S(0)=M$ as it represents I_M/M,

the scattering intensity per particle in a given cluster. However, our definition is more convenient in describing the fractal aggregates as it reflects their scaling behavior. To recognize this, it is instructive to discuss the physical origin of the behavior of $I_M(q)$ at both limits of q and its relation with $S(q)$. If an aggregate is sufficiently small that $qR_g<<1$, the scattered electric field from all the particles will add coherently and the intensity will be proportional to the square of the cluster mass M^2. In this limit, the structure factor is simply equal to 1, and is independent of q. On the other hand, a larger cluster with $qR_g>>1$ can be thought to be comprised of smaller subunits, each of size of q^{-1}. Each subunit will scatter completely coherently with an intensity proportional to the square of its mass, $(qa)^{-2d_f}$. However, the phases of the field scattered from different subunits will not be equal, and the incoherent addition of these random phases will cause the total intensity to be the sum of the intensities scattered from each subunit rather than the sum squared. The number of the subunits is the the ratio of the total mass of the cluster to the mass of a subunit, $M(qa)^{d_f}$. Thus the total scattering intensity from the cluster is $I_M(q) \propto M(qa)^{-d_f} = M^2(qR_g)^{-d_f}$. Therefore, the scattering intensity from a cluster of mass M is the mass square times the structure factor, where the structure factor is a function of qR_g *only*, which can also be seen from Eq. (4.4).

In accord with the argument above, we denote the structure factor as $S(qR_g)$ instead of $S(q)$. This means that going to a smaller q vector is equivalent to enlarging the outer size of the structure R_g. It is a direct consequence of the fractal scaling behavior, where R_g is the only characteristic length scale of the object. It is even more powerful in describing colloidal aggregates, where all clusters have the same form of $h(v)$, so that one structure factor describes all individual clusters of different R_g. Indeed, this scaling is applicable not only to the structure factor, which describes the radially averaged properties of the structure, but to the

anisotropy of the fractal aggregates also.[7,8]

The behavior of $S(qR_g)$ at its limits discussed above can also be derived from Eqs. (4.4) and (4.5) as

$$S(qR_g) \Rightarrow \begin{cases} 1 & qR_g<<1 \quad (4.6a) \\ & \text{for} \\ (qR_g)^{-d_f} & qR_g>>1 \quad (4.6b) \end{cases}$$

This limiting behavior is well known, and is the consequence of the coherence of the scattering fields at small q limit and the fractal scaling of the structure at large q limit. It is also independent of the cutoff function $h(v)$. On the other hand, the shape of the structure factor around qR_g=1 is closely related to $h(v)$, and is not well known experimentally. It is however crucial in order to obtain R_g, the radius of the clusters, and to properly interpret the scattering results of both static and dynamic.

Table 4.1. Several proposed forms for the cutoff function

Models	$h(v)$ $(v=r/R_g)$
(a) Single Exponential	$e^{-\kappa_1 v}$
(b) Overlapping Spheres	$1-\frac{3}{4}\kappa_2 v+\frac{\kappa_2^3}{16}v^3$ $v<2/\kappa_2$ 0 $v>2/\kappa_2$
(c) Gaussian	e^{-v^2}
(d) Stretched Exponential	$e^{-0.2v^{2.5}}$

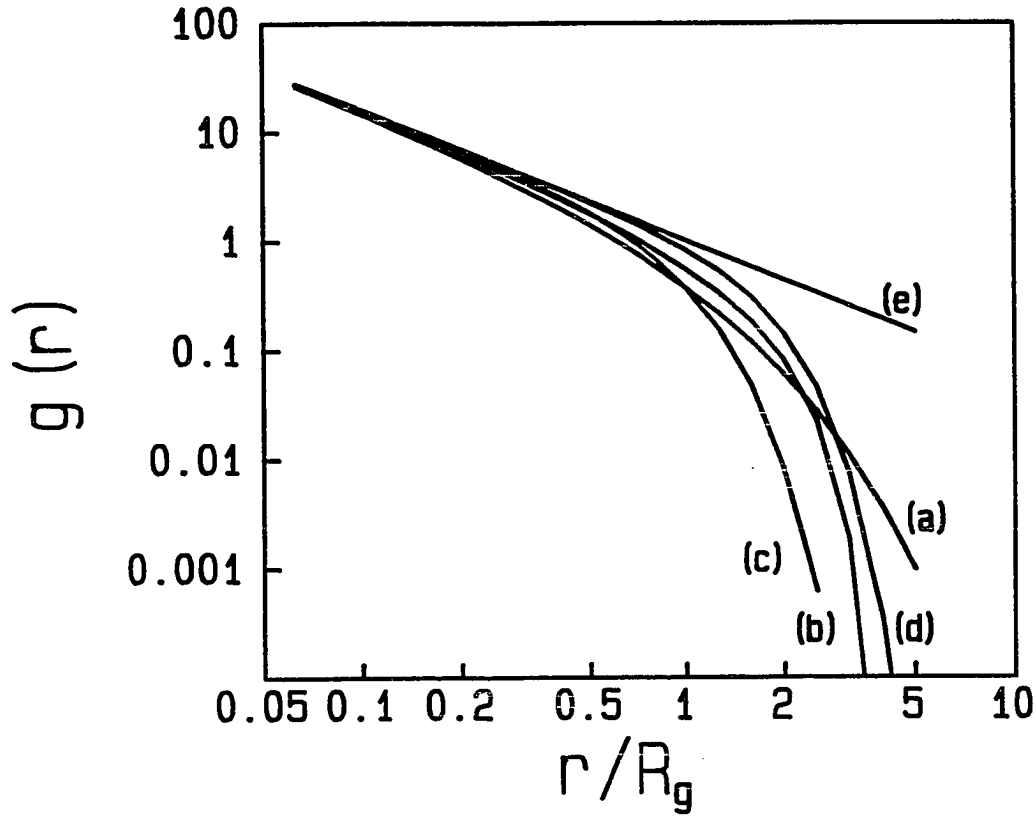

Fig. 4.1 The pair density correlation function $g(r)$ plotted as a function of r/R_g using several different forms for the cutoff function $f(r/R_g)$. (a) Simple exponential, (b) Overlapping sphere model, (c) Gaussian, and (d) stretched exponential. Notice how early the curves deviate from the fractal behavior represented by a straight line (e), which does not have a cutoff function.

Theoretically, a number of models for the cutoff function have been proposed and used to transform $g(r)$ into the structure factor. We list some of these models in Table 4.1. In Fig. 4.1, we plot the shape of $g(r)$ vs. the reduced length $v=r/R_g$ for these models, compared with a straight line representing infinite fractal scaling. Curve (a) uses a single exponential, $h(v)=e^{-\kappa_1 v}$, which yields a structure factor of an analytical form[2]

$$S(qR_g) = C(1+q^2R_g^2/\kappa_1^2)^{(1-d_f)/2}\,\frac{\sin[(d_f-1)\arctan(qR_g/\kappa_1)]}{(d_f-1)qR_g/\kappa_1} \qquad (4.7)$$

where C is a constant close to unity, and $\kappa_1^2=\frac{3}{2}(d_f-1)$ can be determined at the small q limit by Guinier's Law, that $S(qR_g\to 0)\approx 1-\frac{1}{3}q^2R_g^2$. The form of Eq. (4.7) is closely related to the modified Fisher–Burford form[3]

$$S(qR_g) = (1+\frac{2}{3d_f}q^2R_g^2)^{-d_f/2} \qquad (4.8)$$

Both forms are particularly good in describing structures like gels, where the individual clusters interpenetrate each other to form a continuous network. However, the crossover is very slow, as can be seen in Fig. 4.1, and the deviation from the power law behavior is apparent as early as $r/R_g\approx 0.1$. Curve (b) represents a model proposed by Hurd and Flower.[5] They assume that $h(r/R_g)$ can be described by the overlapping volume of two spheres of radius $R_v=R_g/\kappa_2$ separated by a distance r, where

$$\kappa_2^2 = \frac{2d_f(d_f+1)}{(d_f+2)(d_f+5)}$$

can also be determined from Guinier's Law. It again starts deviating from the power law behavior at $r/R_g\approx 0.1$ and makes a smooth crossover until $r/R_g=2/\kappa_2$ where it drops to zero suddenly. Curve (c) uses a Gaussian form for the cutoff $h(v) = e^{-v^2}$, it was chosen mainly for mathematical convenience,[9] and as an alternative to the single exponential form. However, it exhibits a sharper crossover than the single exponential. An even sharper crossover can be obtained using the stretched exponential, $h(v) = e^{-\alpha v^\beta}$. Mountain and Mulholland used this form to fit a set of

computer–simulated DLCA aggregates, and obtained α=0.2 and ω=2.5.[6] The result is shown as curve (d). The curve is very close to the power law behavior until $r/R_g \geq 0.5$, from which point it cuts off rather sharply.

A common behavior of these curves is that they all deviate from the power law dependence $\sim r^{d_f-3}$ long before $r/R_g \approx 1$ where they actually cutoff. This "crossover" region lasts more than a decade for most of the curves. This suggests that the boundary effect can only be neglected when r is considerably larger than R_g, e.g., $r<<0.1R_g$, if these models are used. In addition, this effect will also be reflected in the crossover shape of the structure factor $S(qR_g)$ when qR_g is comparable to or larger than 1.

The stretched exponential form, which is a fitted result from simulated clusters, suggests that the structure of the colloidal aggregates may have a rather sharp crossover. We take an alternative approach: instead of studying simulated clusters in real space, we fit the structure factor of these clusters in momentum space using computer simulated clusters produced under diffusion–limited conditions. We have numerically calculated the structure factor, which can be written as

$$S(qR_g) = M^{-2} < \sum_{l,m} e^{i\mathbf{q}\cdot(\mathbf{r}_l - \mathbf{r}_m)} > \tag{4.9}$$

where $\mathbf{r}_l$ is the position of lth particle in a cluster. We obtain an $S(qR_g)$ by averaging the results from 20 clusters of different masses of M=100 to 900 particles. We fit it with a polynomial form,

$$S(x) = \left(1 + \sum_{i=1}^{n} C_i x^{2i}\right)^{-d_f/2n} \tag{4.10}$$

where $x=qR_g$ and the C_i are fitting parameters. To obtain an adequate fit we find we must take a polynomial up to x^8 (n=4), in which $C_1=\frac{8}{3d_f}$ is predetermined from Guinier's Law, and C_2, C_3, C_4 are fitted with the actual shape of the structure

factor. The form thus obtained has the right asymptotic limits at small and large values of qR_g, and the higher order terms are necessary to properly fit the form of $S(qR_g)$ around qR_g=1.

Therefore, both the form of Mountain's and the form used here suggest a sharp crossover at either $r \approx R_g$ or $q \approx R_g^{-1}$ for the simulated clusters, even though the two computer simulations used different aggregation models. By comparing the two forms in the q space, as shown in Fig. 4.2, we see that they are indeed very close to each other. In addition, the power law dependence of both curves starts as early as $qR_g \approx 2$. By contrast, the dashed curve shown is a calculation using the overlapping sphere model, which deviates from the other two with a broader crossover.

In order to see whether these forms can actually describe colloidal aggregates, we need to compare them with experimental measurements. Experimentally, the shape of $S(qR_g)$ can only be directly measured when the aggregates are monodisperse, or all the clusters are of the same mass. In this case, the measured scattering intensity $I(q)$ is just N times $I_M(q)$ where N is the the number of clusters in the sample volume.

Generally, colloid aggregation produces polydisperse cluster distribution, which means clusters are different in their mass or size. If we characterize this distribution by $N(M)$, the number of clusters of mass M, then the measured scattering intensity can be expressed as a sum of $S(qR_g)$ over the cluster mass distribution $N(M)$ with the M^2 weighting:

$$I(q) = B \Sigma_M N(M) M^2 S(qR_g) \tag{4.11}$$

$$\Rightarrow \begin{cases} \Sigma\, N(M)M^2 & qR_{max} << 1 \quad (4.12a) \\ \text{for} & \\ N_0 (qa)^{-d_f} & qR_{min} >> 1 \quad (4.12b) \end{cases}$$

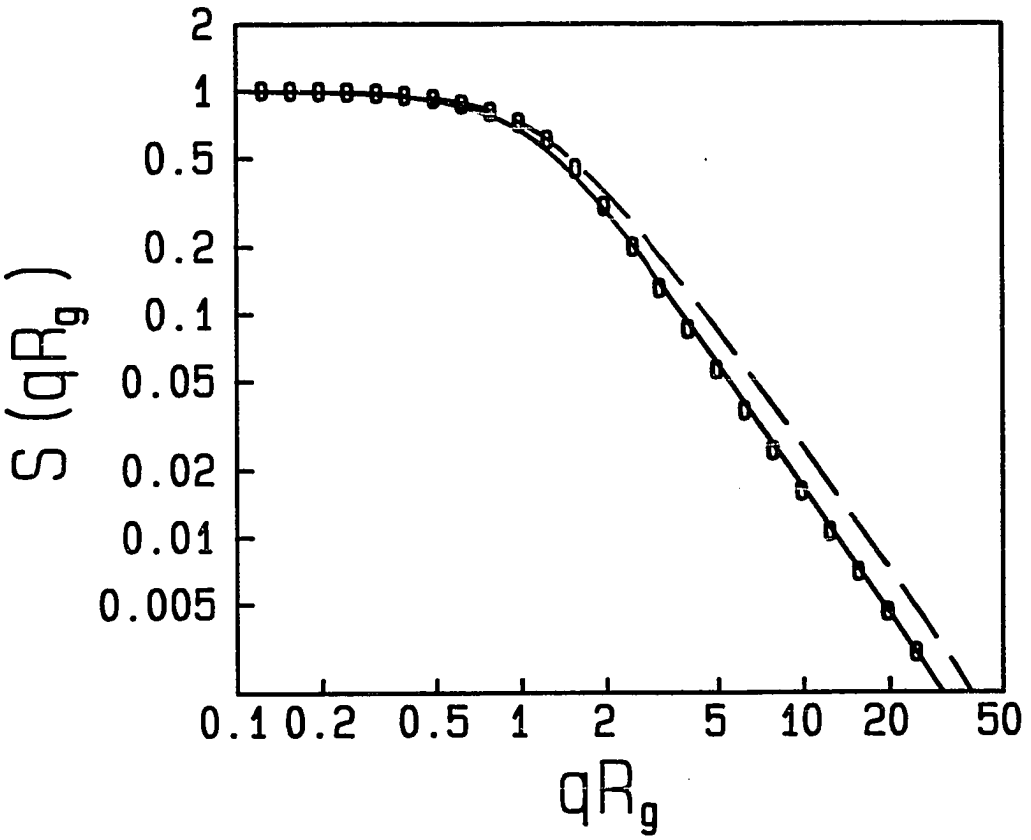

Fig. 4.2 $S(qR_g)$ obtained directly from computer generated DLCA clusters. The squares represent a fit with the polynomial form described in the text. The solid curve represents a Fourier transform of $g(r)$ with the stretched exponential cutoff, which is a result of fitting the computer generated clusters by Mountain and Mulholland. As can be seen, the two forms are in excellent agreement, and both exhibit a fairly sharp crossover around qR_g=1. For comparison, the dashed curve plotted is a calculation using the overlapping sphere model.

where $N_0=\Sigma N(M)M$ is the total mass. It can be seen that the limiting behavior of $I(q)$ is very similar to that of $S(qR_g)$ in Eq. (4.6). That is, for very small q, $I(q)$ is independent of q; for very large q, it is proportional to q^{-d_f}. However the conditions in this case are more strict: very small q means that q must be much smaller than the reciprocal of the largest cluster radius R_{max}; very large q means that q must be much larger than the reciprocal of the radius of smallest aggregates R_{min}. A consequence of these conditions is that the crossover shape of $I(q)$ between the two limiting regions can be very different from that of $S(qR_g)$. It is more smooth and extends over a larger q interval. In other words, the shape is smeared by the effect of the cluster mass distribution. It depends on the shape of $S(qR_g)$, as well as the shape of the cluster mass distribution $N(M)$. Thus, a proper comparison of the theory with experiment measurements must use Eq. (4.11) to actually sum over the cluster mass distribution.

A form of the cluster mass distribution is therefore needed to actually compare the calculation with the measured data. We will use the forms predicted from solutions to the Smoluchowski equations.[10] For DLCA we assume a constant kernel to the equations which gives

$$N(M) = A_1 M_2^{-1}(1 - 2M_2^{-1})^{M-1} \tag{4.13}$$

For RLCA, a sum kernel $K_{ij} \sim i+j$ yields

$$N(M) = A_2 M^{-\tau} e^{-M/2M_2} \tag{4.14}$$

In both cases, the normalization constants can be determined such that the total mass N_0 is conserved, and

$$M_2(t_a) = \Sigma N(M)M^2/N_0, \tag{4.15}$$

which is the second moment of the distribution, reflects the time t_a dependence of the cluster mass distribution and represents an average cluster mass. Both forms of the cluster mass distribution have been shown to be in good agreement with the measured $N(M)$ of several different colloid systems,[11-13] produced by both the DLCA

and the RLCA regimes. For DLCA, a simple relation can be found for M_2 and the average mass defined in the normal way, $M_2=\frac{1}{2}\overline{M}$ where $\overline{M}=N_0/\Sigma N(M)$. For RLCA, however, the total number of clusters $\Sigma N(M)$ is weighted too heavily toward the small masses by the power law shape, and hence does not properly reflect the time dependence of the cluster mass distribution.

4.3 EXPERIMENT AND RESULTS

We use colloidal gold as our experimental system.[14] It contains very monodisperse gold particles of radius about 7.5 nm and has a volume fraction of 10^{-6} before the aggregation. Pyridine is used to induce the aggregation. The aggregation process is very reproducible and the kinetics can be easily controlled. Depending on the amount of pyridine added, the aggregation rate can vary by several orders of magnitude, allowing both the diffusion–limited regime (DLCA) and the reaction–limited regime (RLCA) to be investigated. In addition, the gold particles have a high scattering cross section, which helps to reduce possible complications due to parasitic scattering from dust particles and other sources of noise at small angle, allowing signals to be collected when the aggregates are very small. Since the measurement takes time to average $I(q)$, while an aggregation process goes continuously, the aggregation must be stopped before making the measurement. This can be done easily with colloidal gold by adding a small amount of surfactant to the solution. The surfactant molecules stick to the surface of the gold particles, preventing further aggregation by sterically stabilizing the clusters. The surfactant layer is so thin that it has no measurable effect on either static or dynamic scattering. All DLCA data were obtained using this method, since the aggregation rate is so fast. For RLCA, the aggregation is substantially slower, lasting from several hours to a day. Thus the measurements are obtained from the sample while the aggregation progresses. For the same reason, we can make

measurements for other colloids in this regime even if their aggregation cannot be easily stopped.

We use an Ar^+ laser of wavelength λ=488 nm, and a goniometer carrying optical detectors to measure the scattering intensity $I(q)$ as function of the scattering angle θ, where $q=(4\pi n/\lambda)\sin(\theta/2)$ and n is the index of refraction of water. With an angular scan from $\theta=10^{\circ}$ to $\theta=150^{\circ}$, a range of q=0.003 nm^{-1} to q=0.03 nm^{-1} can be obtained. The goniometer is well aligned for these measurements. Toluene is used as the alignment sample (Rayleigh scatterers). We ensure that $I(q)$ measured from toluene is flat, to within a random fluctuation of ±3%. In principle, a wider q range can be achieved by going to smaller angles; practically, it is difficult to go below 10° because of the inevitable small amount of dust particles present, as well as flare due to slight misalignment, and the finite size of the laser beam.

We show our measurements of $I(q)$ taken with the diffusion–limited aggregation in Fig. 4.3(a). Four sets of data are plotted to show the evolution of the shape of the scattering with time. The unit of the intensity is arbitrary, but the curves are normalized according to the incident power and absorption so that they can be directly compared. The linear part in each curve representing the power law dependence at large q is developing successively, and it ultimately expands to the entire measurable q range as shown by the upper most curve. The fractal dimension d_f=1.86 can be determined there from the slope, therefore the only adjustable parameter in fitting the other data is the average mass M_2 characterizing the cluster mass distribution Eq. (4.13). The solid curves are calculations, with fitted values of M_2 labeled. The structure factor used in the calculations is the functional form Eq. (4.10) with C_2=2.50, C_3=–1.52 and C_4=1.02 obtained using computer–simulated DLCA clusters. The agreement between the theory and the measured data is surprisingly good, indicating that the computer simulation does a very good job in

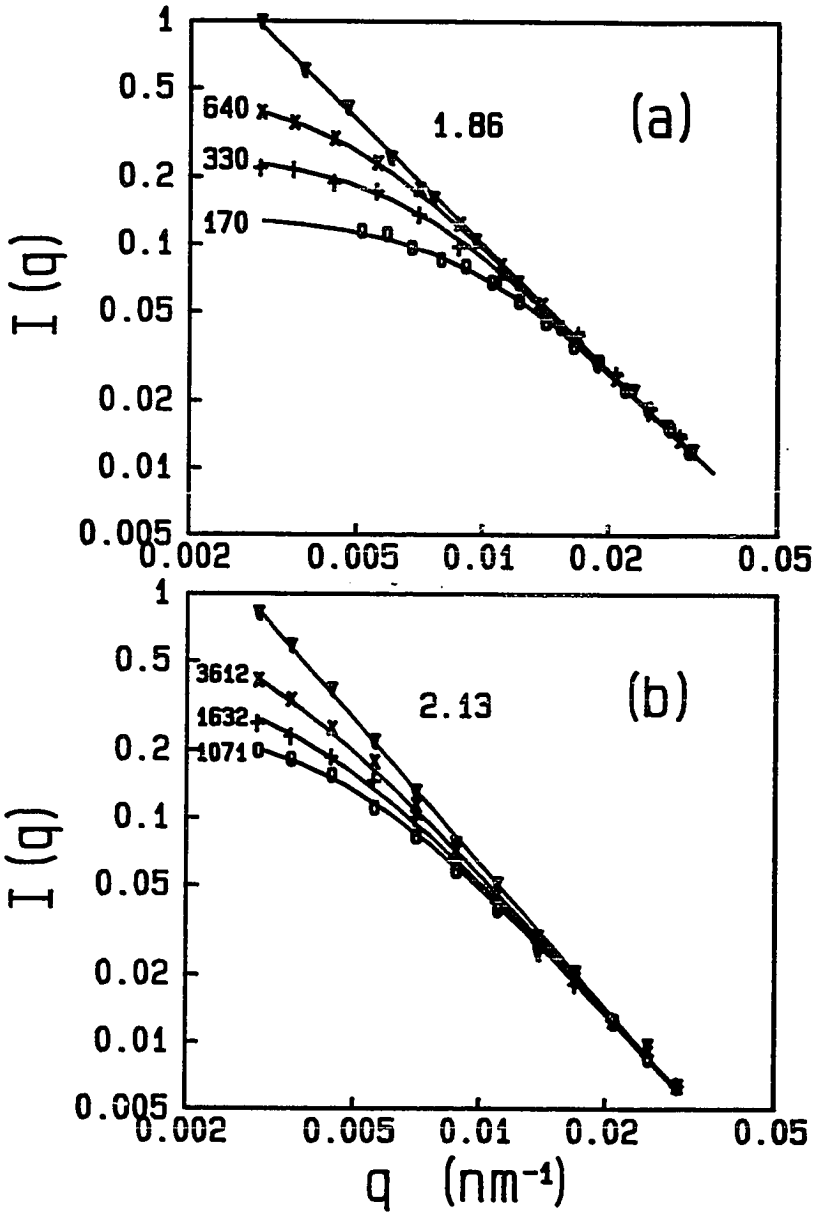

Fig. 4.3 The scattering intensity $I(q)$ obtained with colloidal gold aggregated by (a) DLCA and (b) RLCA. In each figure, different symbols represent data taken at different aggregation times t_a. The solid curves are the calculations using Eqs. (4.10)–(4.14). The values of M_2 obtained in the fitting are labeled with each curve, except the upmost curves, which are linear, giving the fractal dimension d_f=1.86 for DLCA and d_f=2.13 for RLCA. $I(q)$ is in arbitrary units.

predicting the radially averaged structural properties. It not only fits the data extremely well, but also follows the growth as the aggregation progresses, until the power law dependence expands to the entire range of q measured.

Similar data are obtained for the other regime of aggregation, RLCA. They are plotted in Fig. 4.3(b) with the calculated curves. The same functional form for the structure factor is used for the calculations, with different values for the fitting parameters. We obtain d_f=2.11 from the upper most curve; C_2=3.13, C_3=–2.58, C_4=0.95 are again results from computer simulations. As can be seen, the fits are also excellent.

It should be mentioned that, using the same forms for the structure factor and cluster mass distribution, with additional information of the structure anisotropy, we can also predict the behavior of the dynamic scattering from these aggregates. We have shown elsewhere[15] that indeed our predictions are in good accord with both static and dynamic scattering data measured concurrently from the same aggregation samples. The self–consistency of the two measurements shows that our form for the structure factor is very reasonable, and the average mass obtained from the fitting is thus a reliable quantity.

With Figs. 4.3(a) and 4.3(b), from the data measured and the average cluster mass obtained from the fitting, we can estimate the condition of Eq. (4.12b), or the critical values of $q\overline{R}_g$, above which the measured $I(q)$ becomes a power law. For this purpose, we define an average radius of gyration as

$$\overline{R}_g = aM_2^{1/d_f} \tag{4.16}$$

Since M_2 is defined in Eq. (4.15) as the second moment of the cluster mass distribution, $\overline{R}_g$ is then also a well defined quantity which reflects the time dependence of the cluster mass distribution. By comparing the critical values of $q\overline{R}_g$ obtained for the two regimes, we can see that the different distributions give different smearing effects to the measured $I(q)$. For DLCA (Fig. 4.3(a)), the

crossover is relatively sharp, and the linear behavior at large q is obvious for all curves. If the q range could be extended to $q \approx 0.002$ nm^{-1}, both q–independent and linear regions could be measured. A rough estimate from the lower curves suggests that for $q\overline{R}>3$, the curves start to become linear, and for $q\overline{R}<0.2$, they enter the q–independent region. These are much weaker conditions than stated in Eq. (4.15), and the crossover region extends over only about a decade of q, which reflects the relatively small effect of the cluster mass distribution for DLCA. This is because that the distribution, described by Eq. (4.13), is nearly flat up to a cutoff mass. With the M^2 weighting in Eq. (4.11), this causes the intensity $I(q)$ to be dominated by the clusters of large mass.

The result is quite different in the case of the other regime, RLCA. Figure 4.3(b) shows that all three lower curves do not appear to be independent of q at small q, and none of them becomes linear at large q until $q>0.025$ nm^{-1}, as can be seen by comparison to the upper most curve which is linear. The crossover region is thus much wider than in DLCA. It can be estimated from the figure that $q\overline{R}_g$ has to be >8 for the power law dependence to appear. Nevertheless, it is still a weaker condition than $qR_{min}>>1$, since the minimum R_g in this regime is a, the monomer size. There is always a non–negligible amount of small clusters present, including the monomers, which do not exhibit fractal scaling. The reason that q^{-d_f} dependence can still be measured from the scattering intensity $I(q)$ is that the weighting factor M^2 in $I_M(q)$ due to individual clusters cancels the effect of the negative power law from the cluster mass distribution, $N(M) \sim M^{-\tau}$, thus making the large clusters still the dominant. However, when the distribution exponent $\tau>2$, which exceeds the M^2 factor, the q^{-d_f} dependence will never be observed. Instead, $I(q) \sim q^{d_f(3-\tau)}$.[9] In the case of RLCA regime, it has been shown that $\tau \approx 1.5$ for the aggregates of colloidal gold.[12] Using dynamic light scattering, it has also been shown that this value for the cluster distribution exponent is universal for other colloidal

aggregates produced under reaction–limited conditions.[15] Thus the fractal dimension *can* be measured from the slope of the $I(q)$ plotted logarithmically as soon as it appears linear, or, when $q\overline{R}_g >> 1$. The measured value from the upper most curve in Fig. 4.3(b) gives $d_f \approx 2.11$, which agrees with previously reported experimental measurements[16] and computer simulation results.[17]

The same sort of measurements can be done with other colloids, especially for RLCA, which is very slow, allowing data to be taken without stopping the aggregation process. We show in Fig. 4.4 a similar result obtained with colloidal silica, aggregated under reaction–limited conditions. Again we are able to fit the data very well using the same expressions for $I(q)$. This provides additional evidence of the universality of colloid aggregation, further supporting the results of dynamic light scattering study.

We want to point out that all calculated results used above are from a fitted functional form, Eq. (4.7), with parameters obtained from computer–simulated clusters. We have also tried to fit the scattering data using the available models discussed in the previous section. The fits to $I(q)$ are markedly poorer. An example using the overlapping sphere model is shown in Fig. 4.5, in which the calculated curve cannot fit the sharp shape of the data at the crossover. Similar results are seen using the single exponential model and the Fisher–Burford form. However, we note that if no cluster mass distribution is used, and the data is fit with a form, $I(q) \propto \overline{M}^2 S(q\overline{R}_g)$, these models do fit the data reasonably well, especially for data taken with aggregates produced with RLCA. Such a fitted form, $S(q\overline{R}_g)$, only reflects the shape of an "average" structure factor *after* the smearing effect by the cluster mass distribution, and the average $\overline{R}_g$ thus obtained lacks a well defined physical meaning.

We conclude that the best forms for the structure factor of the colloidal aggregates formed in both aggregation regimes are the functional forms drawn from

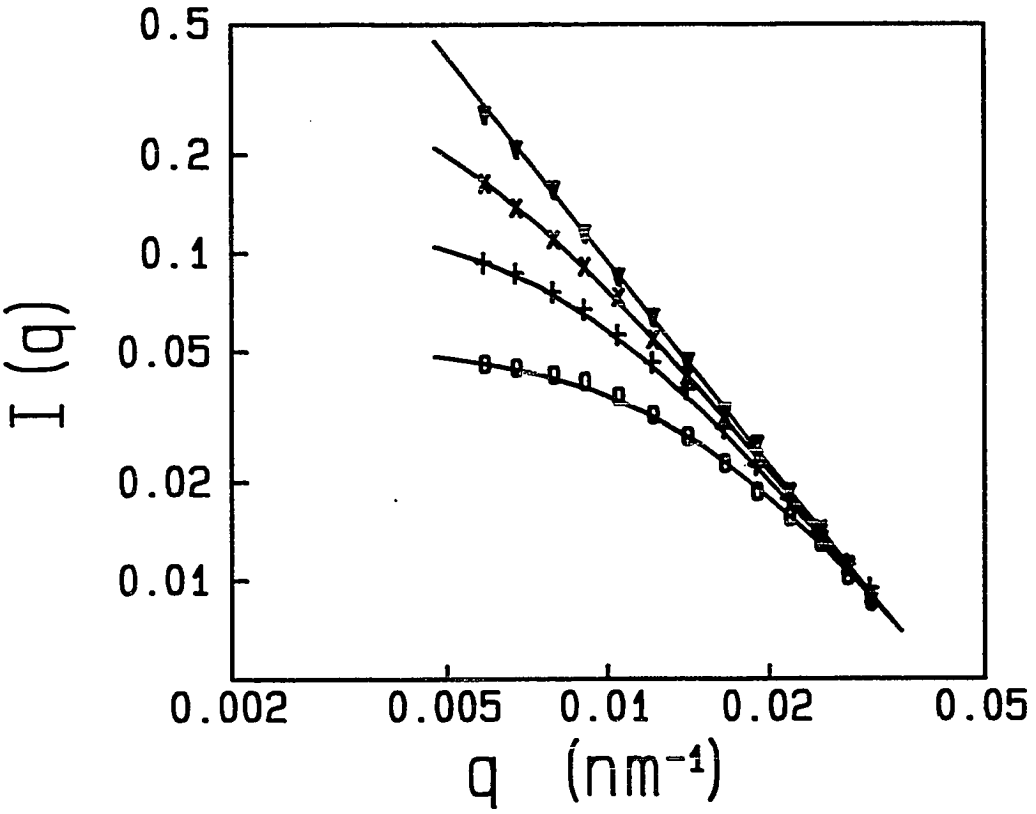

Fig. 4.4 Scattering intensity $I(q)$ obtained with colloidal silica aggregated by RLCA. It is similar to Fig. 4.3.

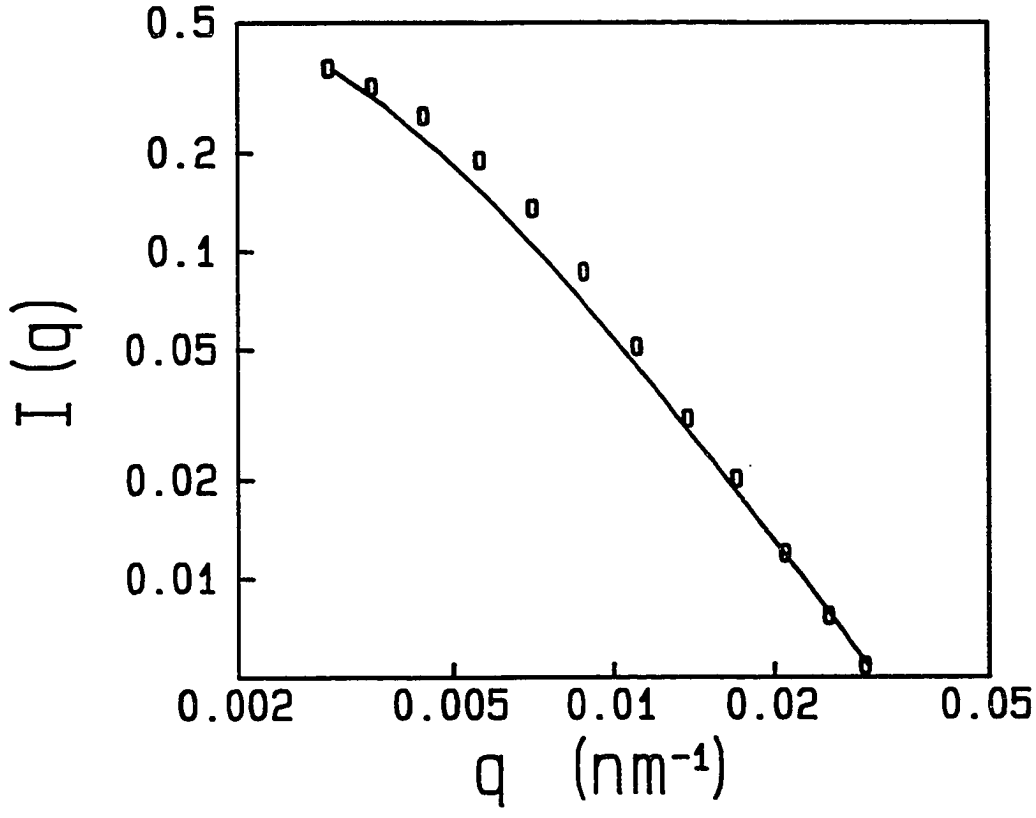

Fig. 4.5 A trial to fit the scattering intensity $I(q)$ (squares) using the overlapping sphere model (solid curve). As can be seen, the calculation do not fit the data very well.

computer simulation results. They contain high order terms of qR_g needed to reflect the actual sharp crossover of the structure factor at $qR_g \approx 1$. The forms of the structure factor using other models can fit the shape of $I(q)$ reasonably well, but fail to describe the structure factor of individual clusters.

4.4 STRUCTURE RESTRUCTURING OF FRACTAL AGGREGATES

In this section, we apply the technique of static light scattering to study the mechanical properties of the fractal colloidal aggregates. With the knowledge of the static light scattering from the colloidal aggregates, we are able to apply this technique to more fundamental physical properties of the fractal aggregates, which is crucial not only from scientific interest, but also because of the technological importance of the fractal materials, which are products of numerous random growth processes in industrial applications and in nature.

A basic difference in the structure of fractal objects from ordinary materials is their very tenuous nature. Therefore we might expect them to be quite susceptible to deformation under external forces. A recent calculation of the mechanical properties of colloidal aggregates showed that they could possess a fractal structure only up to some critical size where upon they become unstable to either thermal fluctuations or gravitational distortion.[18] In this section we discuss the effect of external stress on the structure of the aggregates and the consequences on the static light scattering from them.

We again use colloidal gold as a prototypic system in our experiments. The aggregation kinetics can be readily controlled which yields aggregate clusters with different fractal dimensions and known cluster mass distributions. In addition, the aggregation can be stopped by addition of surfactant, enabling clusters of different sizes to be obtained for investigation.

Neither thermal fluctuations nor gravity cause deformation of the fractal

structure of the colloidal gold aggregates when their size is sufficiently small to avoid sedimentation. Therefore we apply an external shear stress to the clusters in our experiments. We use aggregates formed by DLCA, as they are nearly monodisperse, thus minimizing complications due to polydispersity. Clusters were first aggregated until the characteristic cluster radius was roughly 1000 nm, as measured by dynamic light scattering. Then, a controlled amount of shear stress was applied to the clusters by forcing them to flow through a narrow tube. The maximum shear stress applied, σ_m, depends on the tube radius b and the flow rate Φ,

$$\sigma_m = \gamma\eta = \frac{4\Phi\eta}{\pi b^3}, \tag{4.17}$$

where γ is the shear rate and η is the viscosity. The tube radius used was less than 0.5 mm and the time the aggregates are in the tube was very short (<0.5 sec), thus no aggregation occurred during the shearing. Immediately after the shearing, the aggregation was stopped by addition of surfactant.

The q dependence of the scattering intensity was measured and compared with that obtained from the same colloid not subjected to shear. An example of the results is shown in Fig. 4.6. The lower curve is from the unsheared aggregates, and exhibits the expected linear behavior, giving a fractal dimension of d_f=1.84. By contrast, the scattering from aggregates subjected to a maximum shear of about 290 dynes/cm^2, shown in the upper curve, which is shifted for clarity, no longer exhibits a simple linear shape. Instead, there is a distinct kink in the curve at $q\sim$0.008 nm^{-1}, which corresponds to a length of about 130 nm. At large q the scattering still has the same slope as that from unsheared clusters; however, at small q the slope of the scattering has markedly increased, although it is not really possible to describe it as linear on the logarithmic plot given the limited range of q probed.

The change in the scattering results from shear–induced restructuring of the tenuous fractal structure of the clusters. A plausible picture of the effects of the

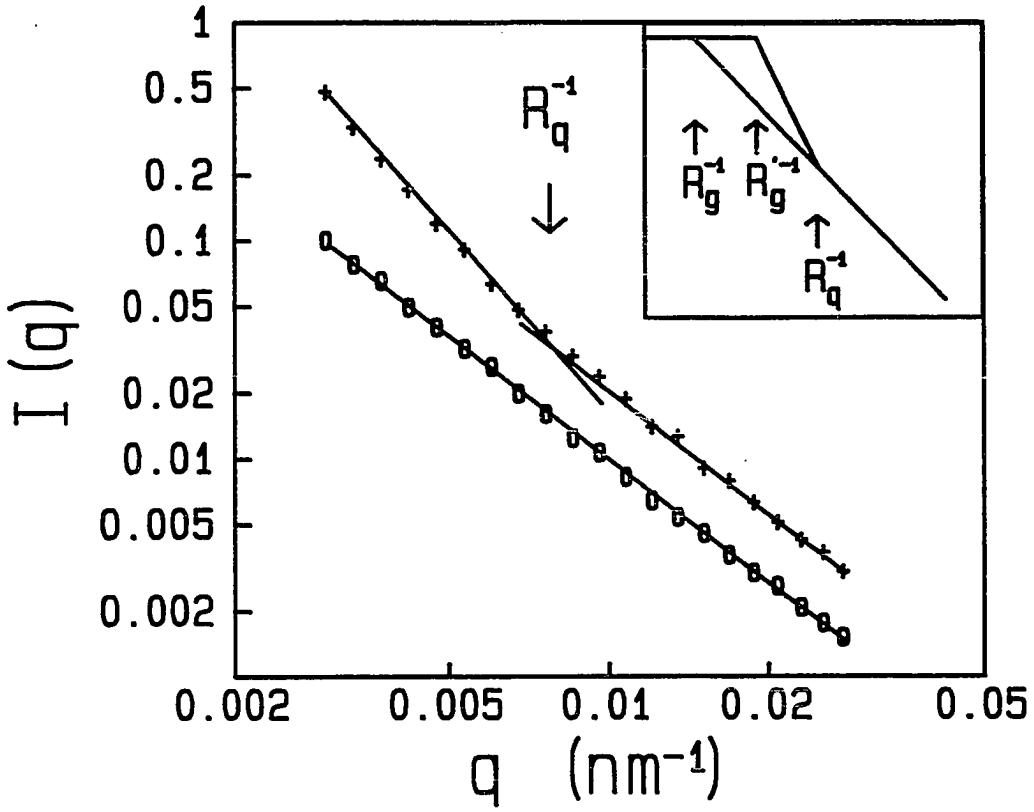

Fig. 4.6 A logarithmic plot of the scattering intensity from DLCA gold clusters before (squares, lower curve) and after (pluses, upper curve) being subjected to shear. The shear causes restructuring of the fractal shape, changing the slope of the scattering at low q. The inset shows schematically the expected effect of the restructuring on the scattering.

shear is that it causes the fractal aggregates to bend or deform, causing loops to be formed, and therefore strengthening the structure. These loops would tend to be formed on larger length scales, where the structure is weaker. Below a certain length scale, the aggregates are strong enough to withstand the shear to which they are subjected, so the original fractal correlation persists.

Another possibility is that shear causes the clusters to break apart, with the weak arms falling off. Using dynamic light scattering to measure the average hydrodynamic radius, $\overline{R}$, we do not see any substantial change in $\overline{R}$ after the shearing. This possibility can also be ruled out by experiments in which we add the surfactant first and then apply shear to the clusters. In this case we do not see any shear–induced change in the static scattering. Since the surfactant–coated clusters are no longer "sticky" they cannot form the permanent loops necessary for the restructuring. By contrast, if our observations were caused by cluster break–up, the addition of surfactant should have had no discernible effect.

Since the fractal behavior of the structure is modified, and it is no longer scale invariant over the q range probed, we cannot express the structure factor as function of qR_g. In stead, we expect a different shape of the structure factor for the sheared aggregates of different sizes. The expected effects of this restructuring on the structure factor of the aggregates is shown schematically in the inset of Fig. 4.6. The unsheared aggregates exhibit a power law behavior in the fractal regime, with $S(q) \sim q^{-d_f}$, until $q \approx R_g^{-1}$, then crossover to the q independent regime. For the sheared aggregates, below certain characteristic length scale R_q the structure is robust and remains fractal, the structure factor is unchanged for $q > R_q^{-1}$. However, the formation of loops will result in a decrease in R_g to R_g', so that the q independent regime will have to extend to a larger $q \approx R_g'^{-1}$. Then, to join properly with the fractal regime, the scattering in the region of q which probes the length scales that have been substantially restructured will have to have a larger slope, as

shown by the dashed line in the Figure. If this region matches that probed in our light scattering experiments, this simple argument would account for the behavior observed. The distinct kink between the two linear behavior regions exhibited in the measured $I(q)$ implies that the length scale R_q is universal for the different sizes of clusters within the distribution when they are subjected to the same amount of maximum shear.

A consequence of this picture is that the degree of the restructuring depends on the initial size of the cluster R_g, and the magnitude of the shear stress applied. This is indeed what we observe: the apparent slope of the low q scattering increases with the magnitude of the applied shear and the size of the clusters. To compare the effects under different amount of stress, we measure the asymptotic slopes at both small and large q from plots similar to Fig. 4.6, and then measure a crossover radius R_q, given by the inverse of the value of q, where the two slopes intercept (see Fig. 4.6). We plot the magnitude of the slope at small q as function of the shear stress in Fig. 4.7(a). These slopes are all larger than 1.84, the original fractal dimension, and, as shear increases, the slope also increases, implying a decreasing R_g' in order to resist the increasing stress. For clusters with smaller initial radius ($\overline{R}\approx$500 nm, represented by the crosses), the slopes are smaller, because of more limited range of restructuring. In Fig. 4.7(b), we plot R_q, the crossover radius as a function of shear stress σ_m for the same two sets of clusters. For the larger clusters R_q goes down as shear increases, indicating that restructuring is affecting smaller length scales. However, as the stress increases above 700 dynes/cm^2, R_q apparently saturates at about 100 nm, which corresponds to about 12 particle radii. This length scale seems to be independent of the initial cluster size, as can be seen from the data obtained with smaller clusters (crosses), which shows little dependence on the shear stress.

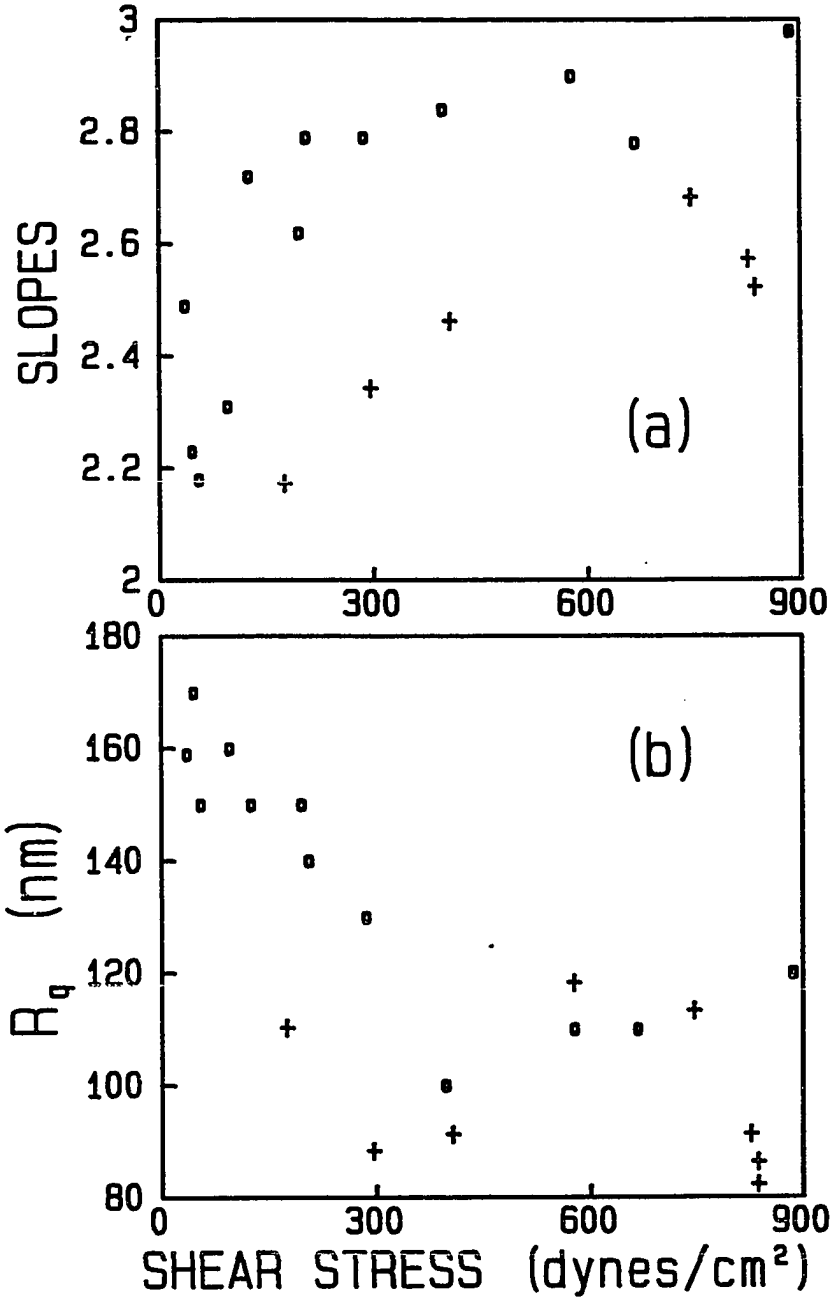

Fig. 4.7 The effects of applied shear stress on DLCA gold clusters as seen in the static light scattering, (a) the slope at low q, and (b) the crossover radius, both measured from the scattering data plots similar to Fig. 4.6. In both figures, the squares are for clusters with a characteristic radius $\overline{R}\approx$1000 nm, and the pluses are for clusters with $\overline{R}\approx$500 nm.

4.5 CONCLUSION

In this chapter, we focused on an important feature of the static light scattering technique: the crossover region that reflects the finite size of the clusters. It is this region that distinguishes the shape of the measured scattering intensity from the structure factor of the individual aggregates. The shape of the intensity is smeared by the polydispersity in the cluster mass distribution, making it more smooth and extend over a wider q range than the structure factor of individual clusters. Thus to properly study the behavior of the static scattering intensity, the effect of the cluster mass distribution must be properly included.

This is evidenced by our measurements of the scattering intensity from clusters formed by both DLCA and RLCA. For DLCA, the cluster mass distribution is relatively monodisperse, which results in a small smearing effect in the measured scattering intensity. For RLCA, however, the shape of the crossover of the scattering intensity is much more smooth and much wider, because of the highly polydisperse, power–law cluster mass distribution. The q^{-d_f} dependence of the scattering intensity can still be observed, provided q is sufficiently large.

The experimental observations are well described by our calculations using results of computer simulations. The structure factors calculated from the simulated clusters in both regimes reflect the sharp crossover around $qR_g \approx 1$. Other available models, however, do not posses this sharp crossover, although they do have the right forms at both limits of q. They can fit the shape of the measured scattering intensity, as a smeared average structure factor of the aggregates, but fail to predict the shape of the structure factor of the individual aggregates.

Finally, we have applied static light scattering technique to study the restructuring of the colloidal aggregates. The change in the scattering from the aggregates subject to an external shear stress clearly reflects restructuring at large length scales, while at small length scales the original fractal correlation persists.

REFERENCES

[1]*Kinetic Aggregation and Gelation*, ed. F. Family and D. P. Landau (Elsevier, Amsterdam, 1984).

[2]T. Freltoft, J. K. Kjems and S. K. Sinha, *Phys. Rev.* **B33**, 269 (1986).

[3]G. Dietler, C. Aubert, D. S. Cannell and P. Wiltzius, *Phys. Rev. Lett.* **57**, 3117 (1986).

[4]P. Wiltzius, *Phys. Rev. Lett.* **58**, 710 (1987).

[5]A. J. Hurd and W. L. Flower, *J. Colloid Interface Sci.*, **122**, 178 (1988).

[6]R. G. Mountain and G. W. Mulholland, preprint.

[7]H. M. Lindsay, R. Klein, D. A. Weitz, M. Y. Lin and P. Meakin, *Phys. Rev.* **A38**, 2614 (1988).

[8]see Chapter 5, this volume.

[9]J. E. Martin and B. J. Ackerson, *Phys. Rev.* **A31**, 1180 (1985).

[10]R. J. Cohen and G. B. Benedek, *J. Phys. Chem* **86**, 3696 (1982).

[11]G. K. von Schulthess, G. B. Benedek and R. W. de Blois, *Macromolecules*, **13**, 939 (1980).

[12]D. A. Weitz and M. Y. Lin, *Phys. Rev. Lett.* **57**, 2037 (1986).

[13]E. Pefferkorn, C. Pichot and R. Varoqui, *J. Phys.* (France), **49**, 983 (1988).

[14]D. A. Weitz, M. Y. Lin and C. J. Sandroff, *Surface Sci.*, **158**, 147 (1985); also Chapter 2, this volume.

[15]see Chapter 5 and 6, this volume.

[16]D. A. Weitz, J. S. Huang, M. Y. Lin and J. Sung, *Phys. Rev. Lett.* **54**, 1416 (1985).

[17]W. D. Brown and R. C. Ball, *J. Phys.* **A18**, L517 (1985).

[18]Y. Kantor and T. A. Witten, *J. Phys. Lett.* **45**, L675 (1984).

CHAPTER 5

DIFFUSION–LIMITED COLLOID AGGREGATION AND ITS UNIVERSALITY STUDIED BY LIGHT SCATTERING

ABSTRACT

The process of colloid aggregation in the diffusion–limited regime (DLCA) is studied using light scattering. A detailed description is given of how the scattering results are related to the properties the aggregates. Using static light scattering, the structure factor of the aggregates is found to agree with a form determined from computer–simulated aggregates. From the data of both static and dynamic light scattering, we determine the ratio of the hydrodynamic radius to the radius of gyration of individual aggregates to be β=0.93. When the size of the aggregates is larger than the inverse of the scattering wavevector, the effects of their rotational diffusion become important for dynamic light scattering. With all these effects properly included, we can determine the average hydrodynamic radius from the data. A method is developed to scale the dynamic light scattering data onto a single master curve, whose shape is sensitive to these effects. Excellent agreement is found between our prediction of the shape of the master curve and that obtained from experiments. Furthermore, the master curves from several completely different colloids are shown to be identical. In addition, the fractal dimension measured by static light scattering and the aggregation kinetics measured by dynamic light scattering are also the same for these colloids. This provides strong evidence of the universality of the DLCA regime of colloid aggregation.

5.1 INTRODUCTION

Historically, kinetic aggregation has been widely studied, as it represents a problem in classical physics of fundamental interest, as well as a widely exploited phenomenon of technological importance. In recent years, there have been significant advances in our understanding of colloid aggregation as a kinetic growth process. The key to these advances is the recognition that the highly disordered structure of colloidal aggregates can be quantitatively characterized by its scaling behavior, and therefore is well described as a fractal. Furthermore, modern scaling concepts have found many applications in the description of the kinetics of the aggregation process.

The class of kinetic growth process most widely considered for colloid aggregation is that which begins with a suspension of monodisperse particles. Upon aggregation, these particles collide due to their Brownian motion and stick together to form clusters. The clusters themselves continue to diffuse, collide and form yet larger clusters. This process is called cluster–cluster aggregation, and is a non–equilibrium, kinetic process. It results in a polydisperse cluster mass distribution, and a complete description of the aggregation process must include a description of this distribution. The kinetics of the aggregation can then be described in terms of the time evolution of this distribution. In turn, both the kinetics and the shape of the cluster mass distribution are intrinsically related to the structure of the clusters that are ultimately formed.

Two distinct, limiting regimes of aggregation have been identified for colloids in solution.[1,2] These correspond directly to the classical regimes of rapid and slow aggregation that have been well established in the traditional colloid literature.[3] The first of these regimes results in the most rapid aggregation possible, and occurs when the aggregation rate is limited solely by the time between the collisions of the clusters due to their diffusion. This regime is called diffusion–limited cluster–

cluster aggregation (DLCA). The second limiting regime occurs when the reaction rate of two particles is much slower than the collision rate, so that a large number of collisions are required before two particles can stick together, resulting in a much slower aggregation rate. This regime is called reaction–limited cluster–cluster aggregation (RLCA).

An elegant and quite detailed picture of the cluster–cluster aggregation has evolved in recent years,[4,5] based upon theoretical advances, extensive application of computer simulations and a variety of experimental measurements. Both regimes have been shown to have rather different, yet distinct behavior in all the key features: cluster structure, cluster mass distribution, and its kinetic evolution. In experimental measurements, light scattering techniques, both static and dynamic, have frequently been used to probe these features. However, there has not been a systematic experimental study of all these features for a colloid system and their effects to the scattering results. One purpose of this chapter, is to present a detailed self–consistent description of the light scattering experiments of colloid aggregation.

Static light scattering is used to probe the fractal structure of the colloidal aggregates, and measure their fractal dimension. In particular, it is used to verify the shape of the structure factor of the individual clusters. Dynamic light scattering probes both translational and rotational diffusion of the clusters, and thus is used as a measure of the cluster size and the cluster anisotropy. We develop a description of both static and dynamic light scattering results, based on the properties for the colloidal aggregates. In addition, we develop a technique for scaling the results of dynamic light scattering onto a single master curve. The shape of this master curve is very sensitive to many of the key features of the aggregation process: the shape of the cluster mass distribution; the fractal dimension of the aggregates; the anisotropy of the aggregates; and the shape of the cluster structure factor. In addition, it provides a measure of the average size of the aggregates, and hence the aggregation

kinetics. Therefore, light scattering techniques can provide a complete description of the aggregation process.

However, the great power of the description of colloid aggregation by the two limiting regimes is the independence from the specific details of the colloid system. As such, it is universal and applicable to a wide range of colloid systems. This universality has never been verified experimentally. The other purpose of this chapter therefore, is to apply light scattering, to test this universality. The master curves from entirely different colloids are directly compared to critically evaluate the proposed universality of the aggregation processes.

Due to the difference in the features of the two limiting regimes, we focus on DLCA in this chapter. To test the universality of DLCA regime, we measure the behavior of three completely different colloids: gold, silica and polystyrene latex, all aggregated in the diffusion–limited regime. We demonstrate that the master curves of the colloids are all identical. In addition, the fractal dimensions, measured by static light scattering, and the aggregation kinetics of the colloids are all the same. Furthermore, these results are also in agreement with the predictions of the model for DLCA.

The remainder of this chapter is organized as follows: In the next section we present a brief review of our current understanding of colloid aggregation, and in particular of DLCA regime. The following section describes the details of the light scattering experiments. In the following two sections, we develop a description of the light scattering from fractal colloidal aggregates. We first discuss experimental measurements of both static and dynamic light scattering, and give a self–consistent description of the results. We then discuss the aggregation kinetics measured by the first cumulant of dynamic light scattering. By taking into account both polydispersity and rotational diffusion, an exact measure of the cluster size can be obtained. In the following section, we develop the technique of scaling the data

onto a single master curve, and calculate the expected shape. Finally, in the next section, we utilize static and dynamic light scattering and the master curves to compare the behavior of the different colloids and verify that DLCA is a universal process. A brief concluding section closes the chapter.

5.2 DIFFUSION–LIMITED COLLOID AGGREGATION

In a colloid aggregation process, aggregates with tenuous and disordered structure are formed, which, however, can be characterized by their fractal dimension, d_f. Furthermore the distribution of the cluster size is very broad. This distribution evolves with time as the aggregation progresses, and its time dependence can be described by the growth rate of the characteristic size of the clusters. The detailed structure of the aggregates is intrinsically related to the cluster mass distribution; and both are, in turn, controlled by the aggregation kinetics. Therefore, a complete description of an aggregation process in each regime, DLCA or RLCA, requires a description of the cluster structure, the aggregation kinetics, and the shape of the cluster mass distribution. The behavior of both regimes of aggregation has been studied theoretically and by means of computer simulations, as well as experimentally with several different types of colloids. Here we briefly review the results of the studies of DLCA regime.

For DLCA, computer simulations[6,7] have shown that the clusters formed are fractal, with $d_f \approx 1.8$. The fractal dimension of DLCA aggregates has been measured for several different colloids, including gold,[8] silica[9] and polystyrene.[10] Several different experimental techniques have been used, including the analysis of transmission electron micrographs (TEM), light scattering and X–ray scattering.[11] In all cases a value of $d_f \approx 1.85 \pm 0.1$ is obtained, consistent with the computer simulation results.

The cluster mass distribution, $N(M)$, which expresses the number of clusters

of mass M, can be determined from the Smoluchowski rate equations. The solution exhibits dynamic scaling,[12] and can be written as

$$N(M) = \overline{M}^{-2}\psi(M/\overline{M}) \tag{5.1}$$

where $\overline{M}$ is an average cluster mass. The shape of the distribution, determined by the scaling function $\psi(x)$, is independent of the time. The time dependence of the distribution is reflected in the moment of the distribution, $\overline{M}$, and can be characterized by a dynamic exponent, z, where $\overline{M} \sim t_a^{\,z}$, with t_a the aggregation time. To a good approximation, the shape of the cluster mass distribution of DLCA, is given by[13]

$$N(M) = \frac{N_0}{\overline{M}^2}\left(1 - \frac{1}{\overline{M}}\right)^{M-1} \tag{5.2}$$

where $N_0 = \Sigma N(M)M$, the total mass of the system. The shape of $N(M)$ as expressed by Eq. (5.2) is essentially independent of M up to $\overline{M}$, after which it decreases exponentially. The average cluster mass is defined as

$$\overline{M} = N_0/\Sigma N(M). \tag{5.3}$$

Computer simulations of DLCA predict cluster mass distributions that are in good agreement with this result.[14] Experimentally, measurements using TEM counting with colloidal gold[15] and using electrical resistance counting with latex aggregates[16] also support this result.

The time dependence of the characteristic cluster mass can also be determined by means of the Smoluchowski equations.[12,13,17] For DLCA, a linear dependence is predicted, so that $z=1$ and

$$\overline{M} = t_a/t_0 + 1. \tag{5.4a}$$

where the characteristic time is given by

$$t_0 = 3\eta V/(8k_B T N_0), \tag{5.4b}$$

with η the viscosity of the fluid and N_0/V the initial particle concentration. Computer simulations predict that $z=1$.[14] The experimental study of latex

aggregates[16] found that the total number of the clusters decreases as $N_t \sim t_a^{-1}$, thus $\overline{M} \sim N_t^{-1} \sim t_a$, resulting in $z=1$, consistent with the theoretical predictions.

The behavior of diffusion–limited aggregation of different colloids should be independent of the specifics of each colloid, and the model for DLCA should be universal. The key features characterizing this universal behavior include the aggregate structure, described by both the fractal dimension and the anisotropy of the clusters; the cluster mass distribution; and the aggregation kinetics. In this chapter, we develop a detailed description of light scattering from colloidal aggregates and show that the scattering results are very sensitive to all these features. Therefore we can use both static and dynamic light scattering to compare the behavior of completely different colloid systems, and to critically test the universality of DLCA. In addition, with this understanding, we can calculate the scattering results theoretically using the model for DLCA, and test its applicability to real systems.

5.3 EXPERIMENT METHODS

We use both static light scattering and dynamic light scattering (or quasi–elastic light scattering)[18] as our experiment methods. Static light scattering measures the time averaged scattering intensity from the sample, $I(q)$, as function of the scattering wavevector, $q = (4\pi n/\lambda)\sin(\theta/2)$, where λ is the incident wavelength, n is the index of refraction of water, and θ is the scattering angle. Dynamic scattering, by contrast, measures the temporal autocorrelation function of the scattering intensity,

$$G_2(t) = < I(t') \, I(t'+t) > \tag{5.5}$$

where t is the delay time and the brackets represent an average t'.

With our experimental setup, we can measure both static and dynamic scattering concurrently as function of the scattering angle θ, and hence the

scattering wavevector, q. We use an Argon ion laser with a wavelength λ=488 nm as the incident source. For the colloidal gold samples, which absorb the incident light, the incident intensity is maintained at less than 1 mw before entering the sample cell to avoid heating effects. A 256–channel correlator and a rotating arm goniometer carrying the detecting optics are used to measure the scattered intensity, $I(q)$, and the intensity autocorrelation function, $G_2(t)$. At each angle, the sample time of the correlator is adjusted so that the magnitude of the measured autocorrlation function decays by about one decade over the 256 channels. The baseline, B, of the autocorrelation function is determined both from the measured average intensity and from the correlator baseline channels which is delayed an additional 1028 sample times. While the two methods usually agree to within 0.5%, the average intensity is always used in the analysis. To get the first cumulant, Γ_1, of the measured $G_2(t)$, we fit the logarithm of the autocorrelation function to a third order polynomial after it is normalized by B,

$$\frac{1}{2}\ln(G_2(t)/B-1) = \Gamma_0 - \Gamma_1 t + \frac{1}{2}\Gamma_2 t^2 - \frac{1}{6}\Gamma_3 t^3. \qquad (5.6)$$

We note that the first cumulant obtained in this way is reasonable but not perfect. By increasing the order of the polynomial used in the fit, or decreasing the number of channels used, we can asymptotically approach the true value of Γ_1. By generating a $G_2(t)$ and using the same fitting procedure it shows that Eq. (5.6) yields a Γ_1 of within 3% of the true value.

The measurements can be made in two ways. As an ideal way, we make a measurement as a function of only q at a fixed aggregation time t_a if we can stop the aggregation. We can then average a long period of time to get very good quality of the autocorrelation function $G_2(t)$ over a wide range of correlation time t. The first cumulant Γ_1, however, does not change by averaging longer time, since it is the initial decay rate of $G_2(t)$, thus only depends on the shape of $G_2(t)$ at very short t. This method has been applied only to colloidal gold because we can stop the

aggregation by adding a small amount of surfactant to the solution. The surfactant molecules adsorb on the surface of the gold aggregates and the tails of these molecules repel one other, substantially reducing the stickiness of the clusters, and halting any further aggregation. In a separate experiment where we compared the measurements before and after the aggregation was stopped, to ensure that the addition of the surfactant does not alter the aggregate structure or its behavior.

An alternate way is to initiate the aggregation of the colloids in the scattering cell, and make the measurements repeatedly at several scattering angles, while the aggregation proceeds. The time required to make a complete angle scan is 8 to 15 minutes, during which the aggregates can grow substantially, so both q and t_a vary for each datum.

5.4 LIGHT SCATTERING FROM COLLOIDAL AGGREGATES

Light scattering has been widely used in probing colloid aggregation and to study the characteristic features of the aggregation. The typical radius of the colloidal particles is usually substantially less than the wavelength of light, while the aggregates usually grow to sizes considerably larger than the wavelength. Thus static light scattering provides an excellent method for probing the structure of the aggregates, and determining their fractal dimension. Dynamic light scattering probes the dynamics of the aggregating clusters, therefore provides rich information about the anisotropy of the cluster structure, the hydrodynamic radius of the clusters, as well as cluster distribution.[18] Both scattering techniques provide in situ measurements of the aggregation process.

In this section, we investigate aggregate samples for which the aggregation has been stopped at a certain time t_a and develop a consistent description of both static and dynamic light scattering. We calculate theoretically the quantities that can be experimentally measured, with the knowledge we have about the colloidal

gold system and by making extensive use of the properties of the clusters obtained from computer simulations. We compare our calculations with the data of both static and dynamic scattering measured concurrently. We show that by properly including all the effects, our calculations are in agreement with these data. In addition, by comparing the data of static and dynamic scattering, we are able to determine the ratio of the hydrodynamic radius R to the radius of gyration R_g of the individual clusters.

We use colloidal gold as the prototypic experimental system, since all the features of its aggregation are known independently. In addition, we can stop the aggregation to obtain good quality data for the full autocorrelation function, in order to compare its shape with the calculation. The high scattering cross section of gold particles enables us to extend the measurement to very early stages of the aggregation when the clusters are relatively small.

A. Static Light Scattering

The static scattering intensity $I_M(q)$ of a cluster of mass M is proportional to the Fourier transform of the pair density correlation function of this cluster. Therefore, a measure of this q dependence of the scattering intensity reveals the structural properties of the clusters and consequently, can determine the fractal dimension. However, since the clusters are polydisperse, the measured scattering intensity $I(q)$ is an average of $I_M(q)$ over the cluster mass distribution. Therefore, $I(q)$ can be written as

$$I(q) = \sum_M N(M) I_M(q) \tag{5.7}$$

where

$$I_M(q) = AM^2 S(qR_g) \tag{5.8}$$

Here A is a constant depending on the experimental conditions and the scattering cross section of individual particles. $S(qR_g)$ is the static structure factor of a cluster of a radius of gyration $R_g = aM^{1/d_f}$, where a is the monomer radius. As is expressed,

it is a function of the reduced scattering vector qR_g only.[19] Its limiting behavior is

$$S(qR_g) = \begin{cases} 1 & qR_g << 1 \\ & \text{for} \\ (qR_g)^{-d_f} & qR_g >> 1 \end{cases} \tag{5.9}$$

For $qR_g \approx 1$, the shape of $S(qR_g)$ is determined by the cutoff form of the pair density correlation function. It is obvious from Eqs. (5.7)–(5.9) that the shape of the static scattering intensity $I(q)$ is similar to $S(qR_g)$, depending on how monodisperse the cluster mass distribution $N(M)$ is. The scattering intensity also contains a q–independent region when q is very small; a power–law dependent region when q is very large; and a crossover region in between. In order to compare all three regions with the theory and to fit the data, we purposely chose a sample for which the aggregation was stopped when we could measure the crossover region of the scattering intensity. The data taken is shown in Fig. 5.1 by the squares. We can see that the crossover region extends over most of the q range measured, although at large q, it appears to be linear on the logarithmic plot.

The data is interpreted in terms of Eqs. (5.7) and (5.8). The cluster mass distribution is assumed to have a form of Eq. (5.2) for DLCA, and the average mass, $\overline{M}$, is used as the fitting parameter. For the structure factor, we use a functional form given by

$$S(x) = (1 + C_1x^2 + C_2x^4 + C_3x^6 + C_4x^8)^{-d_f/8} \tag{5.10}$$

where $x = qR_g$, $C_1 = \frac{8}{3d_f}$, and C_2, C_3 and C_4 are obtained by fitting this expansion to the structure factor calculated for computer generated DLCA clusters.[19] Eq. (5.10) has the correct asymptotic forms at both limits of x, and C_1 is determined so that Guinier's law is obeyed. The calculation using this form for the structure factor is shown by the solid line in Fig. 5.1. The fitting gives $\overline{M}$=165. As can be seen, the agreement is excellent. It is necessary to include the high order terms of qR_g in Eq. (5.10) to produce the relatively sharp crossover of the structure factor. If we

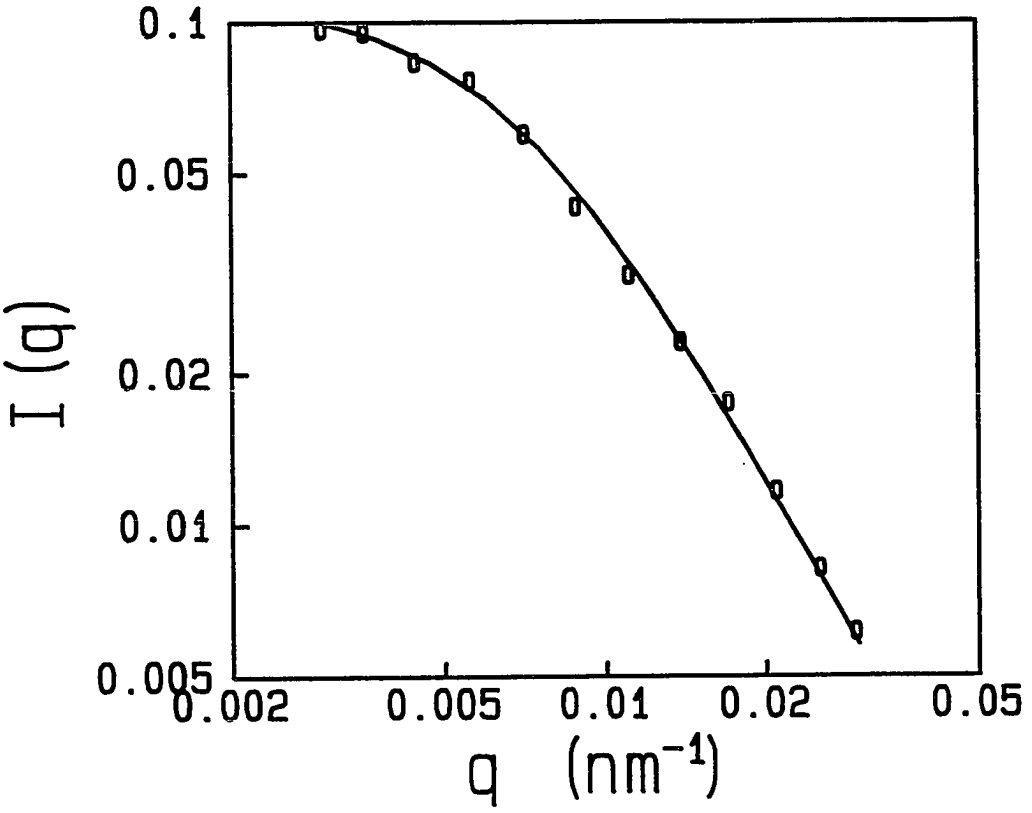

Fig. 5.1 Static light scattering intensity from colloidal gold aggregates formed by DLCA. The data were taken when the sizes of the aggregates were not large enough for the intensity to exhibit a linear fractal scaling in the logarithmic plot. The solid curve is a calculation using Eqs. (5.3), (5.7), (5.8) and (5.10). An average cluster mass of $\overline{M}$=165 is obtained from the fit.

try to use other forms for the structure factor, such as the modified Fisher–Burford form,[20] which do not have a sharp crossover around qR_g=1, the fit to the data is markedly poorer.[19,21]

The fitting parameter, $\overline{M}$, characterizes the cluster mass distribution. We will use this same parameter in fitting the results of dynamic scattering, which were measured concurrently with $I(q)$. This will provide a self–consistent picture of both scattering techniques.

B. Dynamic Light Scattering

Dynamic light scattering provides an additional, very useful experimental probe of colloid aggregates. It measures the temporal fluctuations in the scattered light intensity due to the diffusive motion of the clusters. From the decay of the autocorrelation function of these fluctuations, it is possible to determine the hydrodynamic radius of the characteristic clusters in the distribution. However, for aggregates whose size is larger than q^{-1}, not only the translational diffusion of the clusters, but also their rotational diffusion has to be considered. Since the internal fractal structure of the cluster is resolved, the scattered intensity is strongly dependent on the orientation of the cluster, and consequently fluctuates as the aggregate undergoes rotational diffusion. A calculation of the autocorrelation function therefore involves a determination of the anisotropy of the clusters.

One treatment of the effects of rotational diffusion entails the decomposition of the structure factor into spherical harmonics. For each spherical harmonic the decay rate due to rotational diffusion is known.[18] Thus, the field autocorrelation function can be expressed as

$$G_1(t) = \sum_{M,\ell} N(M)M^2 e^{-q^2 Dt} S_\ell(qR_g) e^{-\ell(\ell+1)\Theta t} \qquad (5.11)$$

Here, $S_\ell(qR_g)$ is the ℓth component (ℓ=0,1,2,...) of the spherical harmonic expansion of the structure factor and $S(qR_g) = \Sigma_\ell S_\ell(qR_g)$. The translational and rotational

diffusion coefficients of a cluster of mass M are $D=\zeta/R$ and $\Theta=\frac{3}{4}\zeta/R^3$, where $R=\beta R_g$ is the hydrodynamic radius and $\zeta=k_BT/6\pi\eta$.

From Eq. (5.11) we see that translational diffusion and rotational diffusion contribute to the autocorrelation function with different decay rates. For translational diffusion, the decay rate is $\Gamma_t=Dq^2$, and is proportional to q^2; in contrast, due to rotational diffusion each harmonic contributes with a different decay rate, $\Gamma_\ell=\ell(\ell+1)\Theta$, and is independent of q. The q dependence due to rotations is caused by the anisotropy of the structure, and thus is reflected in the components of the harmonic expansion, $S_\ell(qR_g)$.

In order to calculate the harmonic components, $S_\ell(qR_g)$, one needs to know the exact structure of the cluster, that is, the position of each particle in the cluster. Since this is not feasible for the real clusters, we again use the computer generated clusters. The results obtained by this technique are in excellent accord with experimental measurements.[22] However, this method is computationally intensive, making it relatively inflexible and difficult to apply to clusters larger than $M\approx1000$ and $qR_g>10$. Here we use an alternate approach which explicitly takes advantage of the scaling properties of the fractal clusters.

An approximation of the autocorrelation function, which is exact up to the first cumulant, can be constructed as

$$G_1(t) = \sum_M N(M)M^2S(qR_g)\, e^{-q^2D_{\text{eff}}t}, \tag{5.12}$$

where the effective diffusion coefficient $D_{\text{eff}}=Df(qR_g)$ includes the effects of both translational and rotational diffusion. The contribution to the higher cumulants due to rotational diffusion of the individual clusters is neglected. The function $f(qR_g)$, which reflects the effects of rotational diffusion to the first cumulant, can be derived from Eq. (5.11) as

$$f(qR_g) = \frac{D_{eff}}{D} = 1 + \frac{3\Sigma_\ell \ell(\ell+1)S_\ell(qR_g)}{4(\beta qR_g)^2 S(qR_g)} \tag{5.13}$$

A critical feature of $f(qR_g)$ is that it is a function of qR_g only. This means that for dynamic light scattering, as for static light scattering, the clusters can be characterized by a single length scale, R_g. At small qR_g, it has been shown that $S_\ell(qR_g<<1)\approx 0$ except for $\ell=0$. This leads to $f(qR_g<<1)=1$, as expected, since the scattered light does not resolve the anisotropy of the clusters. For $qR_g>>1$, scaling arguments show[23] that

$$f(qR_g) \approx 1 + \frac{\alpha^2}{4\beta^2} \tag{5.14}$$

where $\alpha\approx 1.5$. The shape of $f(qR_g)$ can be calculated using Eq. (5.13) with computer generated clusters. We have calculated $f(qR_g)$ for 20 clusters each of masses 100, 200, to 900 particles, and have plotted the average as a function of qR_g in Fig. 5.2. As can be seen, the curve approaches 1 when $qR_g<1$, and becomes flat when $qR_g>5$, as predicted.

After $f(qR_g)$ is determined, Eq. (5.12) can be calculated, using the same forms for $S(qR_g)$ and $N(M)$, with $\overline{M}=165$ obtained in the fit to $I(q)$. The experimentally measured $G_2(t)$ can be related to $G_1(t)$ by the Siegert relation[22,24]

$$G_2(t) = A' G_1(t)^2 + B \tag{5.15}$$

where A' is an instrument–dependent quantity and B is the baseline.

At small angles, where $q\overline{R}_g = qa\overline{M}^{1/d_f}$ is small, rotational diffusion plays almost no role, so that $\overline{D}_{eff}\approx\overline{D}=\zeta/\beta\overline{R}_g$, and the only unknown parameter is β. Thus we can obtain the experimental value for β from the fit to the autocorrelation function. This is shown in Fig. 5.3, where the autocorrelation function is measured at $\theta=15^o$, corresponding to $q=0.0045$ nm^{-1}, and $q\overline{R}_g=0.75$, taking $a=7.5$ nm for

colloidal gold. We obtain the best fit to the data using β=0.93, and the agreement between the fit and the data is so good that the fitted curve cannot be distinguished from the data. The fit includes the effects of rotations, but they play a very small role as can be seen from the dashed curve shown, which is a calculation using D_{eff}=D. The value obtained for β is in good agreement with theoretical calculations.[25,26]

At large angles, rotational diffusion plays a much more important role. This is evident in Fig. 5.4, where we show the autocorrelation function measured at 96°, corresponding to $q\bar{R}_g$=4.3. The autocorrelation function is also calculated, where there are now no unknown parameters. The calculated curve fits the data very well as can be seen from Fig. 5.4, while the dashed curve, which does not include the effects of rotational diffusion, deviates considerably from the data. For data taken at all other angles, we fix β=0.93 and use the average mass, $\bar{M}$, as the fitting parameter. The deviation in $\bar{M}$ in fitting $G_2(t)$ at different angles is very slight, as is shown in Fig. 5.5. The difference between $\bar{M}$ fitted at each angle and $\bar{M}$=165 obtained from the fit to $I(q)$ is within 3% for all the data.

Both static and dynamic light scattering techniques provide a measure of the properties of the colloidal aggregates. By assuming a form for the cluster mass distribution, we verify the form for the structure factor, and the effects of rotational diffusion. We note that we have obtained good agreement with the shape of the autocorrelation function over all time measured, despite the fact that we use only the first cumulant expansion for the decay for the individual clusters. This reflects that the decay of the autocorrelation function of individual clusters is nearly exponential, even with rotational diffusion. It is the cluster mass distribution which gives the small amount of curvature observed.

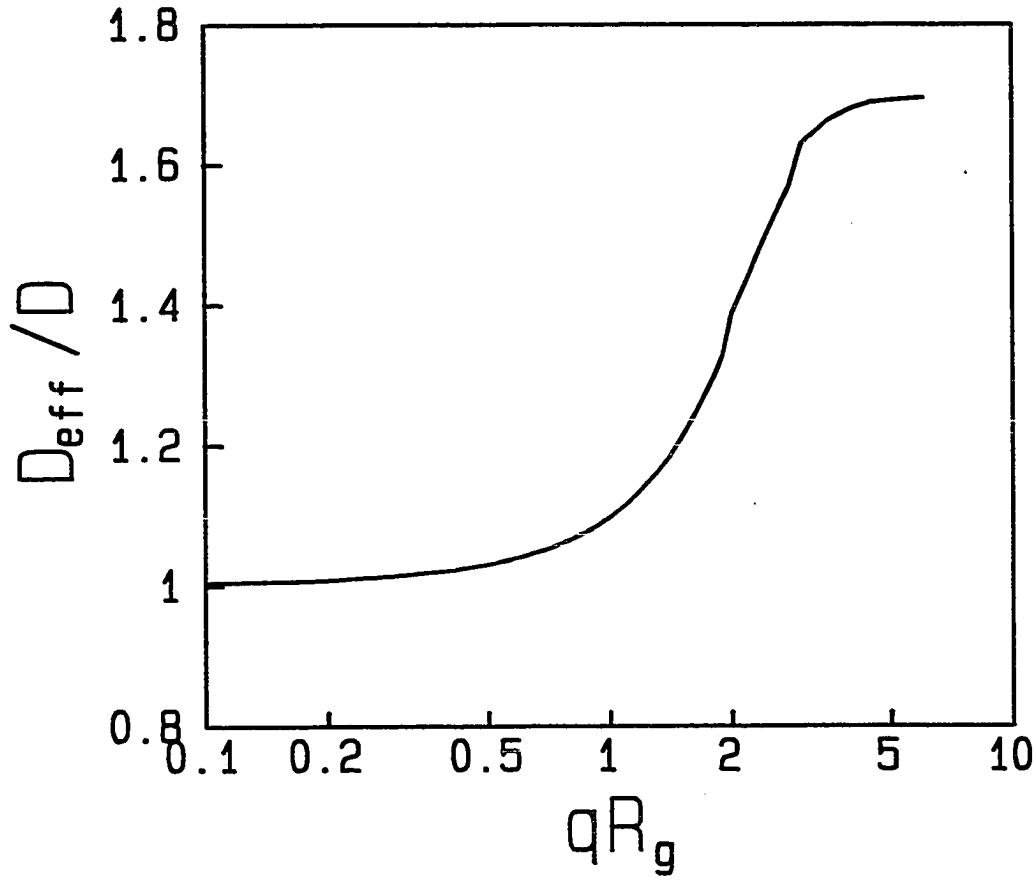

Fig. 5.2 The scaled effective diffusion coefficient, including the effects of rotational diffusion for DLCA clusters. It is an average of the calculations from nearly 200 computer generated clusters of different masses.

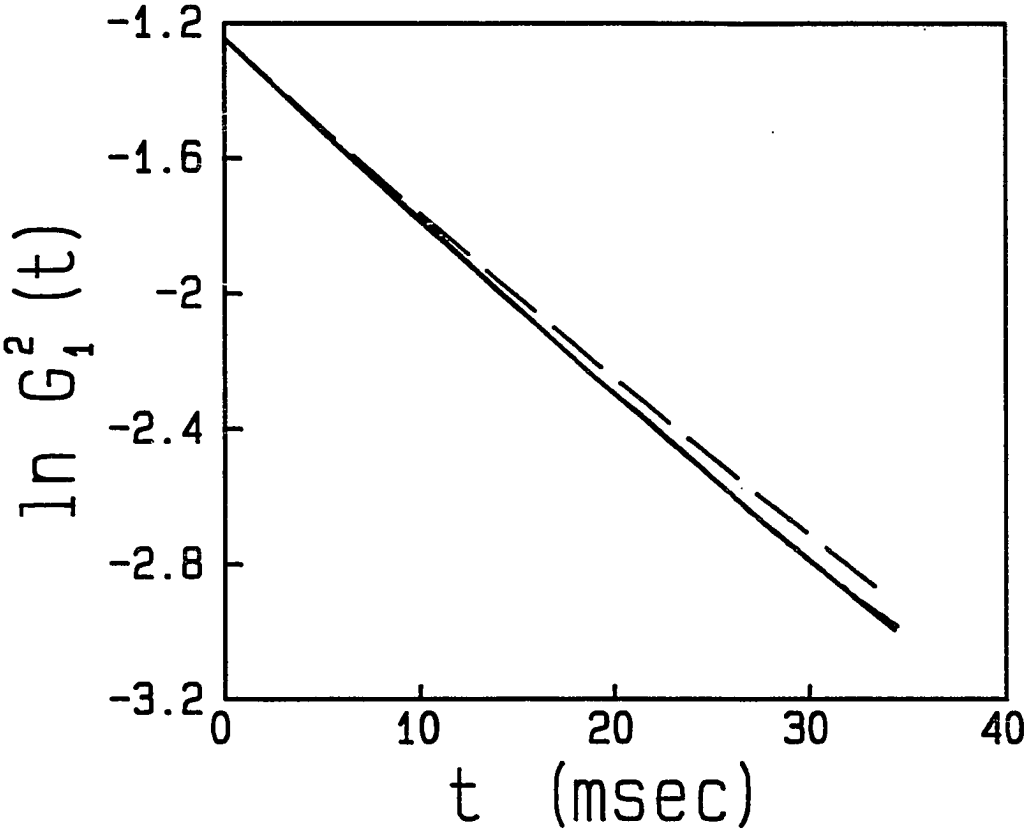

Fig. 5.3 The autocorrelation function measured at θ=15^{o} for gold DLCA aggregates. The solid curve through the data is a fit using Eq. (5.12) and D_{eff}, which includes the effects of rotational diffusion. The fit and the data cannot be distinguished. The dashed curve is the same calculation, but excludes the effects of rotational diffusion.

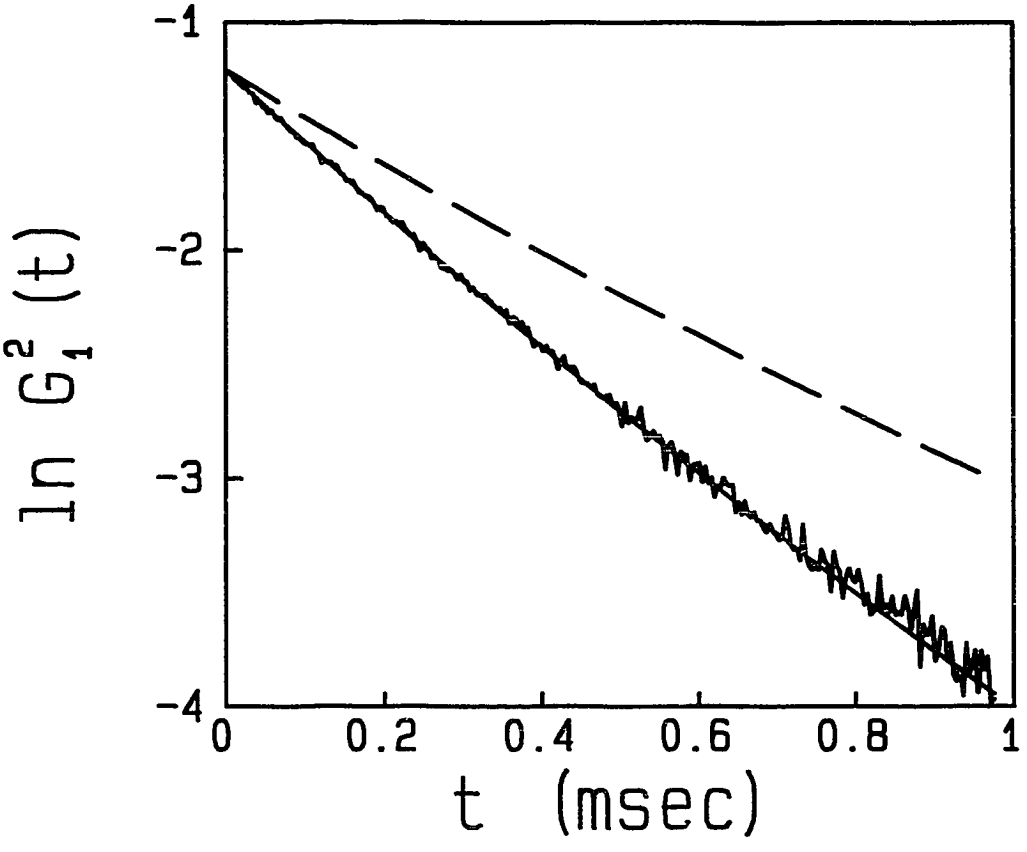

Fig. 5.4 The autocorrelation function measured at θ=96^{o} for gold DLCA aggregates. The solid curve through the data is a fit using Eq. (5.12) and D_{eff}, which includes the effects of rotational diffusion. The dashed curve is the same calculation, but excluding the effects of rotational diffusion, which are significant in this case.

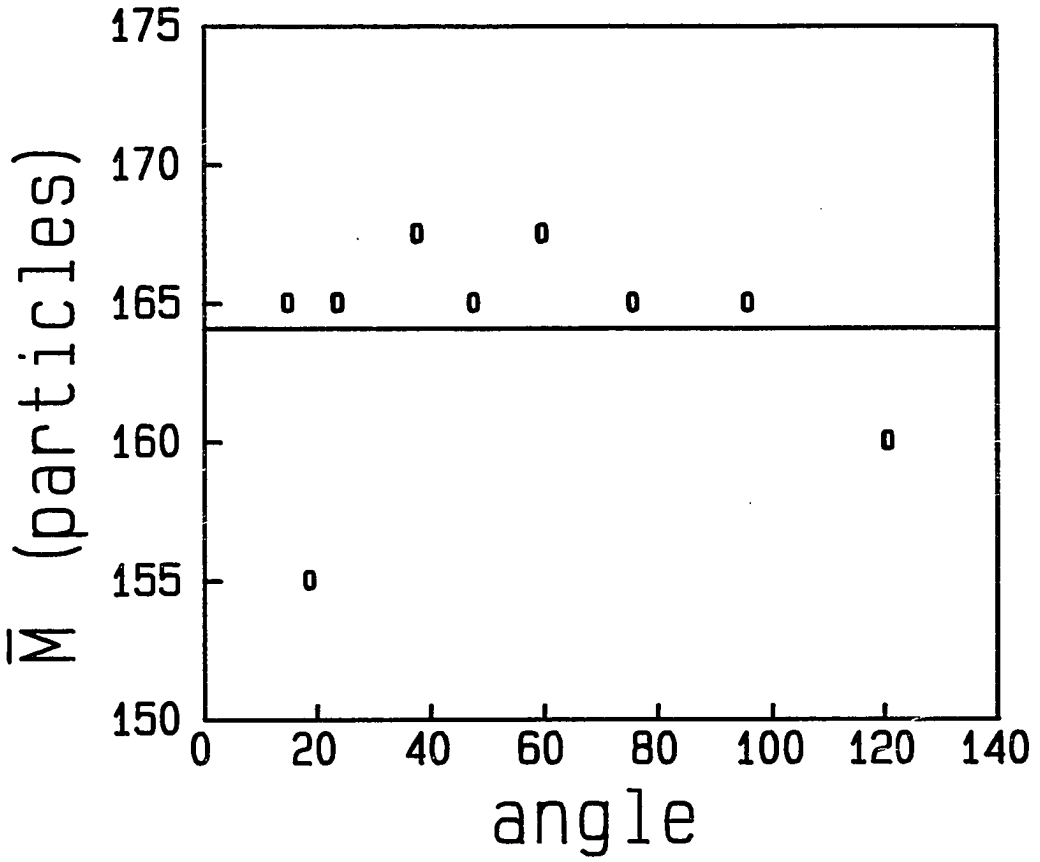

Fig. 5.5 The deviations of the fitting parameter $\overline{M}$ for the autocorrelation function at different angles. $\overline{M}$=165 is obtained in fitting $I(q)$, the static scattering intensity shown in Fig. 5.1.

5.5 AGGREGATION KINETICS

In the previous section, we study the scattering results of a single sample, where the cluster mass distribution has a characteristic radius $\overline{R}_g$ comparable to q^{-1}. This enables us to use both static and dynamic light scattering techniques to study the features of the aggregates, especially the static structure factor and the effects of rotational diffusion. We can extend this calculation of the scattering results to other times during the aggregation. However, we must know the characteristic cluster size of the distribution, as a function of the aggregation time, t_a. For monodisperse or nearly monodisperse systems with *no* effects of rotational diffusion, it can be obtained simply from the first cumulant of the autocorrelation function,

$$\Gamma_1 = \left.\frac{\partial \ln G_1(t)}{\partial t}\right|_{t=0}, \tag{5.16}$$

which can be obtained experimentally with Eq. (5.6). A radius corresponding to the characteristic cluster size can be derived from the first cumulant, as $\overline{R}=\zeta/\overline{D}=\zeta q^2/\Gamma_1$, where $\overline{D}$ is the translational diffusion coefficient of the characteristic cluster. However, as we have seen in the previous section, the effects of rotational diffusion cause a change in the shape of the autocorrelation function, therefore they also cause a change in the average radius determined from the first cumulant, which is the initial slope of the autocorrelation function. Thus, the first cumulant, when divided by q^2, only gives an *effective* average diffusion coefficient. It can be derived from Eq. (5.12) as

$$\overline{D}_{\text{eff}} = \frac{\Gamma_1}{q^2} = \frac{\Sigma_M \; N(M)M^2 S(qR_g) D_{\text{eff}}}{\Sigma_M \; N(M)M^2 S(qR_g)}. \tag{5.17}$$

Therefore, $\overline{D}_{\text{eff}}$ is an average of the effective diffusion coefficient D_{eff}, weighted by the scattering intensity and the cluster mass distribution. We note

that the orientationally averaged static structure factor is used as the intensity weighting, even though the effects of rotational diffusion are caused by the orientational anisotropy of the cluster structure. These effects are included in Eq. (5.17) only through D_{eff}, which, expressed in Eq. (5.13), is itself an average weighted by the spherical harmonic components.

Since the higher cumulants of the autocorrelation function affected by rotational diffusion do not contribute to $\overline{D}_{\text{eff}}$, Eq. (5.17) is exact. We note that $\overline{D}_{\text{eff}}$ is dependent on q. This additional q dependence is due both to the cluster mass distribution and to the contributions of rotational diffusion to D_{eff}. Even for a relatively monodisperse cluster mass distribution, such as that obtained for DLCA, the effects of rotational diffusion cause the measured $\overline{D}_{\text{eff}}$ to be dependent on q. This additional dependence is observed experimentally and is well described using the form of D_{eff} shown in Fig. 5.2.[22]

Since every quantity in Eq. (5.17) is known, we can calculate $\overline{D}_{\text{eff}}$ as a function of $\overline{M}$ and q, from which, the measured average effective radius, $\overline{R}_{\text{eff}}=\zeta/\overline{D}_{\text{eff}}$, can be obtained. Therefore, knowing the experimentally measured quantity, $\overline{D}_{\text{eff}}$ or $\overline{R}_{\text{eff}}$ at any q, we can translate to the average mass of the cluster mass distribution, $\overline{M}$, which increases with t_a, but is independent of q. Then the true size of the characteristic cluster can be calculated from $\overline{M}$ by

$$\overline{R}=\frac{\zeta}{\overline{D}}=\zeta\left[\frac{\Sigma N(M)\,M^2\,D}{\Sigma N(M)\,M^2}\right]^{-1}, \tag{5.18}$$

which is the hydrodynamic radius measured at q=0, while $\overline{D}=\overline{D}_{\text{eff}}(q=0)$ is the corresponding translational diffusion coefficient. Thus $\overline{R}$ as a function of $\overline{R}_{\text{eff}}$ can serve as a calibration, to relate the measured value to the desired value. We show this in Fig. 5.6, where $\overline{R}$ as a function of $\overline{R}_{\text{eff}}$ for $\theta=20^{\circ}$, 42°, and 111° is plotted. For comparison, the straight line is just $\overline{R}=\overline{R}_{\text{eff}}$, representing a monodisperse spherical system. As can be seen, at different angles, an effective radius $\overline{R}_{\text{eff}}$ yields

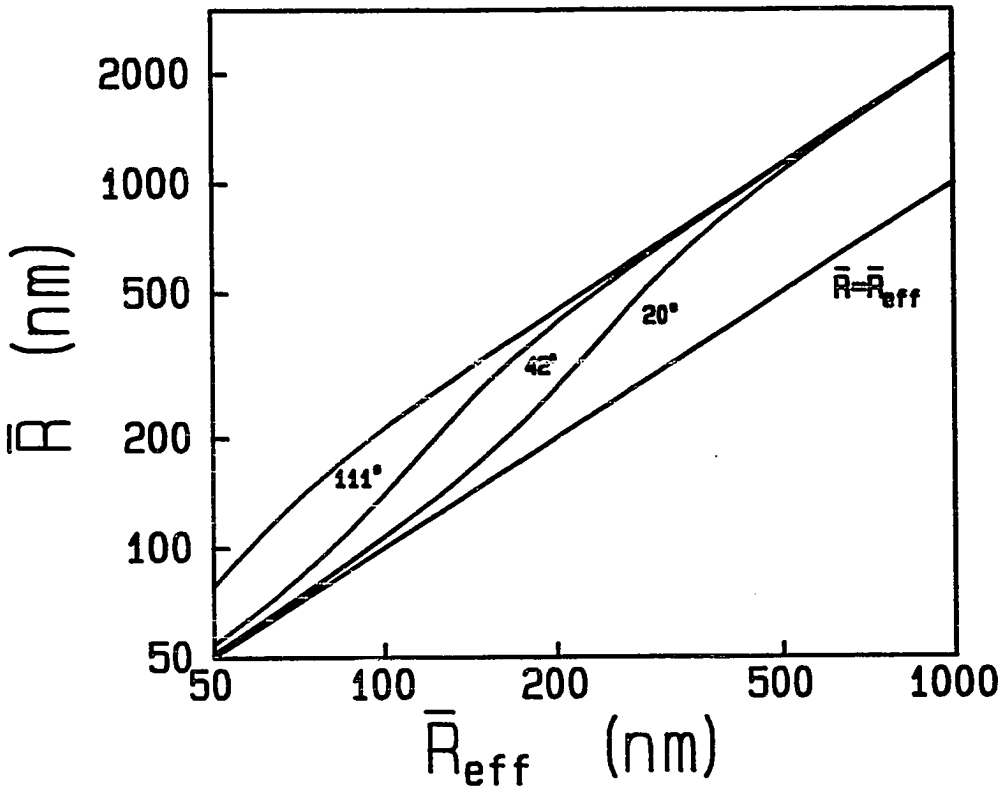

Fig. 5.6 The average hydrodynamic radius $\bar{R}$ as a function of the effective average radius $\bar{R}_{eff}=\zeta q^2/\Gamma_1$. The curves are for (from the top) $\theta=20^o$, 42^o, and 111^o. The straight line represents $\bar{R}=\bar{R}_{eff}$, hence is for monodisperse spheres only.

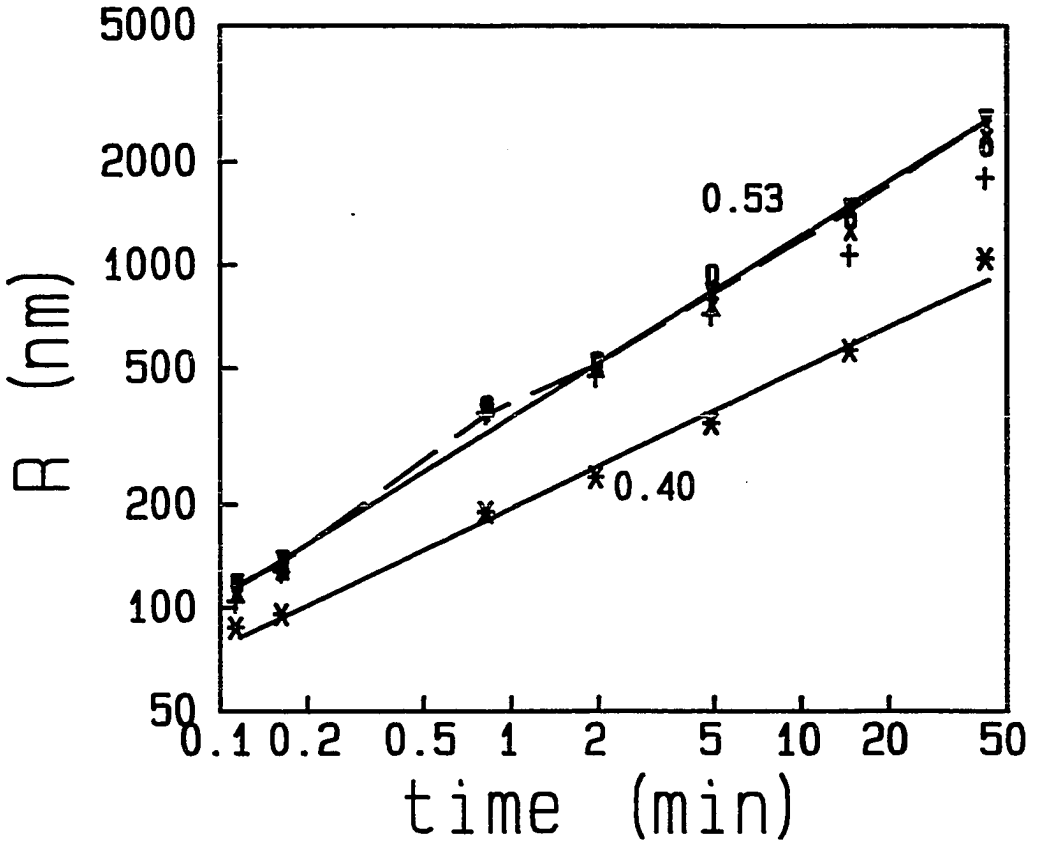

Fig. 5.7 The aggregation kinetics expressed by the average hydrodynamic radius $\overline{R}$ as a function of the aggregation time t_a. The squares (o, for θ=20°), crosses (×, for θ=42°), and pluses (+, for θ=111°) are obtained using the calibration curves of Fig. 5.6. The solid triangles connected by the dashed lines are the results from the master curve scaling (see Section 5.6). A slope of 0.53 is obtained from the solid line through the data. In comparison, $\overline{R}_{eff}$ obtained at θ=42° is also plotted. It has a smaller slope, 0.40.

different values of $\overline{R}$, reflecting the q dependence due to the effects of rotational diffusion and polydispersity. For large $\overline{R}_{eff}$, the three curves are no longer different, as they all have reached the large $q\overline{R}_g$ limit. However, the difference between $\overline{R}_{eff}$ and $\overline{R}$ is profound, as measuring $\overline{R}_{eff}$=1000 nm actually means $\overline{R}\geq$2000 nm. The additional contribution to the autocorrelation function due to rotational diffusion causes the faster decay, thus if the total decay rate is accounted for by translational diffusion only, the average size would have to be smaller, by a factor as large as 2 at large $q\overline{R}_g$, when both contributions are comparable.

The aggregation kinetics can be obtained by expressing $\overline{R}$ as a function of the aggregation time, t_a. In Fig. 5.7, values of $\overline{R}$ obtained at three angles from the measurements of colloidal gold aggregates formed by DLCA are plotted vs. t_a, on a logarithmic scale. The straight line fit determines the dynamic exponent, z. Since $\overline{R}\sim\overline{M}^{1/d_f}\sim t^{z/d_f}$, the slope gives z=0.53×1.85=0.98≈1, in agreement with the theoretical predictions[12,14,17] and the experimental results of latex aggregates.[16] By contrast, the effective radius measured at any single angle grows relatively slower. We show this in the same figure by stars for $\overline{R}_{eff}(t_a)$ taken at 42°. It also exhibits power law growth, however, but with a smaller exponent. We had previously reported[27] that this effective hydrodynamic radius measured at a single q, which was not corrected for rotational diffusion, increased as t_a^{1/d_f}. This earlier result was probably obtained using somewhat aged colloid, and was therefore not truly in the diffusion–limited regime, but was rather in the crossover between DLCA and RLCA. Nevertheless, the essential conclusion, that z=1, remains completely valid.

5.6 MASTER CURVES FOR DYNAMIC LIGHT SCATTERING

There is a considerable amount of information contained in the q dependence of the measured $\overline{D}_{eff}$. This can be seen by examining Eq. (5.17), which can be viewed as a moment of the cluster mass distribution. Both $S(qR_g)$ and

$D_{eff}=Df(qR_g)$ depend on q, which causes this moment to also vary with q. If a sufficiently small q can be achieved so that all clusters have $qR_g<<1$, then both $S(qR_g)$ and $f(qR_g)$ are equal to 1, and $\overline{D}_{eff}=\overline{D}$, which is q independent. Since $D\sim M^{-1/d_f}$, the order of the moment will be $2-1/d_f$. However, as q increases, some of the clusters become larger than q^{-1}, and the moment measured is no longer so straightforward. In this case, the q dependence will also vary with $\overline{M}$, which characterizes the cluster mass distribution, and determines the fraction of clusters having $R_g>q^{-1}$. At very large q, the result reverts to another simple moment, where now the intensity from each cluster contributes only a factor of M in the weighting. In addition, D_{eff} also becomes independent of q (see Eq. (5.14)). Thus the order of the moment measured is $1-1/d_f$.

Experimentally, only a limited range of q is accessible. However, as the aggregation proceeds, $\overline{M}$ increases with time. By taking advantage of the dynamic scaling of the cluster mass distribution, we can greatly extend the range over which the q dependence of $\overline{D}_{eff}$ can be measured with varying $\overline{M}$ or $\overline{R}$. This can be shown easily by recognizing that $\overline{D}_{eff}$, when normalized by $\overline{D}=\zeta/\overline{R}$, is a function of $q\overline{R}$ *only.* A mathematical derivation is given in the Appendix. Physically, it results from the fact that the cluster mass distribution is characterized by a single length scale, $\overline{R}$. This is due to the dynamic scaling of the distribution, by which the moment of the distribution changes with time, while the shape of the distribution keeps unchanged. Thus, any moment of the distribution which reflects the time dependence of the distribution, can be used to scale q.

We can calculate the shape of $\overline{D}_{eff}$ as a function of q in the experimentally accessible range, but for several $\overline{M}$ or $\overline{R}$, each reflecting a different stage during the aggregation process. Then we scale these separate curves to a master curve by plotting them as $\overline{D}_{eff}/\overline{D}$ as a function of $q\overline{R}$. The shape of this master curve will reflect the effects of the key features of the aggregation process on the scattering

results. To see this, we have calculated $\overline{D}_{eff}/\overline{D}$ for several different conditions, and have plotted these curves in Fig. 5.8 as a function of $q\overline{R}$. Curve (a) is a calculation with no effects from either polydispersity or rotational diffusion so that $\overline{D}_{eff}=\overline{D}$. Hence it applies only to monodisperse spheres and is flat. Curve (b) takes into account the $N(M)$ of DLCA, but uses $D_{eff}=D$, thus ignoring rotational effects. Curve (c) is the form for $f(qR_g)=D_{eff}/D$ shown in Fig. 5.2, which is for clusters with the same mass, and hence represents a delta function cluster mass distribution. Finally, curve (d) takes into account of both $N(M)$ and rotations, and has the most variation with $q\overline{R}$ of all the curves shown.

The shape of the master curve provides us with a great deal of information about the aggregation process. Its shape depends critically on the cluster mass distribution. It is also sensitive to the contribution of rotational diffusion, and thus reflects the anisotropy of the clusters. Since the behavior of the master curve results explicitly from the change in the structure factor of the clusters, its shape will directly reflect the shape of the structure factor and in particular, the crossover region where $qR_g \approx 1$. The scaling factor required to shift the data onto the master curve provides a measure of the characteristic size of the clusters, and its time dependence will directly reflect the aggregation kinetics.

Experimentally, we take data at different t_a, to follow the aggregation. Figure 5.9 shows the measured diffusion coefficient as a function of q, measured at 7 different times. The colloidal gold used as a model system enables us to stop the aggregation, and hence each of the 7 sets of data was taken with samples stopped at a prescribed time, t_a. This method enables us to take data at very early stages of the aggregation. Data sets 1 and 2 were taken at t_a=7 sec and t_a=10 sec, which is not otherwise possible but which is essential to follow up the rapid aggregation.

To scale the measured data onto a master curve requires a knowledge of $\overline{R}$ to scale each data set. However, to measure $\overline{R}$ directly would require data obtained at

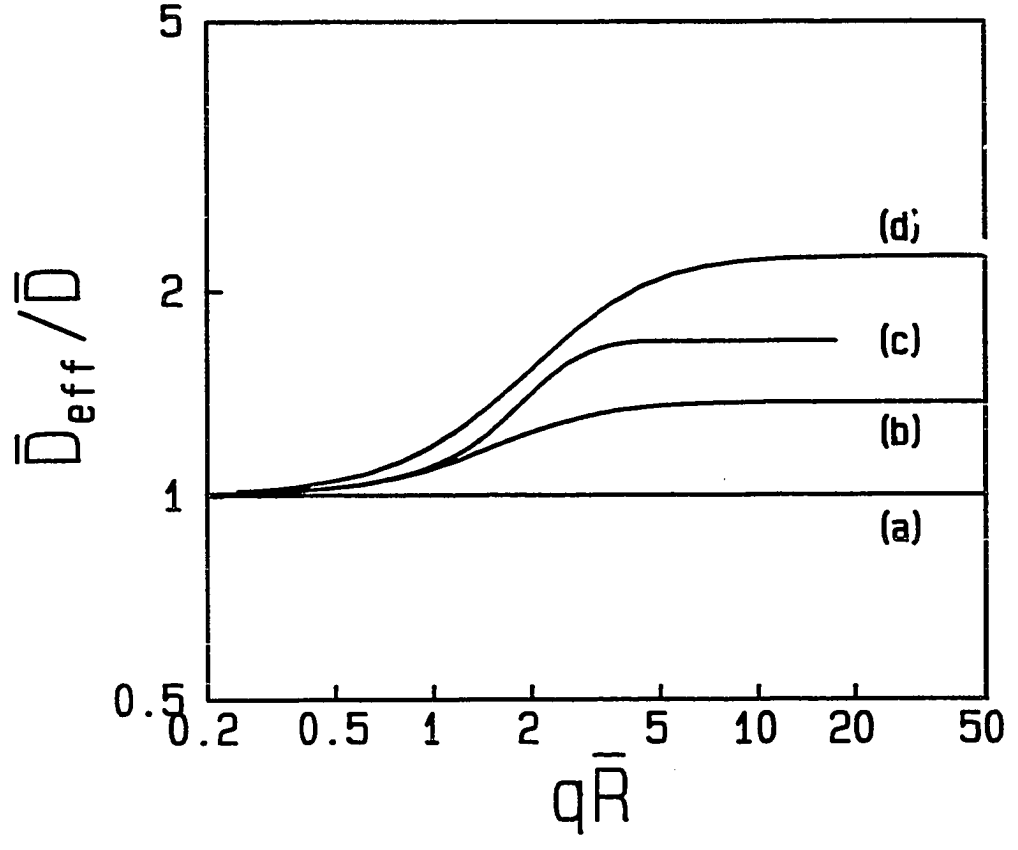

Fig. 5.8 Master curves calculated for different conditions. (a) $\overline{D}_{eff}=\overline{D}$, with no polydispersity; (b) cluster mass distribution of DLCA, excluding the effects of rotational diffusion; (c) including the effects of rotational diffusion, but with a monodisperse cluster mass distribution, and (d) including the effects of both the cluster mass distribution and rotational diffusion.

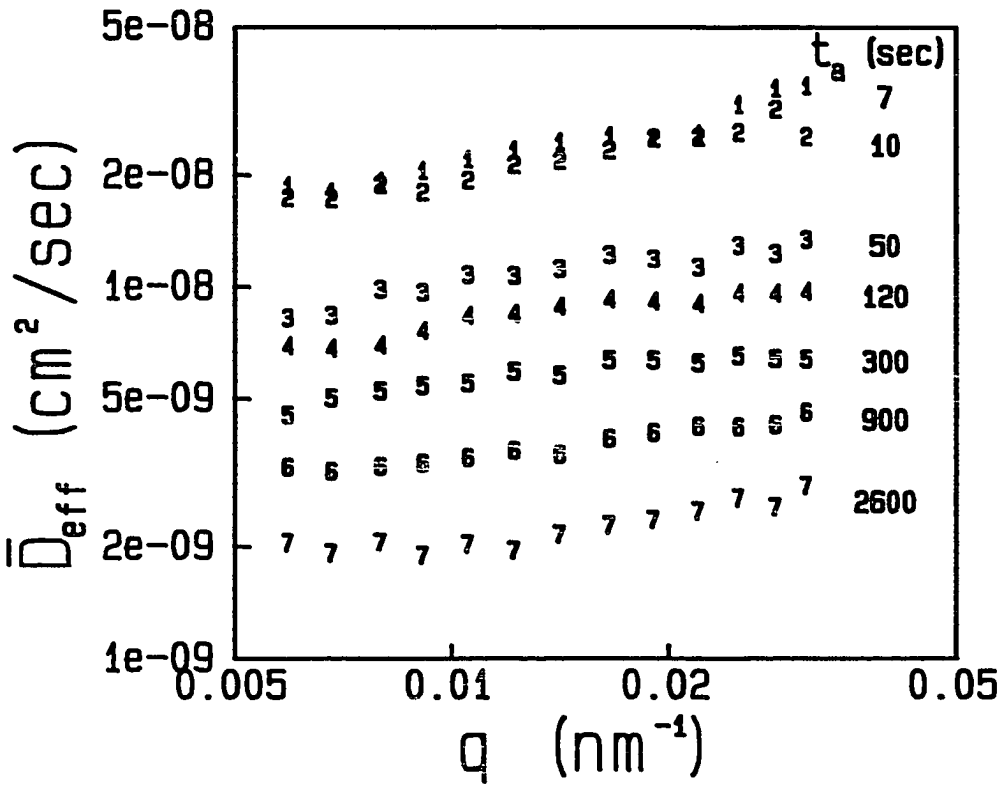

Fig. 5.9 Measured data of D_{eff} as a function of q, taken at different times t_a as labeled, for colloidal gold.

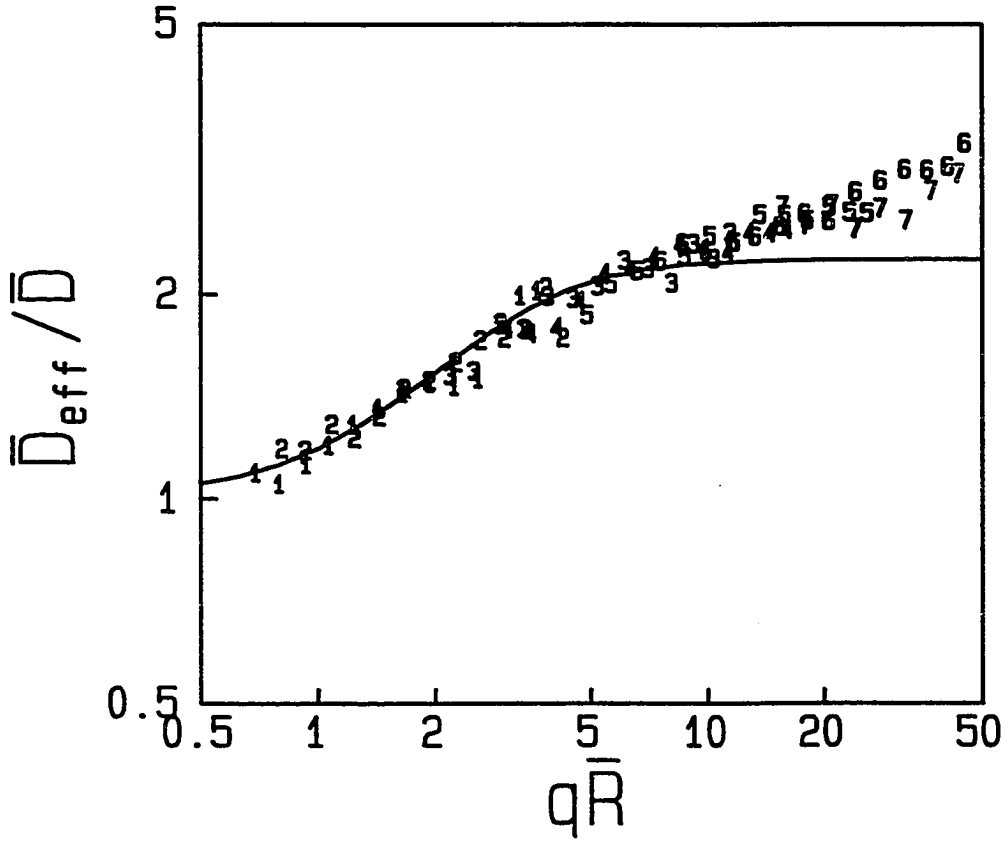

Fig. 5.10 Data from Fig. 5.9 scaled onto a master curve, by multiplying each set by a factor of $\bar{R}/\zeta$, and plotting as a function of $q\bar{R}$. An $\bar{R}(t_a)$ is chosen for each data set such that it overlaps with the others. The solid curves is the calculated result shown in Fig. 5.8(d).

the $q \to 0$ limit, which is not possible for most of the data sets. Hence, the scaling factor is obtained empirically by choosing an $\overline{R}$ for each data set so that it overlaps with the other data sets. With sufficient data sets, this scaling process is both straightforward and unambiguous. As can be seen by the results shown in Fig. 5.10, the data can be scaled to lie on a single master curve. The solid curve plotted with the data is the calculation shown in Fig. 5.8(d). It goes through the data over most of the range of $q\overline{R}$, until $q\overline{R} >> 1$. Internal vibration modes could be responsible for the deviation at large $q\overline{R}$, which we do not take into account in the theoretical calculation.

The scaling factor $\overline{R}$ obtained is a function of t_a. This provides an additional measure of the aggregation kinetics. We have plotted the values of $\overline{R}$ obtained in the scaling in Fig. 5.6, by the solid triangles connected with dashed lines, with the data of $\overline{R}(t_a)$ obtained by the calibration function. As can be seen, the data set obtained in this way behaves much better, since it results from the master curve, thus is an average over many angles.

5.7 UNIVERSAL BEHAVIOR OF COLLOID AGGREGATION

The power of the master scaling curve is not only that it provides an effective way to study the features of colloid aggregation, but also that it can serve as a sensitive means of comparing the aggregation behavior of completely different colloids. This can be done directly because all features specific to the individual colloid, such as the single particle radius, a, have been scaled out of the master curve. Thus we can use dynamic light scattering as a critical test of the universal behavior of colloid aggregation in each of the two limiting regimes. In addition, static light scattering provides an extra method to measure the fractal dimension and the structure factor.

To test the universality of DLCA, we choose three very different colloids:

gold, silica and polystyrene latex. Each is comprised of a different material, each is stabilized by different functional groups, for each colloid the aggregation is initiated by a different method, each colloid forms completely different interparticle bond upon aggregation. However each of them can be disstabilized to $E_b << k_B T$, allowing DLCA regime to be investigated.

The colloidal gold is prepared following a modified recipe due to Turkevich[28,29] by reducing gold from a sodium tetrachloroaurate solution. The colloid has an initial particle radius of a=7.5 nm, and a volume fraction of $\phi_0 = 2.8 \times 10^{-6}$. It is initially stabilized by surface adsorbed citrate ions. Aggregation is initiated by adding pyridine, which adsorbs on the surface of the particles, displacing the citrate ions and reducing the stabilizing surface charges. The amount of pyridine added determines whether the aggregation is diffusion or reaction–limited. For DLCA, the final concentration of pyridine was 10^{-2} M. The interparticle bonds of aggregates are most likely metallic.

The colloidal silica used is Ludox–TM commercially available from DuPont. It consists of particles with a=11 nm and was diluted to $\phi_0 = 1.7 \times 10^{-6}$ for the experiments. The colloid is initially stabilized by SiO^- groups on the surface of the particles. The pH was adjusted to $\geq$11 by addition of NaOH and aggregation was then initiated by addition of NaCl, which decreases the Debye–Hückel screening length, reducing the repulsive barrier between the particles. The final salt concentration was 1.7 M. The interparticle bonds of the aggregates are believed to be siloxane bonds.

The polystyrene latex has a=19 nm and was diluted to $\phi_0 = 0.8 \times 10^{-6}$. The polystyrene is stabilized by charged carboxylic acid groups on their surface. Aggregation was initiated by adding HCl to a concentration of 1.2 M which both neutralizes the surface charges and decreases the Debye–Hückel screening length. The interparticle bond of the aggregates are due to Van der Waals interactions and

steric entanglements.

To achieve diffusion–limited aggregation kinetics means that the barrier height between the colloidal particles must be E_b=0. Therefore, precautions are taken in preparing each colloid. Distilled, deionized and filtered water is used in every step in diluting the solutions. Only the water was filtered, not the colloids, since going through the filter induces some aggregation and changes the particle surface chemistry and concentration. For colloidal gold, aged water seems to cause difficulties in completely displacing the surface ions, resulting in aggregation kinetics that are in the crossover regime rather than the DLCA regime. For colloidal silica, it is crucial to have enough OH^- ions in the solution to catalyze an irreversible, permanent bond when the particles stick.

Except for gold, where data were taken by first stopping the aggregation, all the data for the other two colloids were taken repeatedly as a function of q by changing the angle of the detector while the aggregation was in progress. We then logarithmically interpolated the data to extract data sets representing the q dependence of Γ_1 at several fixed aggregation times, t_a. Master curves were obtained following the procedures described in the previous section. The kinetics were determined from the time dependence of the scaling parameter $\bar{R}$. In addition, the static light scattering intensity was measured concurrently, allowing the fractal dimension to be determined independently.

The normalization removes all features specific to the individual colloids from the scaling curves. Thus there are no remaining adjustable parameters and they can be compared directly. In Fig. 5.11, we plot the three master curves obtained from the different colloids. As can be seen, they are indistinguishable. Furthermore, the theoretically calculated curve is in good agreement with the data. The static scattering from each colloid was also identical, as shown in Fig. 5.12. The measured fractal dimension was $d_f \approx 1.86 \pm .01$ in each case as shown in Table 5.1.

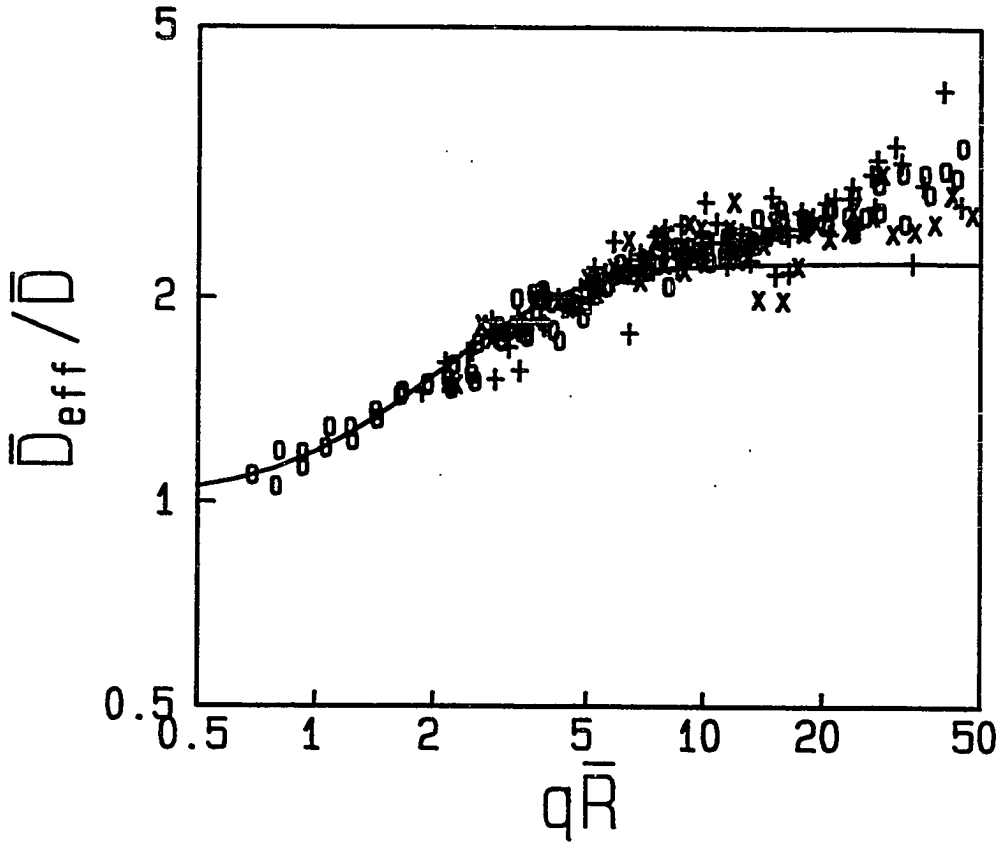

Fig. 5.11 Master curves for gold (o), silica (+), and polystyrene (×) for DLCA. The solid curve is the calculated result shown in Fig. 5.8(d).

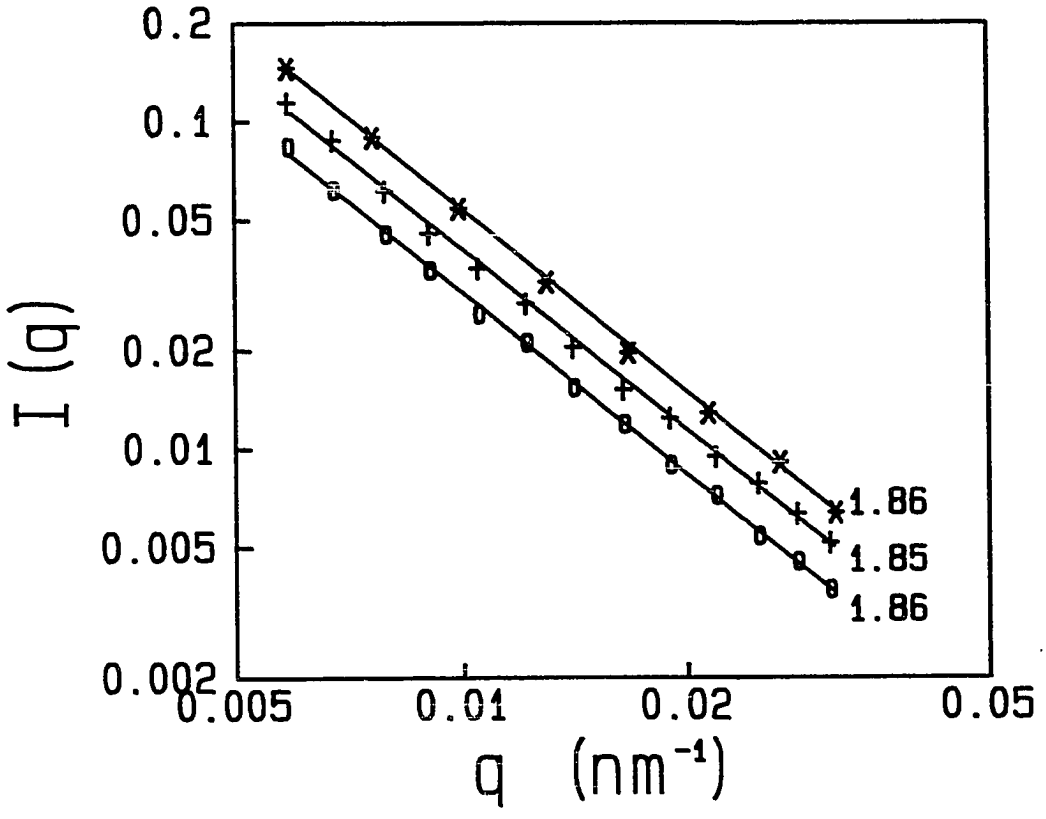

Fig. 5.12 Static light scattering from DLCA aggregates of gold (o), silica (+) and polystyrene (*). The measured fractal dimensions are: gold, d_f=1.86; silica, d_f=1.85; and polystyrene, d_f=1.86.

The growth kinetics of each colloid had the same behavior, as shown in Fig. 5.13. The values of $\overline{R}$ obtained from the scaling are plotted as a function of aggregation time t_a for all three colloids. They all exhibit linear behavior in the logarithmic plot. The slope of each curve gives the exponent z/d_f. With the fractal dimension obtained above, we calculate z for each colloid, and list in the same Table. The values of z thus obtained are within 6% for all three colloids, and also agree well with the theoretical prediction that z=1. Furthermore, the prefactor of each curve can be measured as the intercept from the plot, and compared with theory. From Eq. (5.4a), we have

$$\overline{R}_g \approx a\,(t_a/t_0)^{1/d_f}, \tag{5.19}$$

where t_0 is given by Eq. (5.4b). Using $\overline{R}=\beta\overline{R}_g$, we have

$$\overline{R} = a\beta\,(t_a/t_0)^{1/d_f}. \tag{5.20}$$

We calculate the prefactor $a\beta/t_0^{1/d_f}$ for each colloid and list them with the measured intercepts in Table 5.1. Again we see remarkable agreement between the calculated and measured values for each colloid, considering all the approximations and experimental uncertainties. All results shown in the Table indicate that these properties of the three colloids are almost identical, and are also in good agreement with the calculated values.

Table 5.1 Comparison of quantities for the different colloids

Colloids	d_f	z	Dynamic Prefactor (nm/min$^{0.54}$)	
			$a\beta/t_0^{0.54}$	Measured
Gold	1.86	0.98	301	359
Silica	1.85	1.00	179	166
Polystyrene	1.86	1.05	85	115

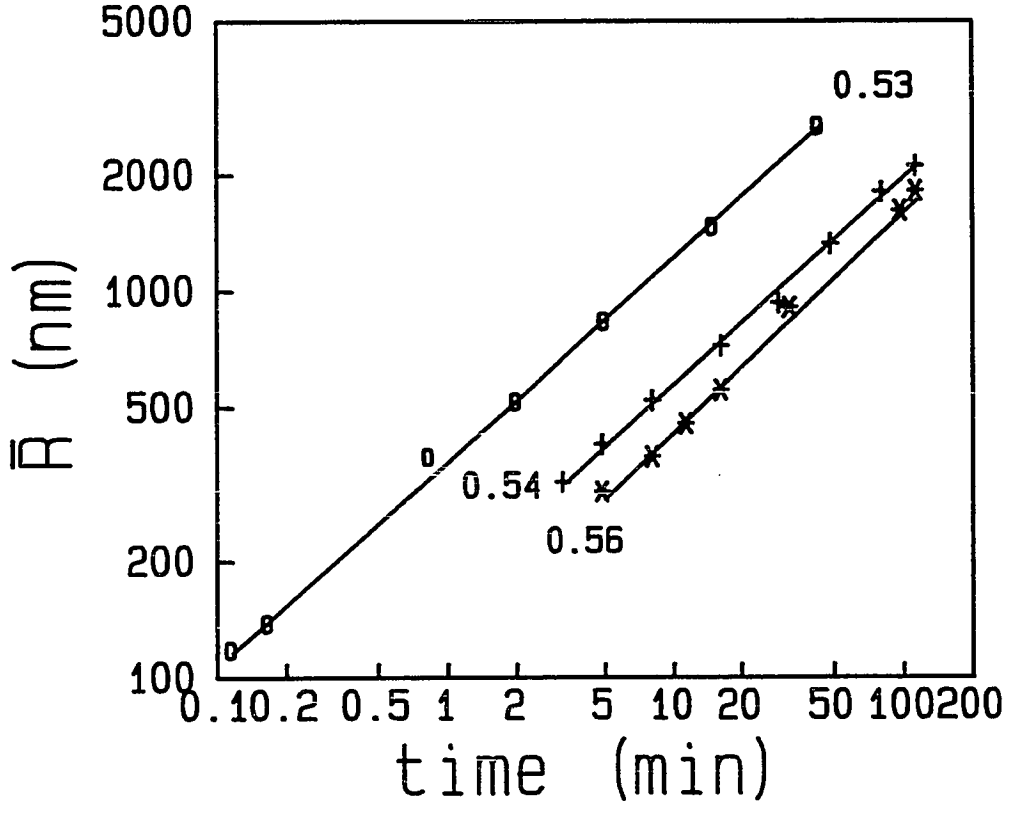

Fig. 5.13 Kinetics of DLCA aggregation for gold (o), silica (+) and polystyrene (*), plotted in a logarithmic scale. The slopes for the straight lines are for gold (0.53), silica (0.54), and polystyrene (0.56).

5.8 CONCLUSIONS

In this chapter, the process of colloid aggregation in the diffusion–limited regime is studied using both static and dynamic light scattering. We show that both scattering techniques are excellent probes of the aggregation process. All the important features of the aggregation process can be probed: the fractal dimension; the structure factor of the clusters; the cluster anisotropy as reflected in rotational diffusion; the cluster mass distribution, and aggregation kinetics. We present a detailed description of static and dynamic light scattering from colloidal aggregates, which accounts for the experimental results very well. Static light scattering, with $q\bar{R}>1$, is used to measure the fractal dimension; when $qR\approx1$ it is used to measure the cross–over behavior of the structure factor of the aggregates. Dynamic light scattering is sensitive to the shape of the cluster mass distribution and the effects of rotational diffusion of the aggregates when $q\bar{R}>1$. A correct measure of the size of the characteristic cluster by dynamic light scattering can be obtained when the effects of rotational diffusion are properly included. We have also measured the ratio of the hydrodynamic radius to the radius of gyration of individual clusters as $\beta=0.93$ for aggregates formed by DLCA.

A method is developed to scale the results of dynamic light scattering onto a single master curve. The sensitivity of dynamic light scattering to all the key features of the aggregation process is reflected in the shape of this master curve. Since the master curves are independent of the specifics of the colloidal system, they can be used to critically test the universality of colloid aggregation. This universality is demonstrated by presenting identical master curves from three completely different colloids. In addition, static light scattering measurements of the fractal dimension and dynamic light scattering measurements of the aggregation kinetics are also all the same for the colloids. The fact that the master curves have identical shape for each colloid implies that each of the key features is identical, and

is independent of the specific details of the individual colloids. This therefore lends very strong support to the concept of the universality of the DLCA regime of colloid aggregation.

APPENDIX

Here we prove that the ratio of the average effective diffusion coefficient and its value at q=0, $\overline{D}_{\rm eff}/\overline{D}$, is a function of $q\overline{R}$ only.

We name $F(q,\overline{R})=\overline{D}_{\rm eff}/\overline{D}$, where $\overline{R}=\zeta/\overline{D}$. Also $D_{\rm eff}/D=f(qR_{\rm g})$, which is function of $qR_{\rm g}$ only, as shown in Eq. (5.13). Since $\overline{D}_{\rm eff}=\Gamma_1/q^2$, according to Eq. (5.17),

$$F(q,\overline{R}) = \frac{\Sigma_M\ N(M)M^2S(qR_{\rm g})D_{\rm eff}/\overline{D}}{\Sigma_M\ N(M)M^2S(qR_{\rm g})} \tag{5.A1}$$

Defining $R_{\rm g}/\overline{R}=r$, $M/\overline{M}'=m$, where $\overline{M}'=(\overline{R}/a)^{d_{\rm f}}$ is a moment of the cluster mass distribution, and consequently, $m=r^{d_{\rm f}}$. We also name $q\overline{R}=x$. Recall from Eq. (5.1) that we have

$$N(M)M^2 = \psi(m)m^2 \tag{5.A2}$$

We now convert the summation $\Sigma_M N(M)$ to an integral, $\int N(M)dM$, and rewrite Eq. (5.A1) as

$$F(q,\overline{R}) = \frac{\int dm\psi(m)m^2S(xr)f(xr)/(\beta r)}{\int dm\psi(m)m^2S(xr)} \tag{5.A3}$$

$$= \frac{\int dr r^{3d_{\rm f}-2}\psi(r^{d_{\rm f}})S(xr)f(xr)}{\beta\int dr r^{3d_{\rm f}-1}\psi(r^{d_{\rm f}})S(xr)} \tag{5.A4}$$

It is clear from Eq. (5.A4) that $F(q,\overline{R})=F(x)$, that is, it is a function of $q\overline{R}$ only. Hence, the quantity $\overline{D}_{\rm eff}/\overline{D}$ scales with $q\overline{R}$, which assures the existence of the master scaling curve.

REFERENCES

[1]D. A. Weitz and J. S. Huang, in *Kinetics of Aggregation and Gelation*, ed. F. Family and D. P. Landau (North–Holland, Amsterdam, 1984).

[2]D. A. Weitz, J. S. Huang, M. Y. Lin and J. Sung, *Phys. Rev. Lett.* **54**, 1416 (1985).

[3]E. J. W. Verway and J. T. G. Overbeek, *Theory of the Stability of Lyophobic Colloids* (Elsevier, Amsterdam, 1948).

[4]P. Meakin, in *Phase Transitions* **12**, ed. J. L. Liebowitz (Academic Press, New York, 1988).

[5]D. A. Weitz, M. Y. Lin and J. S. Huang, in *Physics of Complex and Supermolecular Fluids*, ed. S. A. Safran and N. A. Clark (Wiley–Interscience, New York, 1987).

[6]P. Meakin, *Phys. Rev. Lett.* **51**, 1119 (1983).

[7]M. Kolb, R. Botet and R. Jullien, *Phys. Rev. Lett.* **51**, 1123 (1983).

[8]D. A. Weitz and M. Oliveria, *Phys. Rev. Lett.* **52**, 1433 (1984).

[9]C. Aubert and D. S. Cannell, *Phys. Rev. Lett.* **56**, 738 (1986).

[10]M. Matsushita, Y. Hayakawa, K. Sumida and Y. Sawada, in *Proceeding of the First International Conference for Science on Form*, ed. Y. Kato and J. Toriwaki (KTK Scientific Publishers, Tokyo, 1986).

[11]P. Dimon, S. K. Sinha, D. A. Weitz, C. R. Safinya, G. S. Smith, W. A. Varady and H. M. Lindsay, *Phys. Rev. Lett.* **57**, 595 (1986).

[12]T. Vicsek and F. Family, *Phys. Rev. Lett.* **52**, 1669 (1984).

[13]R. J. Cohen and G. B. Benedek, *J. Chem. Phys.* **86**, 3696 (1982).

[14]P. Meakin, T. Vicsek and F. Family, *Phys. Rev.* **B31**, 564 (1985).

[15]D. A. Weitz and M. Y. Lin, *Phys. Rev. Lett.* **57**, 2037 (1986).

[16]E. Pefferkorn, C. Pichot and R. Varoqui, *J. Phys.* (France), **49**, 983 (1988).

[17]P. G. J. Van Dongen and M. H. Ernst, *Phys. Rev. Lett.* **54**, 1396 (1985).

[18]B. J. Berne and R. Pecora, *Dynamic Light Scattering* (Wiley–Interscience, New York, 1976).

[19]Chapter 4, this volume.

[20]G. Dietler, C. Aubert, D. S. Cannell and P. Wiltzius, *Phys. Rev. Lett.* **57**, 3117 (1986).

[21]R. G. Mountain and G. W. Mulholland, preprint.

[22]H. M. Lindsay, R. Klein, D. A. Weitz, M. Y. Lin and P. Meakin, *Phys. Rev.* **A38**, 2614 (1988).

[23]H. M. Lindsay, R. Klein, D. A. Weitz, M. Y. Lin and P. Meakin, to appear in *Phys. Rev.* A (1989).

[24]E. Jakeman, in *Photon Correlation and Light Beating Spectroscopy*, ed. H. Z. Cummins and E. R. Pike (Plenum, New York, 1974).

[25]W. Hess, H. L. Frisch and R. Klein, *Z. Phys.* **B64**, 65 (1986). In Eq. (14) of this paper, the 4 should be replaced by 2.

[26]Z.–Y. Chen, P. Meakin and J. M. Deutch, *Phys. Rev. Lett.* **59**, 2121 (1987); P. Meakin, Z.–Y. Chen and J. M. Deutch, *J. Chem. Phys.* **82**, 3786 (1984).

[27]D. A. Weitz, J. S. Huang, M. Y. Lin and J. Sung, *Phys. Rev. Lett.* **53**, 1657 (1984).

[28]J. Turkevich, P.C. Stevenson and J. Hillier, *Trans. Faraday Soc. Disc.* **11**, 55 (1951).

[29]Chapter 2, this volume.

CHAPTER 6

REACTION–LIMITED COLLOID AGGREGATION AND ITS UNIVERSALITY STUDIED BY LIGHT SCATTERING

ABSTRACT

The process of colloid aggregation in the reaction limited regime (RLCA) is studied using light scattering. A detailed description is given on how the scattering results are related with the behavior of the aggregates. Using static light scattering, the structure factor of the aggregates is found to agree with a form determined from computer–simulated aggregates. The power–law cluster mass distribution resulting from RLCA causes dynamic light scattering to be sensitive to the behavior of clusters of all sizes. The dynamic light scattering data is scaled onto a single master curve, whose shape depends critically on the structure of the aggregates and the cluster mass distribution. By including the effects of rotational diffusion of the aggregates and their mass distribution with the distribution exponent τ=1.5, excellent agreement is found between our prediction of the shape of the master curve and that obtained from experiments. Furthermore, the master curves from several completely different colloids are identical. In addition, the fractal dimension measured by the static light scattering and the aggregation kinetics are also the same for these colloids. This provides strong evidence of the universality of colloid aggregation, and RLCA as a universal regime.

6.1 INTRODUCTION

Significant advances in our understanding of kinetic colloid aggregation have been made in the past several years. This is because the structure of the aggregates has been recognized as having scale invariant symmetry, so that it can be characterized as a fractal. This quantitative description of the random and disordered structure of colloidal aggregates has in turn allowed a more detailed study of colloid aggregation by a variety of techniques, among which light scattering has been quite prominent.

In a kinetic aggregation process, where small particles stick together irreversibly to form larger clusters, the cluster structure produced is intrinsically related to the cluster mass distribution. In turn, both the cluster distribution and the cluster structure are ultimately controlled by the aggregation kinetics. Two limiting regimes of kinetics, diffusion–limited (DLCA) and reaction–limited (RLCA) cluster aggregation have been identified as universal regimes. Each regime has been widely studied both theoretically and experimentally. Each regime exhibits characteristic yet distinct behavior in terms of the shape of the cluster mass distribution, the kinetics of growth, and the fractal dimension of the aggregates.

If DLCA and RLCA are universal classes of kinetic aggregation, a wide variety of colloids can be expected to exhibit similar behavior. Several different colloid systems have been investigated, but there has been no systematic verification of the universal behavior of colloidal aggregation. To critically verify the universality of either one of the two regimes, all the important features that characterize the aggregation process need to be examined.

Here, we show that light scattering techniques, including both static and dynamic, are particularly powerful in studying and quantitatively describing colloid aggregation. The scattering results are sensitive to many of the features of an aggregation process: the cluster structure, including both the radially averaged

properties characterized by the fractal dimension and the cluster anisotropy, the cluster mass distribution and its time evolution as the aggregation proceeds. By properly including the effects of all these features, we are able to account for the experimental observations. We show that a master scaling curve can describe all the data measured in an aggregation process, and, can be used to characterize the aggregation and the aggregate structure, thus critically testing the universality of the colloid aggregation process. We verify this universality by comparing the light scattering data for three different colloid systems and showing that our theoretical calculations agree very well with our measurements.

Besides serving as a critical test for the universality of colloid aggregation, light scattering from colloidal aggregates is itself an important topic to study. In fact, it has been already widely used to study colloid aggregation, because of its convenience and the unique wavelength range of light compared with the sizes of the colloidal aggregates. Therefore, we also present a study of the self–consistency of both static and dynamic light scattering from colloidal aggregates. This is crucial in order to properly interpret the scattering results obtained, and serves as the corner stone in developing the method of testing the universality.

In this chapter, we will focus on the RLCA regime only, since the features characterizing the two regimes are distinct, different treatments are needed to discuss each regime. For RLCA, the highly polydisperse cluster mass distribution plays an important role in the scattering results and cautions must be exercised in the calculations of the expected results.

The rest of the chapter is organized as follows: we first discuss colloid aggregation in general and RLCA in particular, and briefly review prior work. In the next section, we describe our experimental setup and methods. We then present a study of both static and dynamic light scattering performed concurrently on the same sample and demonstrate the self consistency of our interpretation. In the two

following sections, we discuss how from calculation and from experiments a master curve can be obtained from the first cumulants of the autocorrelation functions. Finally we show that the experimental measurements for three completely different colloids are indeed identical and thus demonstrate the universality of the RLCA regime. A short conclusion then follows.

6.2 REACTION–LIMITED COLLOID AGGREGATION

A colloid is stable because the energy barrier between the colloidal particles prevents them from sticking to one another upon contact. Hence aggregation can occur only when the height of the barrier, E_b, is reduced. If E_b is reduced to much less than k_BT, very rapid aggregation results, limited only by the diffusion of the particles leading to their collisions. This regime is therefore the diffusion–limited regime. On the other hand, if E_b remains comparable to or larger than k_BT, slow coagulation results, and the aggregation rate is limited by the probability, $P \sim exp(-E_b/k_BT)$, of overcoming the barrier, or the reaction rate of the two particles. This is the reaction–limited regime. In each case, as particles stick together to become clusters, the clusters themselves continue to diffuse and aggregate. Thus the two regimes are more fully referred to as diffusion–limited cluster aggregation (DLCA) and reaction–limited cluster aggregation (RLCA).

In the reaction–limited regime, the aggregation rate is very slow since $P<<1$, so that numerous contacts are required before two approaching clusters stick. It is therefore traditionally called slow aggregation in the colloidal science literature. As the aggregation progresses, clusters with different masses are formed as first particles and then clusters stick with each other. The sticking probability of a cluster is proportional to P and the number of available bonding sites, thus clusters with larger mass grow faster than the smaller ones. These growth kinetics of the reaction–limited regime always leave a large number of small clusters behind,

therefore resulting in a highly polydisperse cluster mass distribution. By the same token, while initially the aggregation rate is very slow because all the clusters are small, the rate increases as the characteristic size of the clusters grows. This results in an exponential growth of the cluster size with time. The growth kinetics as well as the cluster mass distribution will in turn influence the structure of the clusters formed. Since the sticking probability is very low, two approaching clusters can sample all possible mutual configurations before they finally stick together so that smaller clusters can interpenetrate inside the large ones. In addition, because of the high polydispersity of the cluster distribution, many collisions will involve clusters of very different masses. These effects will lead to an increase in the fractal dimension of the clusters.

In order to fully describe the kinetic aggregation process of RLCA, it is necessary to study these characteristic features: the cluster mass distribution, the aggregation kinetics, and the time evolution of the cluster mass distribution, and the cluster structure, which can be described by the fractal dimension. These features can be studied with analytical approaches, computer simulations, and by experiments.

The most frequently studied quantity is the fractal dimension of the clusters. Aggregates formed in this regime from colloidal silica,[1] colloidal gold,[2] polystyrene latex[3] and synthetic melanin[4] have all been studied experimentally, and their fractal dimension measured using various methods, including static light scattering and transmission electron microscopy (TEM). Values of d_f varying between 2.05 and 2.20 have been found for these systems with a typical value being about 2.1. In addition, computer simulations modeling reaction–limited conditions also generate clusters with $d_f \approx 2.1$.[5]

Analytical approaches to RLCA regime are focused on the Smoluchowski rate equations.[6] These rate equations describe the time evolution of the cluster mass

distribution, in terms of their kernel, or the reaction probability of two clusters. It is found that for homogeneous kernels the rate equations yield solution obeying dynamic scaling.[6] Thus the solution can be expressed as

$$N(M,t_a) = M_n^{-2}\psi(M/M_n) \tag{6.1}$$

where $N(M,t_a)$ is the number of clusters of mass M at time t_a, and

$$M_n(t_a) = \frac{\Sigma N(M)\, M^n}{\Sigma N(M)\, M^{n-1}} \tag{6.2}$$

is the nth moment of the distribution. It reflects the time dependence of the cluster mass distribution, while the scaling function, $\psi(x)$, is time independent. In addition, for many kernels, the cluster distribution takes a form

$$N(M) \sim M^{-\tau} e^{-M/M_c}. \tag{6.3}$$

For the RLCA model, based on geometric arguments, Ball et al[7] found that τ=1.5 and the cutoff mass grows exponentially, $M_c \sim e^{t_a/t_0}$, where t_0 is a sample dependent time constant.

A computer simulation study of the RLCA model also results in a power law distribution of the cluster mass, with $\tau \approx 1.5$.[5] Another simulation study,[8] however, suggests that the exponent increases to a value closer to 2 for large t_a.

Experimentally, several colloidal systems have been studied to determine the shape of the cluster mass distribution. Several years ago, Von Schultess et al studied the cluster mass distribution of polystyrene colloids where the aggregation was induced by an antigen–antibody reaction.[9] They found that $N(M)$ was well described by Eq. (6.3), with $\tau \approx 1.5$. Unfortunately, their data extended over a relatively limited range of mass, up to about $M \approx 10$. More recently, a study using dynamic light scattering[10,11] suggested that colloidal silica aggregates produced by RLCA have a power law distribution with $\tau \approx 1.8 \sim 2.0$. This result was based on an interpretation of the light scattering data. Another study using TEM counting method with colloidal gold[12] showed that the cluster mass distribution has a power

law dependence with $\tau \approx 1.5$. It was also found that the measured distribution does obey dynamic scaling, so that data measured at different times can be scaled to collapse onto a single curve. While a wide range of cluster sizes was analyzed, and the result does not have the problem of interpretation that the light scattering does, it nevertheless suffers from limited statistical accuracy characteristic of these counting methods.

The aggregation kinetics of these experimental systems has been studied using dynamic light scattering to monitor the growth rate of the clusters. This average cluster radius was found to grow exponentially with time for colloidal gold,[2] colloidal silica[13] and synthetic melanin[4]. However, care must be exercised in the analysis of the light scattering as the measured average radius, $\overline{R}_{\text{eff}}$, is in general a function of the scattering wavevector, because of the polydispersity in $N(M)$ and of the contribution from rotations of clusters.

From the results listed above, we can see that the aggregation of a variety systems has been explored. They all exhibit similar behavior, consistent with the prediction of the RLCA model. However, discrepancies among certain properties, such as the distribution exponent, τ, still exist. There has not been a systematic study of the universal behavior of reaction–limited colloid aggregation. In the following sections, we present a study of light scattering from colloidal aggregates, and show that static and dynamic light scattering is very sensitive to all the important characteristic features of an aggregation process, that it can be used as a critical test of this universality. In addition, we determine the value of τ for all the experimental systems.

6.3 EXPERIMENT METHODS

We use both static light scattering and dynamic light scattering (or quasi–elastic light scattering)[15] as our experiment methods. Static light scattering

measures the time averaged scattering intensity from the sample, $I(q)$, as function of the scattering wavevector, $q = (4\pi n/\lambda)\sin(\theta/2)$, where λ is the incident wavelength, n is the index of refraction of water, and θ is the scattering angle. Dynamic scattering, by contrast, measures the temporal autocorrelation function of the scattering intensity,

$$G_2(t) = < I(t')\ I(t'+t) > \tag{6.4}$$

where t is the delay time and the brackets represent an average over t'.

With our experimental setup, we can measure both static and dynamic scattering concurrently as function of the scattering angle θ, and hence the scattering wavevector, q. An Argon ion laser with a wavelength λ=488 nm is used as the incident source. For the colloidal gold samples which absorb the incident light, the intensity is maintained at less than 1 mw before entering the sample cell to avoid heating effects. A correlator is used to measure both $I(q)$ and $G_2(t)$. The first cumulant, Γ_1, of the measured $G_2(t)$, is obtained by fitting the logarithm of the autocorrelation function to a third order polynomial after normalized by the baseline, B,

$$\frac{1}{2}\ln(G_2(t)/B-1) = \Gamma_0 - \Gamma_1 t + \frac{1}{2}\Gamma_2 t^2 - \frac{1}{6}\Gamma_3 t^3. \tag{6.5}$$

We make the measurements in situ while the aggregation is in progress. Data are taken as a function of both the scattering vector q, and the aggregation time t_a. Since the aggregation rate of RLCA is typically very slow, enough data can be taken while following up the aggregation process, with reasonable averaging. This method provides a convenient and simple way to make measurements for a complete kinetic process, and is suitable for the slow aggregation. In addition, if high quality data of the autocorrelation function over a wide range of t is desired, we stop the aggregation to make the measurements. This can be done for colloidal gold only, by adding a small amount of surfactant to the solution.

The aggregation usually takes more than several hours, thus precautions must be taken to avoid the differential sedimentation of the clusters due to gravity during the measurement. The drift velocity of a cluster due to gravity is $v=Mg/6\pi\eta R$, where R is the hydrodynamic radius, g is the gravitational acceleration and η is the water viscosity. Assuming fractal scaling, $M=m(R/a)^{d_f}$, where m is the mass of a single colloidal particle of radius a in grams, we have

$$v=\frac{2g}{9\eta}(\rho-\rho_0)a^2(\frac{R}{a})^{d_f-1} \tag{6.6}$$

where ρ is the bulk density of the colloidal particles, and ρ_0 is the density of water. Since the cluster mass distribution is very polydisperse, clusters with a large R may settle down a noticeable height while the smallest clusters are relatively stationary. For gold, which has ρ=19 and a=7.5 nm, a moderately large cluster with a radius of $R\approx$1 micron (the largest clusters can grow up to > 10 microns) will have a gravitational drift velocity of ~ 1.7 mm/hour. This will substantially change the cluster mass distribution at any height in a few hours. Even for silica, which has a much smaller density ($\rho\approx$2.5 and $a\approx$3.5 nm), a 1–micron cluster has a drift velocity of ~ 0.4 mm/hour, which is not negligible for a day–long experiment. In our experiments, an effective zero gravity is achieved, on average, by using a long narrow cuvette as a sample cell, filled completely and sealed at the top. The cell is then inverted every 15 minutes to eliminate the effects of gravitational drift.

Due to the fractal nature, the aggregates occupy an increasing volume fraction of the solution as they grow, even though the total mass is conserved. If this volume fraction approaches unity, they can gel. Complete gelation occurs when $\phi_0\approx(a/R_c)^{3-d_f}$ where R_c is the radius of the largest cluster at the time of gelation and ϕ_0 is the initial volume fraction. For $R_c\sim$10 microns and a=3.5 nm as for colloidal silica monomers, $\phi_0\approx 8\times10^{-4}$. Since the RLCA model proposed assumes low volume fraction, without gelation, we ensure that the initial volume fraction is

$\leq 10^{-5}$ to keep the system far away from gelation at later time.

In the following sections, when we describe how light scattering probes colloid aggregation, we use colloidal gold as the prototypic experimental system, since all those features of its aggregation are known independently.[2,12,14] We are able to stop its aggregation with surfactant, in order to take very good quality data for the autocorrelation function. In addition, gold particles are very good scatterers, which enables us to extend the measurement to very early stages of the aggregation, when the clusters are relatively small, at a volume fraction as low as 10^{-6}.

6.4 LIGHT SCATTERING FROM COLLOID AGGREGATES

In this section, we develop a detailed, self–consistent description of light scattering from colloidal aggregates. We calculate theoretically the quantities that can be experimentally measured, with the knowledge we have about the colloidal gold system and by making extensive use of the properties of clusters obtained from computer simulations. We compare our calculations with the measured data from light scattering experiments. We show that by properly including all the effects, our calculations are in agreement with the data of both static and dynamic scattering, measured concurrently from the same sample. To make sure that for a known system we can predict the experimental observations of light scattering, is crucial in order to use light scattering techniques to obtain information about and to test the behavior of the other systems. Furthermore, by comparing the data of static and dynamic scattering, we are able to determine the ratio of the hydrodynamic radius R to the radius of gyration R_g of the individual clusters.

We take very good quality data by first stopping the aggregation with surfactant. We ensure that the addition of surfactant only stops further aggregation of the colloids, without altering the aggregate structure. Both the static intensity $I(q)$, and the intensity autocorrelation function, $G_2(t)$, are taken concurrently as

functions of q, and averaged for a long period of time to allow sufficient statistical accuracy.

A. Static Light Scattering

The static scattering intensity $I_M(q)$ of a cluster of mass M is proportional to the Fourier transform of the pair correlation function of the cluster. Therefore, a measure of the q dependence of the scattering intensity reveals the structural properties of the clusters and consequently, can determine the fractal dimension. However, since the clusters are polydisperse, the measured scattering intensity $I(q)$ is an average of $I_M(q)$ over the cluster mass distribution. Hence two pieces of information are needed to calculate $I(q)$: the structure of the individual clusters reflected in $I_M(q)$, and the cluster mass distribution $N(M)$.

The scattering intensity of a single cluster can be written as

$$I_M(q) \propto M^2 S(qR_g) \tag{6.7}$$

where $S(qR_g)$ is the static structure factor and the radius of gyration is defined as $R_g = aM^{1/d_f}$. Since the fractal clusters are scale invariant, this structure factor is a function of qR_g only.[16] The limiting behavior of the structure factor is well known. For $qR_g << 1$, the clusters can be considered as point scatterers and $I_M(q)$ is proportional to M^2. For $qR_g >> 1$, the light is only sensitive to the fractal correlation inside the cluster, so $S(qR_g) \sim (qR_g)^{-d_f}$ and $I_M(q) \sim q^{-d_f}$, exhibiting the fractal scaling. In between, when $qR_g \approx 1$, is the crossover region, where the shape of the structure factor is determined by the cutoff function of the pair density correlation function. The experimentally measurable scattering intensity,

$$I(q) = \sum_M N(M) I_M(q) \propto \sum_M N(M) M^2 S(qR_g), \tag{6.8}$$

is a sum of $I_M(q)$ over $N(M)$. It can be shown that its limiting behavior is very similar to that of $I_M(q)$, except at the crossover region, since the sum over $N(M)$ plays a big role in determining $I(q)$.[16]

To obtain the experimental data that can be compared with the theory, we purposely stop the aggregation at a time t_a, when we can measure the crossover region. The data taken for $I(q)$ are shown in Fig. 6.1 by the squares. We can see that the crossover region extends over the entire q range, and only at very large q does the data appear to be linear on the logarithmic plot.

The data is interpreted in terms of Eq. (6.8) where both $S(qR_g)$ and $N(M)$ are needed for the calculation. The structure factor used has a functional form given by

$$S(x) = (1 + C_1x^2 + C_2x^4 + C_3x^6 + C_4x^8)^{-d_f/8} \tag{6.9}$$

where $x=qR_g$, $C_1=\frac{8}{3d_f}$, and C_2, C_3 and C_4 are obtained by fitting this expansion to the structure factor calculated for computer generated RLCA clusters. Eq. (6.9) has the correct asymptotic forms at both limits of x, and C_1 is determined so that $S(x\to 0)=1+x^2/3$, as it must be to follow the Guinier form. The high order terms are found to be necessary to produce the relatively sharp crossover of the structure factor. By contrast, if we try to use other forms for the structure factor, such as the modified Fisher–Burford form,[17] the fit to the data is markedly poorer.[16]

For the cluster mass distribution $N(M)$ the expression in Eq. (6.3) with $\tau=1.5$ is used. We relate the cutoff mass M_c to an average cluster mass defined as the second moment of the distribution,

$$M_2 = \frac{\Sigma\ N(M)M^2}{\Sigma\ N(M)M}. \tag{6.10}$$

Using $\tau=1.5$, $M_2\approx 0.51M_c$ is obtained. With $R_g=aM_2^{1/d_f}$ an average radius of gyration can be introduced. The fit of the data in Fig. 6.1 using Eq. (6.8) then determines the average mass as $M_2=1020\pm 20$ and the average radius of gyration as $R_g\approx 204$ nm, where $a=7.5$ nm for the colloidal gold.

The fitting parameter, M_2, or equivalently R_g, which characterizes the cluster mass distribution will be used in fitting the results of the dynamic scattering,

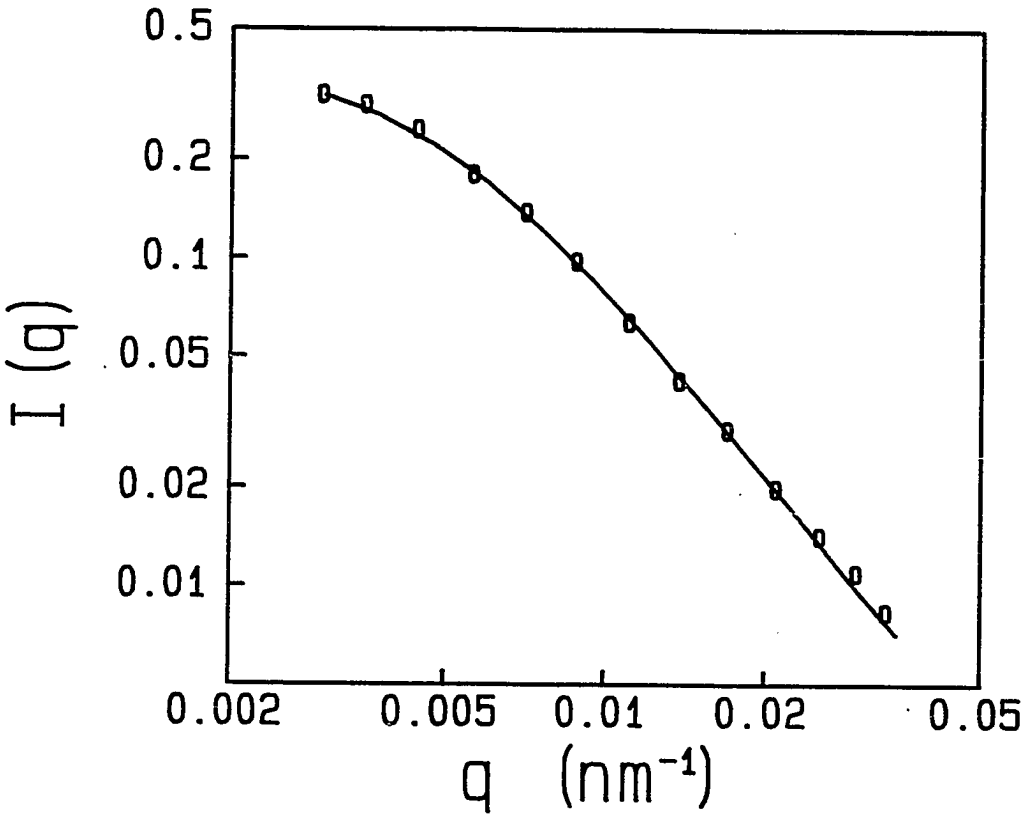

Fig. 6.1 Static light scattering intensity from colloidal gold aggregates formed by RLCA. The data were taken when the sizes of the aggregates were not large enough for the intensity to exhibit a linear fractal scaling in the logarithmic plot. The solid curve is a calculation using Eqs. (6.3), (6.8) and (6.9). An average radius of gyration $\overline{R}\approx 204$ nm is obtained from the fit.

where the same form for $N(M)$ and $S(qR_g)$ appear. This provides a consistent comparison of the calculations with the measured data from the same sample.

B. Dynamic Light Scattering

Dynamic light scattering measures the fluctuation of the scattered light, and therefore probes the dynamics of the aggregates. In homodyne experiments, the measured quantity is the intensity autocorrelation function, $G_2(t)$ (Eq. (6.4)). It can be related to the field autocorrelation function $G_1(t)$ by the Siegert relation[18,19]

$$G_2(t) = A' G_1(t)^2 + B \tag{6.11}$$

where $A'<1$ depends on experimental conditions and B is the baseline.

One treatment of the autocorrelation function $G_1(t)$ including the effects of both translational and rotational diffusion is to decompose the structure factor $S(qR_g)$ into spherical harmonics, since the rotational effect depends on the anisotropy of the cluster structure. The results obtained by this technique are in excellent accord with experimental measurements.[19] However, this method is computationally intensive, in particular for values of $qR_g>12$ and for clusters larger than $M\approx1000$. Here we use an alternative approach which explicitly takes advantage of the scaling properties of the clusters.

We write the autocorrelation function as

$$G_1(t) = \sum_M N(M)M^2 S(qR_g) e^{-q^2 D_{eff} t} \tag{6.12}$$

where $D_{eff}=Df(qR_g)$ is the effective diffusion coefficient of a single cluster, $D=\zeta/R$ is its translational diffusion coefficient with $R=\beta R_g$ the hydrodynamic radius and $\zeta=k_B T/6\pi\eta$. The effects of rotational diffusion are included in $f(qR_g)$,[19,20] which is a function of the scaled scattering vector, qR_g, reflecting the scaling behavior of the fractal aggregates.

In Eq. (6.12) we include the effects of rotations in shifting D to a q dependent D_{eff} in the first cumulant of the individual clusters, while neglecting their effects on

the higher cumulants. Thus, Eq. (6.12) is exact up to the order of the first cumulant. The aggregates formed by RLCA are highly polydisperse, thus we expect that the shape of the autocorrelation function is dominated by the cluster mass distribution, $N(M)$. Indeed, a calculation of the second cumulant Γ_2,[21] which characterizes the width of the decay rates, shows that it is mainly due to the broadening of the cluster mass distribution.

We obtain $f(qR_g)$ using computer simulated clusters produced under reaction–limited conditions. We calculate $f(qR_g)$ for 175 clusters of masses from 50 to 1460 particles, and take the average. We then use Eq. (6.12) to calculate the autocorrelation function, in which we again use Eqs. (6.3) and (6.9) with $\overline{R}_g$=204 nm as obtained before. In Fig. 6.2, we fit the autocorrelation function taken for the same sample at θ=15^o, corresponding to q=0.00447 nm^{-1}. The agreement between the fit and the data is excellent. The only fitting parameter here is β, which is the ratio of the hydrodynamic radius R, used in D, to the radius of gyration R_g, $\beta=R/R_g$. For the best fit shown we obtain β=1.0. Since $q\overline{R}_g\approx0.9<1$, $f(qR_g)\approx1$, and rotational diffusion plays only a minor role as can be seen from the dashed curve shown, which is a calculation using $D_{eff}=D$. This value is also in remarkably good agreement with the value of β=0.97 by computer simulations[22] and that obtained with colloidal silica, after the effect of polydispersity is taken into account.[23,24]

At wider angles, rotational diffusion plays a significant role in the decay of the autocorrelation function as $f(qR_g)>1$. We fix β=1.0 and again use $\overline{R}_g$ as the parameter in fitting $G_2(t)$ taken at these angles. We see very good agreement between the theory and the data, and the deviation in $\overline{R}_g$ for 11 angles from 19^o to 150^o is less than 5%. We show an example for θ=96^o (q=0.0255 nm^{-1}) in Fig. 6.3. As can be seen the agreement is excellent, and we obtain $\overline{R}_g$=205 nm. Since at this angle $q\overline{R}_g\approx5.3$, rotational effects are important. The dashed curve in Fig. 6.3 is the calculation without including rotations, which deviates considerably from the data.

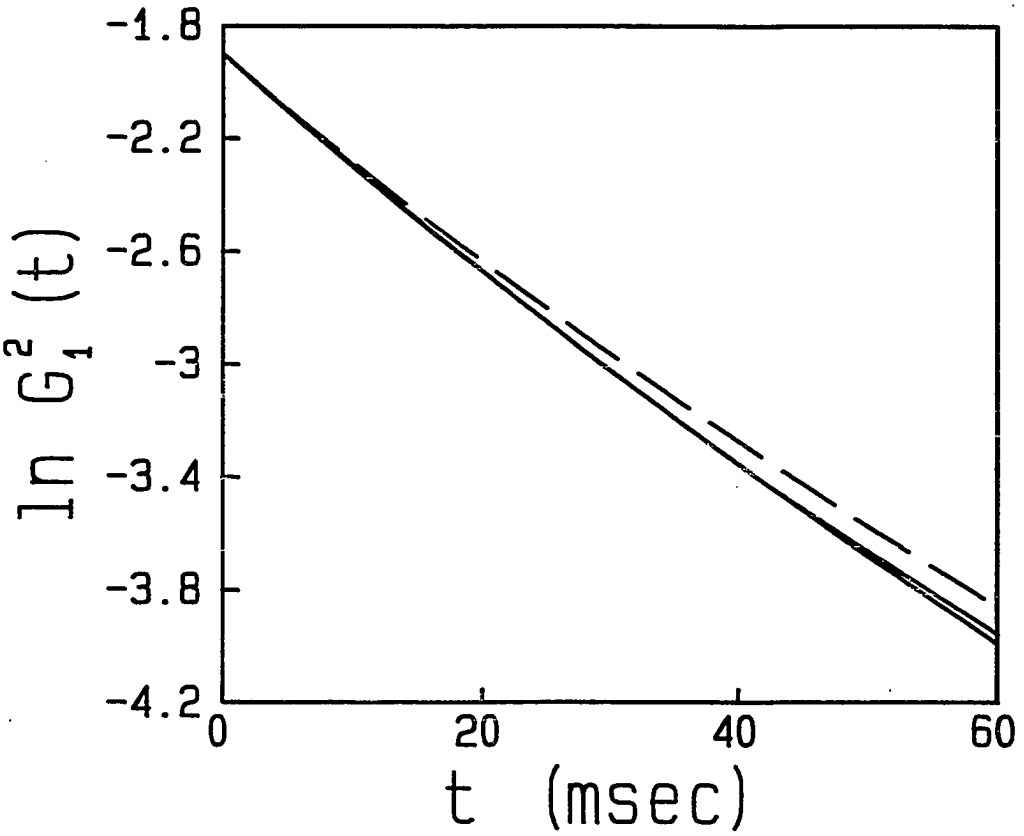

Fig. 6.2 The autocorrelation function measured at θ=15^{o} for gold RLCA aggregates. The solid curve through the data is a fit using Eq. (6.12) and D_{eff}, which includes the effects of rotational diffusion. The fit and the data cannot be distinguished. The dashed curve is the same calculation, but excluding the effects of rotational diffusion.

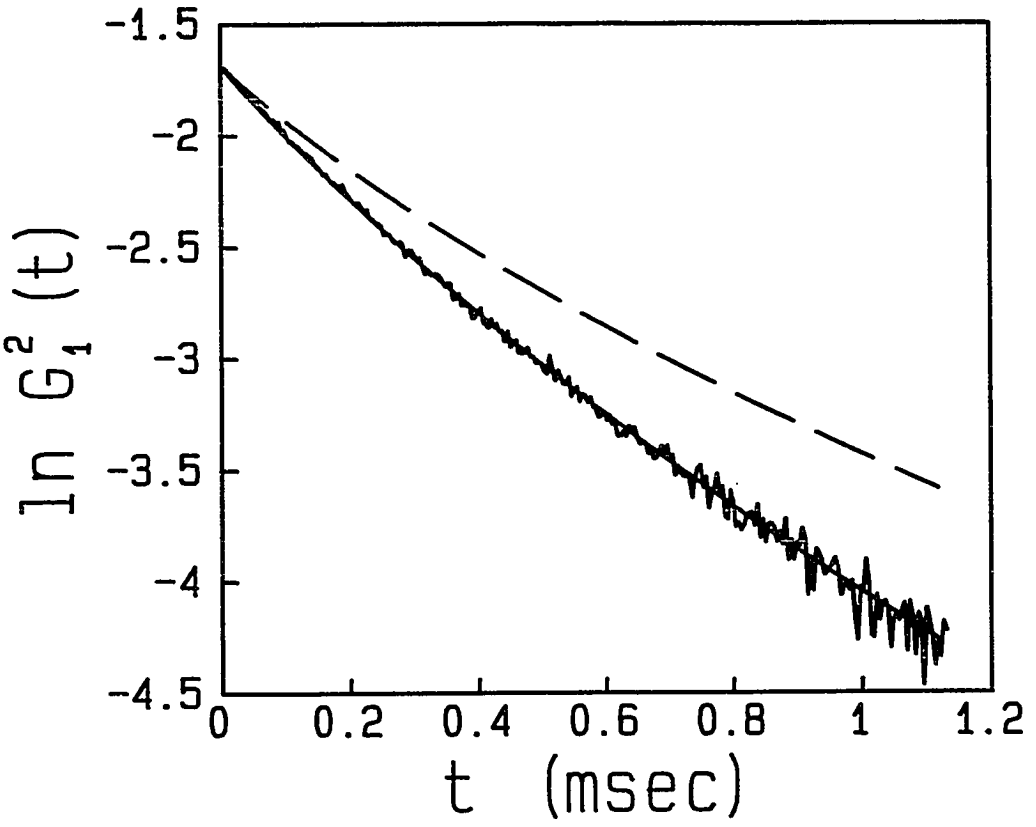

Fig. 6.3 The autocorrelation function measured at θ=96^{o} for gold RLCA aggregates. The solid curve through the data is a fit using Eq. (6.12) and D_{eff}, which includes the effects of rotational diffusion. The dashed curve is the same calculation, but excluding the effects of rotational diffusion, which are significant in this case.

In this section, we study light scattering from colloidal aggregates by calculating the experimental measurable quantities and comparing these with the data. By assuming the form of the cluster mass distribution, we verify our knowledge about the cluster structure, in terms of both the structure factor which reflects the radially averaged properties, and effects of rotations, which reflect the anisotropy of the structure. The structure factor is verified with static light scattering, from which the average radius $\overline{R}_g$ is obtained. Using the same value of $\overline{R}_g$, dynamic light scattering provides an independent verification for the structure factor and also probes the anisotropy through the effect of rotations reflected in D_{eff}. In both cases we found that we have to use the results from computer simulations of RLCA clusters. We obtain good agreement with the shape of autocorrelation function over all t measured, even when $q\overline{R}_g>1$, despite the fact that we use only the first cumulant for the individual clusters. This indicates that the effect of rotational diffusion is mainly to shift the effective diffusion coefficient, while introducing negligible curvature in the decay for each cluster. It is therefore the highly polydisperse cluster mass distribution which causes the curvature observed in the autocorrelation functions in Fig. 6.2 and Fig. 6.3.

Finally, we note that the form of the cluster mass distribution assumed with Eq. (6.3), with τ=1.5, is very reasonable since all the data measured are in excellent agreement with the calculations. However, the fits to both $G_2(t)$ and $I(q)$ are not very sensitive to changes in the value of τ. We will show in the next sections that, to unambiguously determine τ, we must use a different type of analysis.

6.5 SCALING OF THE FIRST CUMULANT

As shown in the previous section, we can account for both static and dynamic light scattering measurements from the same sample. However, the aggregation was first stopped for these measurements, with the average cluster

radius $\overline{R}_g$ being not much larger than q^{-1}. In a kinetic aggregation process, not only does the average radius keep growing, but also the whole cluster mass distribution continues to evolve with time. The information about these aggregation kinetics is equally important to characterize the aggregation process. In addition, we have not been able to unambiguously determine the distribution exponent τ from the previous measurements. In this section, we will show that the first cumulant of the autocorrelation function calculated at different aggregation times, t_a, can be scaled onto a single master curve, by taking advantage of the dynamic scaling of the cluster mass distribution. The shape of this master curve depends critically on all the features, in particular the cluster mass distribution, enabling us to determine τ.

The effect of the cluster mass distribution on the light scattering measurements is reflected in the fact that every measured quantity is weighted by the distribution $N(M)$. This weighting is in addition to that due to the scattering intensity of each cluster, $I_M(q) \propto M^2 S(qR_g)$. Both factors contribute a power law weighting and their combination can lead to very subtle effects in the behavior of the light scattering. Thus caution must be exercised in all the calculations. We consider here the first cumulant of the autocorrelation function,

$$\Gamma_1 = -\left.\frac{\partial \ln G_1(t)}{\partial t}\right|_{t=0}.$$

With Eq. (6.10) we can express Γ_1 in terms of $N(M)$, $S(qR_g)$ and D_{eff},

$$\Gamma_1 = q^2 \overline{D}_{eff} = q^2 \frac{\int N(M) M^2 S(qR_g) D_{eff}\, dM}{\int N(M) M^2 S(qR_g) dM}. \qquad (6.13)$$

We can see that besides the q^2 dependence, the first cumulant represents an average effective diffusion coefficient, $\overline{D}_{eff}$. In addition to the rotational effects included in D_{eff}, the effects of the structure factor and the cluster mass distribution

are reflected in the weighting. Generally, $\overline{D}_{\rm eff}$ is a function of q. Therefore, the average hydrodynamic radius will also depend on q, if it is determined as $\overline{R}_{\rm eff}=\zeta/\overline{D}_{\rm eff}$. This additional q dependence reflects the effects of all the features, allowing us to characterize them. In order to determine this q dependence, we first evaluate Eq. (6.11) analytically, in the absence of rotational diffusion. Therefore, we set $D_{\rm eff}=D\approx\zeta/R_{\rm g}$. We assume $N(M)=M^{-\tau}$ up to a cutoff mass $M_{\rm c}$, and simply use the limiting forms of $S(qR_{\rm g})$ at $qR_{\rm g}<<1$ and $qR_{\rm g}>>1$ to approximate its value,

$$S(qR_{\rm g}) = \begin{cases} 1 & qR_{\rm g}\lesssim 1 \\ (qR_{\rm g})^{-d_{\rm f}} & qR_{\rm g}\gtrsim 1 \end{cases} \qquad (6.14)$$

Then we can express the average effective diffusion coefficient as

$$\overline{D}_{\rm eff} = \frac{\zeta}{a}\frac{\int_1^u M^{2-\tau-1/d_{\rm f}}dM + u\int_u^{M_{\rm c}} M^{1-\tau-1/d_{\rm f}}dM}{\int_1^u M^{2-\tau}dM + u\int_u^{M_{\rm c}} M^{1-\tau}dM}. \qquad (6.15)$$

Here, $u=(aq)^{-d_{\rm f}}$ is the mass of a cluster with $R_{\rm g}=q^{-1}$. Physically, this represents the boundary of the two different scattering regimes in Eq. (6.14). As a consequence, $\overline{D}_{\rm eff}$ is seen to be independent of q in two limits: first, if $q<R_{\rm c}^{-1}$, where $R_{\rm c}=aM_{\rm c}^{1/d_{\rm f}}$ is the radius of gyration of the largest cluster, and second, if $q>a^{-1}$. This is shown schematically in Fig. 6.4. In Fig. 6.4(a), we show $\overline{D}_{\rm eff}$ as a function of q, with different curves representing different cutoff masses, $M_{\rm c}$, for the cluster mass distribution. The lowest curve has the largest $M_{\rm c}$. All the curves have three regions: when $q<R_{\rm c}^{-1}$, $\overline{D}_{\rm eff}=\overline{D}$, a constant, which depends only on $M_{\rm c}$ or $R_{\rm c}$; when $q>a^{-1}$, $\overline{D}_{\rm eff}=\overline{D}'$, another constant depending on $M_{\rm c}$, but weighted differently. In between, $\overline{D}_{\rm eff}$ varies with q, and this q dependence depends on the different weighting reflected in $\overline{D}$ and $\overline{D}'$, and on the difference between a and $R_{\rm c}$. For light scattering experiments, the available q range is usually in this intermediate region, where $\overline{D}_{\rm eff}$ depends on q. This makes light scattering a powerful technique to probe colloid aggregation.

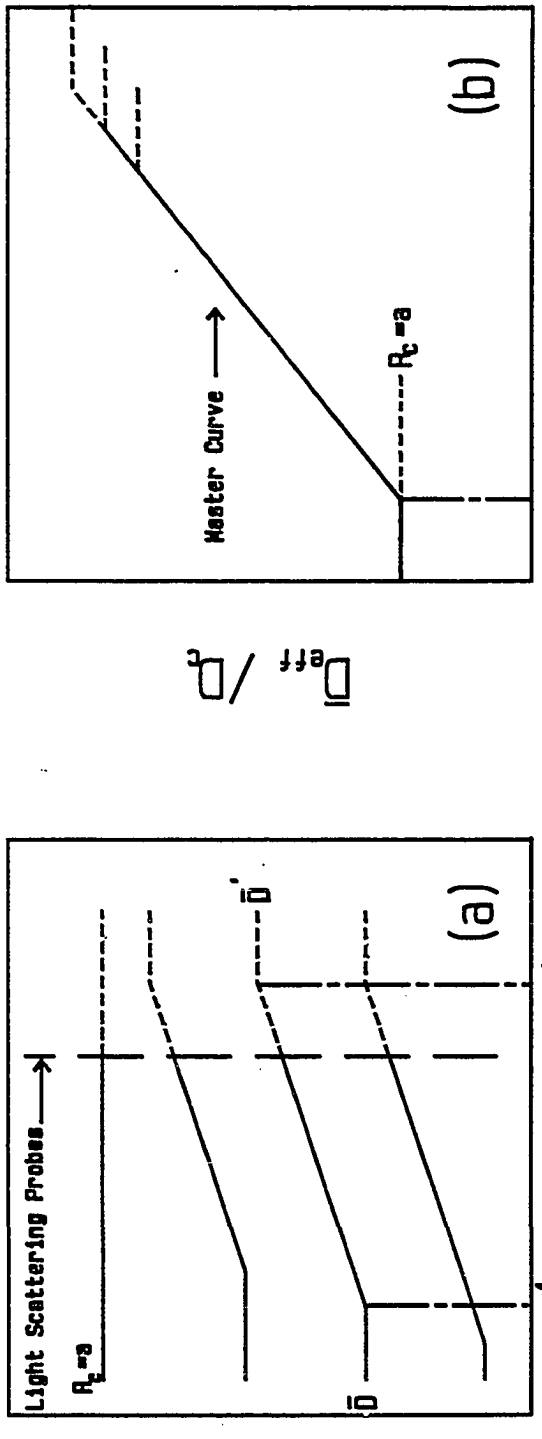

Fig. 6.4 Schematic plots of the average effective diffusion coefficient $D_{eff}=\Gamma_1/q^2$. (a) D_{eff} as a function of q. Different curves represent different cutoff masses M_c of the cluster mass distribution, with the lower curves having larger M_c. Each curve has three regions: for $q<R_c^{-1}$ $D_{eff}=\bar{D}$, the average diffusion coefficient measured in the $q=0$ limit; for $q>a^{-1}$, which light scattering cannot probe, $D_{eff}=\bar{D}'$, another constant independent of q; in between D_{eff} varies with q. Solid parts of the curves represent the range accessible in light scattering experiments. (b) The result after scaling each curve by their cutoff radius R_c. Except for the dashed parts which are not accessible by light scattering, all the curves comprise a master curve as represented by the solid line.

The two constants $\overline{D}$ and $\overline{D}'$, which control the q dependence of $\overline{D}_{\text{eff}}$, can be easily evaluated from Eq. (6.15),

$$\overline{D} = \overline{D}_{\text{eff}}(q<R_c^{-1}) = \frac{\zeta}{a}\frac{\int_1^{M_c} M^{2-\tau-1/d_f} dM}{\int_1^{M_c} M^{2-\tau} dM}, \tag{6.16a}$$

and

$$\overline{D}' = \overline{D}_{\text{eff}}(q>a^{-1}) = \frac{\zeta}{a}\frac{\int_1^{M_c} M^{1-\tau-1/d_f} dM}{\int_1^{M_c} M^{1-\tau} dM}. \tag{6.16b}$$

It should be noticed that all the exponents of the integrands are very close to either zero or -1, when $d_f \approx 2$ and $\tau \lesssim 2$. Mathematically, this means that the integrands are very flat; physically, this means that all the clusters with different masses are weighted almost equally, making $\overline{D}_{\text{eff}}$ and the first cumulant sensitive to the behavior of all clusters probed, independent of their size. As a consequence, no cluster mass is dominant. While the large clusters certainly scatter more light per cluster, the power–law cluster mass distribution pulls the weighting towards the small clusters, so that all the clusters contribute almost equally. In addition, when any of the exponents is close to -1, that integral will depend equally on both limits, which makes the asymptotic limit of $M_c >> 1$ being reached very slowly. Only in that limit, can the q dependence of the average effective diffusion coefficient be simply expressed as $\overline{D}_{\text{eff}} \propto q^{\alpha}$, where $\alpha = 1 - d_f(2-\tau)$ for $2 - 1/d_f \lesssim \tau \lesssim 2$, as was shown by Martin and Leyvraz.[11] However, to reach this asymptotic limit requires that $M_c >> 10^{20}$, which is not achievable experimentally.

Another important feature of the curves shown in Fig. 6.4 is their scaling behavior. The curves in Fig. 6.4(a) do not seem to scale with each other, as they are plotted. This is because there are two length scales that characterize each curve: a and R_c. However, light scattering cannot probe the small length scale, a.

Therefore, the only characteristic length scale actually probed is R_c. Thus, for values of q small enough, we can scale the curves by this length scale, and all the curves will collapse. This is shown schematically in Fig. 6.4(b) where $\overline{D}_{eff}/D_c$ is plotted as a function of qR_c, where $D_c=\zeta/R_c$. The shape of this scaled curve is independent of R_c, and thus independent of the aggregation time t_a. This master curve can be obtained from calculations of different R_c with the experimentally available q range as shown in Fig. 6.4(a), or it can also be calculated with one large R_c, over a wider range of q. Moreover, not only R_c, but also any moment of the distribution with a dimension of length which reflects the time dependence of the distribution can be used to scale the curves. This scaling behavior of the first cumulant is due to the scaling properties of all the quantities involved in Eq. (6.11). It is a direct consequence of the dynamic scaling of the cluster mass distribution, whose shape is unchanged with time, while its moment grows with time. Thus, at different times, dynamic light scattering probes different parts of the distribution. In addition, the fractal scaling of the cluster structure ensures that not only the radially averaged quantity, $S(qR_g)$, can be scaled, but also that the anisotropy of different clusters is self–similar.

We have actually calculated the shape of the master curve numerically using the more realistic forms. Since it depends on clusters of all sizes, we have to use Eq. (6.9) to include the proper behavior around $qR_g=1$ for the structure factor. For the same reason, we need to include rotational effects, for which we use the form of D_{eff} calculated from simulated clusters. For the cluster mass distribution, we again use Eq. (6.3) with the exponential cutoff. Fig. 6.5 is a plot similar to Fig. 6.4, showing the scaling that we have predicted. In the top part of the plot, calculated values of $\overline{D}_{eff}$ using $\tau=1.5$ are plotted as a function of q for (*a*) $M_c=10^4$, (b) $M_c=10^5$ and (c) $M_c=10^6$. As M_c grows, the average diffusion coefficient decreases. Experimentally the range of q accessible by light scattering is 0.003 to 0.03 nm^{-1}.

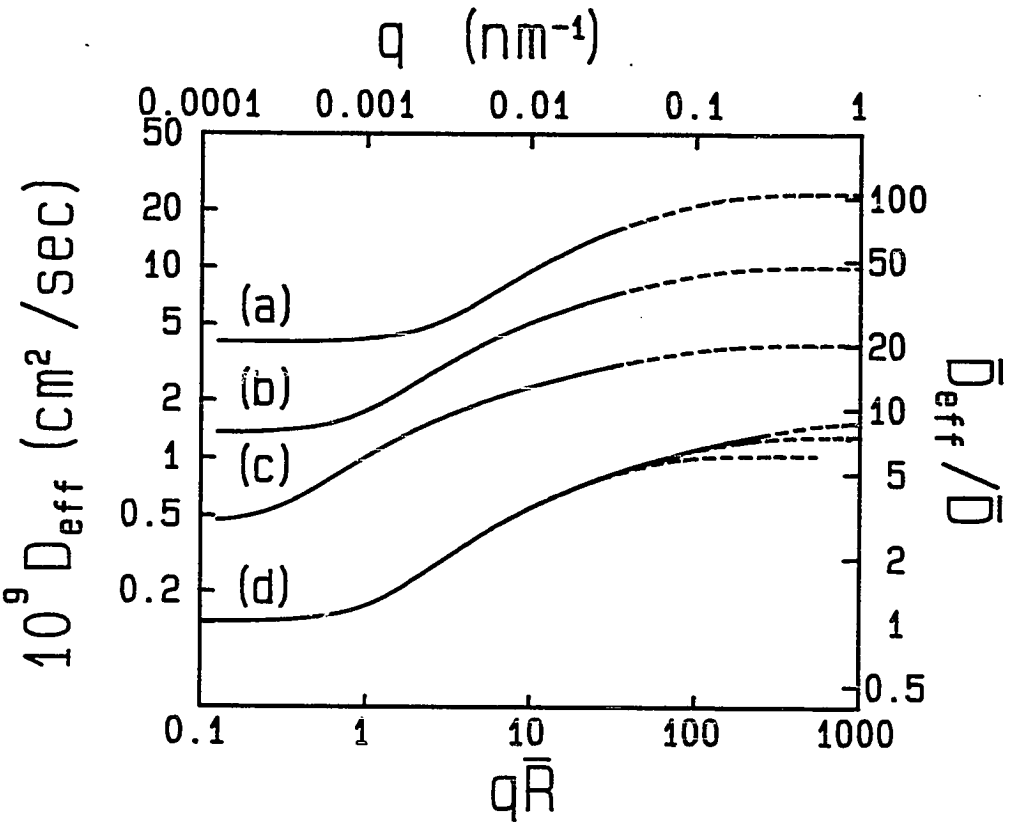

Fig. 6.5 A similar plot to Fig. 6.4, calculated using Eq. (6.13). The top part shows the calculated values of $\bar{D}_{\text{eff}}$ as a function of q, for (a) $M_c=10^4$, (b) $M_c=10^5$ and (c) $M_c=10^6$. The $\bar{D}_{\text{eff}}$ scale is on the left and the q scale is on the top. The experimentally accessible range of q is up to about 0.03 nm^{-1}, after which the curves are represented by dots. The three curves are scaled onto a master curve, (d), as $\bar{D}_{\text{eff}}/\bar{D}$ vs. $q\bar{R}$, whose scales are on the bottom and the right of the plot.

In the bottom part of the plot, curve (d) is the master curve composed of the three upper curves, and obtained by scaling them with the values of $\overline{D}_{\text{eff}}$ measured at q=0, $\overline{D}$, and the corresponding hydrodynamic radius $\overline{R}=\zeta/\overline{D}$. As can be seen, except for the dashed parts, which are not accessible by light scattering, all three curves fall onto a single master curve. We also note that for $q\overline{R}>>100$ all three curves become dashed. However, the master curve there can still be calculated with higher M_c. Therefore, the scaling of the first cumulant, or the average effective diffusion coefficient, provides a way to show the whole shape of the master curve, allowing us to explore the effects of the different features on the dynamic light scattering results.

In Fig. 6.6, we plot our calculations of the master curve using different values of τ, 1.3, 1.5 and 1.7, both with and without including rotational diffusion, to show the sensitivity of the scaling master curve to these effects. For $q\overline{R}<1$, all the curves become indistinguishable from one another. However, as $q\overline{R}$ becomes appreciably larger than 1, the shape of the curves with different values of τ becomes quite different and therefore distinguishable. In addition, the inclusion of the rotational effects is unambiguously reflected in the shape of the curves.

The first cumulant from the dynamic light scattering is a sensitive measure of the cluster mass distribution and rotational effects. The effect of different values of the distribution exponent, τ, can be observed in the q dependence of the master curve. In addition, the shape of the master curve is sensitive to other features, such as the form for the structure factor $S(qR_g)$ and the cutoff form at $M\approx M_c$ for the cluster mass distribution $N(M)$. This makes the master curve an ideal characterization of all these features of the aggregation. In the next section, we compare the calculated master curves with the experimental measurements using colloidal gold.

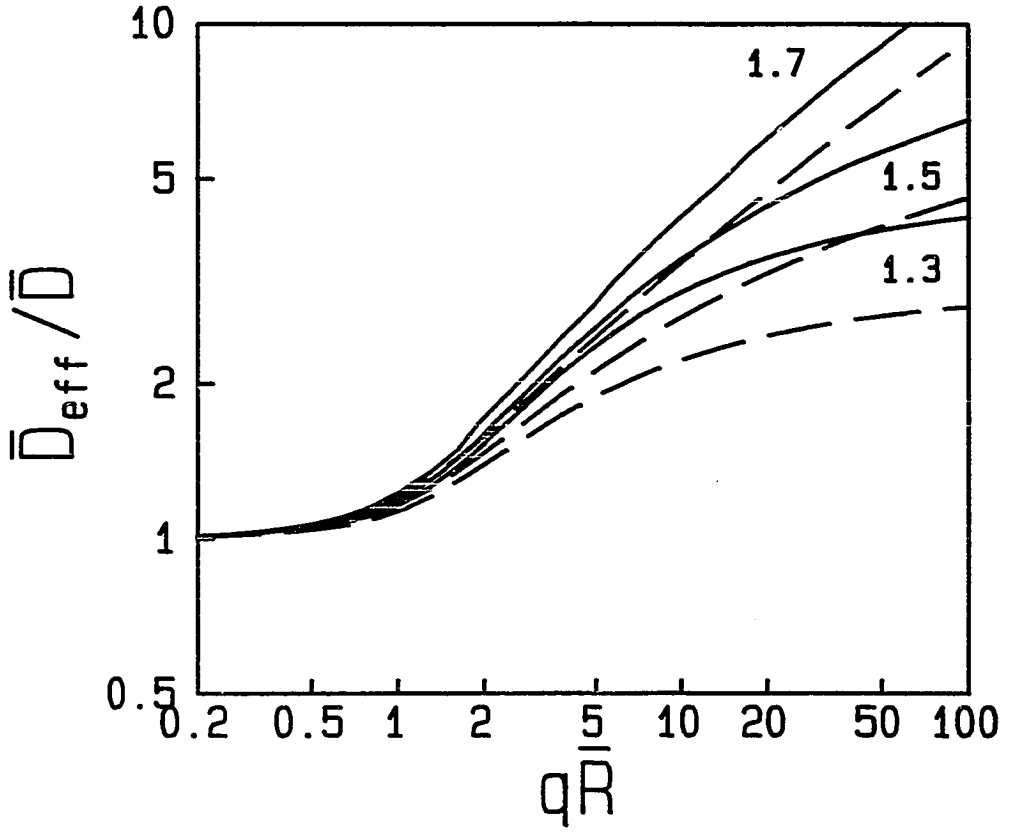

Fig. 6.6 Calculated $\bar{D}_{eff}/\bar{D}$ for several different values of τ, each with (solid curves) and without (dashed curves) including rotational diffusion.

6.6 EXPERIMENTAL RESULTS

The scaling of the experimentally measured data is somewhat different than that done for the calculations. For the calculations, each curve is calculated by choosing a value of $\overline{R}$ to represent the cluster mass distribution at different times, t_a. We then normalize the curves by $\overline{R}$ and by $\overline{D}=\zeta/\overline{R}$, to obtain the complete master curve. Experimentally, the moment $\overline{R}$ is unknown, since we cannot make measurements at sufficiently low q. Instead we interpolate the data measured at both different q and different t_a to obtain a data set of $\overline{D}_{eff}$ at a fixed aggregation time t_a as a function of q. Seven data sets thus obtained are shown in Fig. 6.7 with their t_a labeled. We next scale different data sets onto a single curve, by multiplying the measured $\overline{D}_{eff}$ by $\overline{R}/\zeta$, and multiplying q by $\overline{R}$. A value of $\overline{R}$ is chosen for each data set such that it overlaps with the previous one. With sufficient data, this scaling process is both straightforward and unambiguous. In Fig. 6.8, the final result of this scaling is shown. All the data sets lie on a single master curve, reflecting the scaling behavior of the aggregation, as expected. In the same Figure we include the calculated results from Fig. 6.6, with the rotational effects included, from which, we can determine that $\tau=1.5\pm0.05$. This dynamic light scattering results confirm our previous TEM measurements of the cluster mass distribution,[12] but with much better statistical accuracy. Furthermore the value of τ is in excellent agreement with the theoretical prediction based on the Smoluchowski equations.[8]

We can also determine the kinetics of the aggregation from the scaling of the master curve. The scaling factor $\overline{R}$, is the true average hydrodynamic radius as would be measured in the small q limit. We plot $\overline{R}$ as a function of t_a in a semi–logarithmic scale in Fig. 6.9. The linear behavior indicates that $\overline{R} \sim e^{t_a/t_0}$, so that the average hydrodynamic radius grows exponentially. This is also in agreement with the prediction from the solution of the Smoluchowski equations.[8]

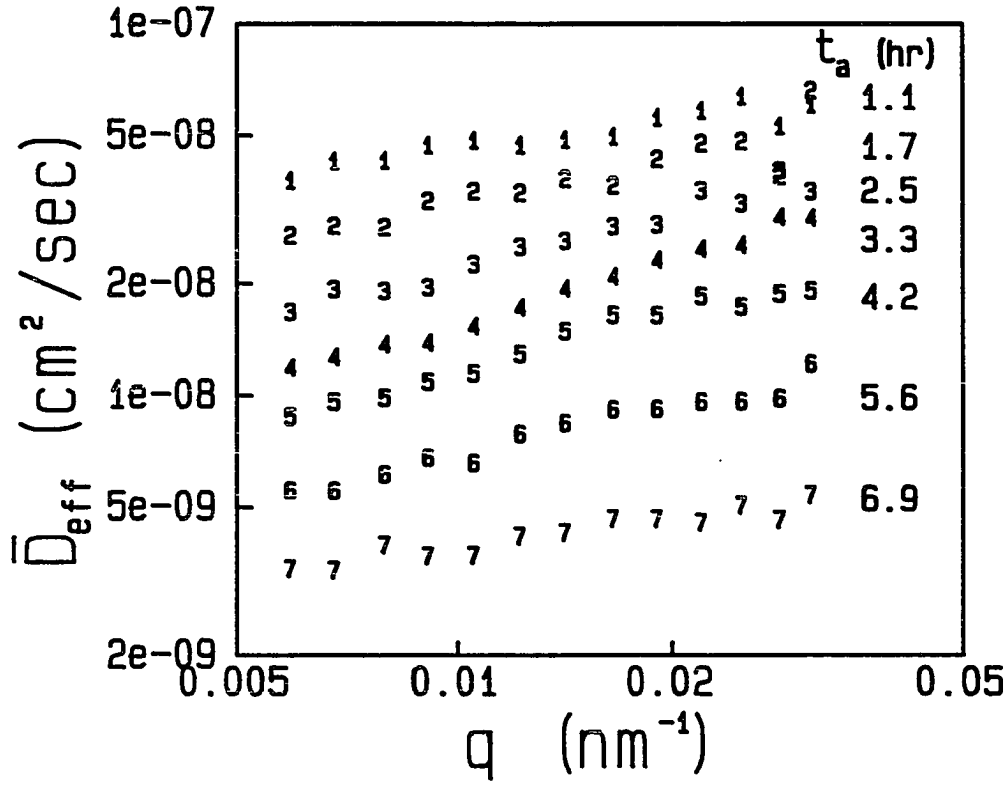

Fig. 6.7 Measured data of D_{eff} as a function of q, taken at different times t_a.

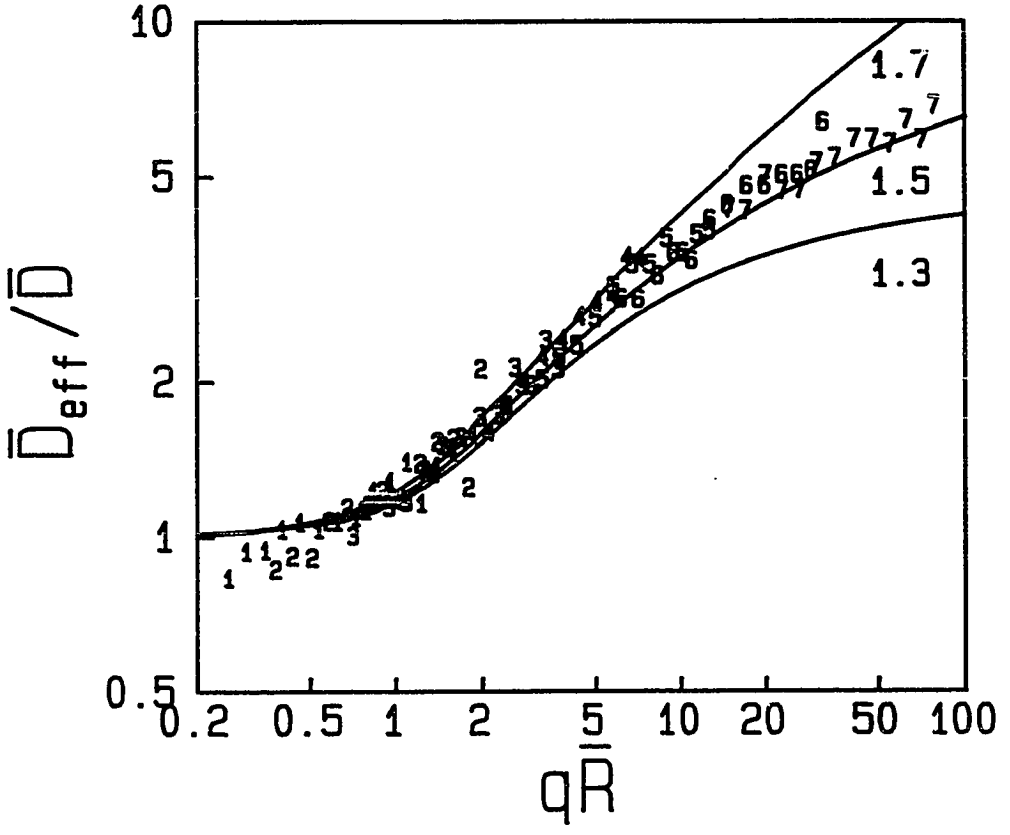

Fig. 6.8 Data from Fig. 6.7 scaled onto a master curve, by multiplying each of them by a factor of $\bar{R}/\zeta$, and plotted as a function of $q\bar{R}$. An $\bar{R}(t_a)$ is obtained for each data set such that it overlaps with the others. The solid curves are the same as those shown in Fig. 6.6 with rotational effects included, for comparison with the data.

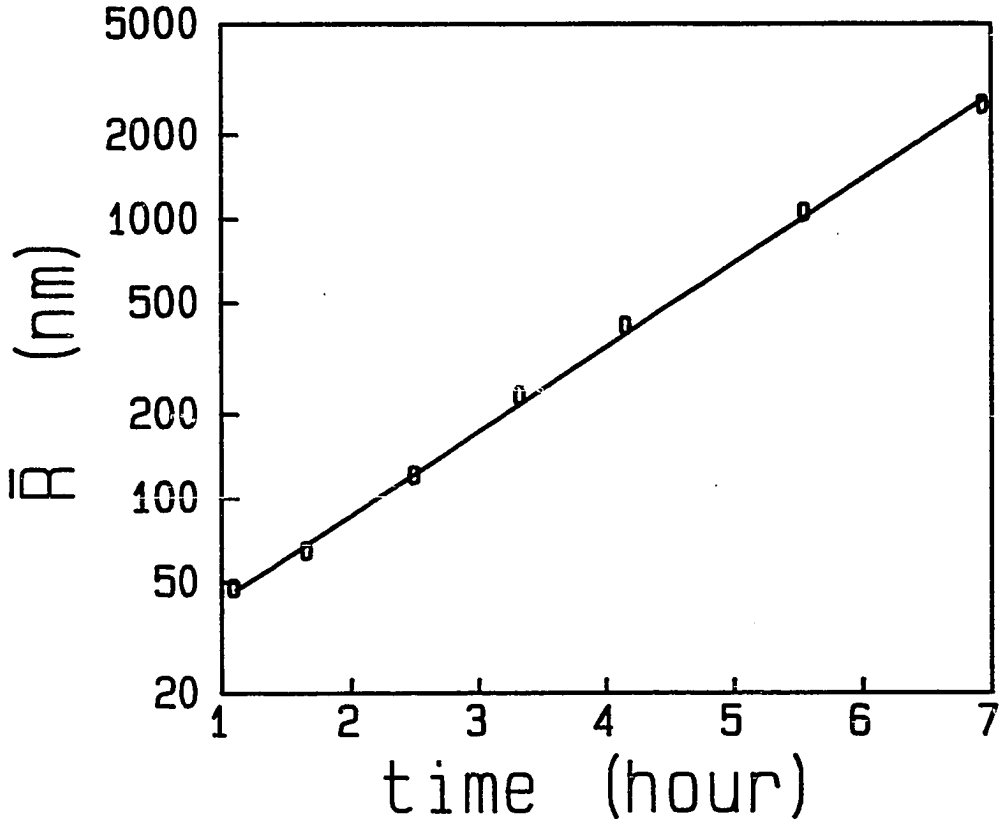

Fig. 6.9 The scaling factor $\overline{R}$ as a function of aggregation time t_a obtained from the scaling operation of Fig. 6.8. $\overline{R}$ represent the hydrodynamic radius measured at q=0 limit. The solid line is a fit giving an exponential form for the aggreagation kinetics.

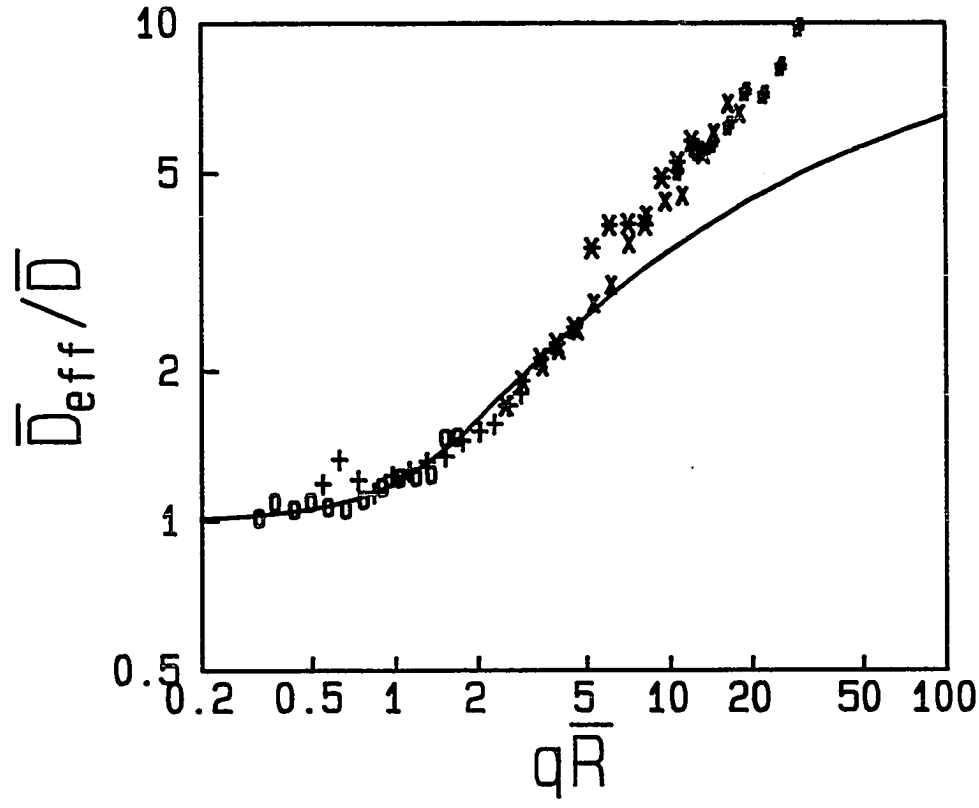

Fig. 6.10 Master curve obtained for gold RLCA aggregates with sedimentation effect due to gravity. The differential settling rates of the clusters change the cluster mass distribution, leading to the change in shape of the master curve. The calculated shape without gravitational settling is shown for comparison by the solid curve.

We note here that caution must be exercised to achieve a true RLCA process experimentally, so that the results can be compared with the calculations of the theoretical model. For example, if there is differential sedimentation due to gravity during the measurements, whose effects the model does not include, the scattering results can be markedly different when compared with the calculations. As discussed in Section 3, the cluster mass distribution can change substantially over the several hours required for an RLCA experiment. The measured data can still be scaled onto a master curve, as shown in Fig. 6.10, which was taken without inverting the sample cell every 15 minutes to remove the effects of differential sedimentation in an aggregation of colloidal gold. However, it does not curve over at large $q\overline{R}$, and has a higher asymptotic slope about α=0.7, and we cannot fit the data using calculations based upon RLCA model.

6.7 UNIVERSAL BEHAVIOR OF COLLOID AGGREGATION

So far we have used only colloidal gold, since RLCA has been well studied for colloidal gold, and its important features are known. However, RLCA, as a limiting and universal regime, should be applicable to other colloid system as well. To test this, one has to prove that the aggregation process has the same cluster mass distribution, the same kinetics, and produces clusters with the same structure as those predicted by RLCA. The scaling of $\overline{D}_{\text{eff}}/\overline{D}$ onto master curves provides a method to directly compare the behavior of completely different colloids. Since the shape of the master curve is very sensitive to the features of the aggregation, dynamic light scattering can be used as a critical test of its behavior. In addition, static light scattering can be used to compare the fractal dimension and the structure factor of different colloids. Therefore, using light scattering techniques, we are able to demonstrate the universal behavior of colloid aggregation, and in addition verify the universality of the theoretically proposed RLCA model.

To examine this, we choose three very different colloids: gold, silica and polystyrene latex. Each is comprised of a different material, each is stabilized by different functional groups, each is aggregated by different methods and each forms completely different interparticle bonds upon aggregation. However, each of them can be destabilized to obtain either $E_b << k_B T$ or $E_b \gtrsim k_B T$, allowing both DLCA and RLCA regimes to be investigated.

The colloidal gold has a particle radius of a=7.5 nm, and a volume fraction of $\phi_0 = 2.8 \times 10^{-6}$. The colloid is initially stabilized by surface adsorbed citrate ions. Aggregation is initiated by adding pyridine, which is adsorbed on the surface of the particles, displacing the citrate ions and reducing the stabilizing surface charges. The amount of pyridine added determines whether the aggregation is diffusion or reaction–limited. For RLCA, the final concentration of pyridine was 10^{-5} M. The interparticle bonds of aggregates are most likely metallic.

The colloidal silica used is Ludox–SM, obtained from DuPont. It consists of particles with a=3.5 nm and was diluted into two samples, one with $\phi_0 = 1.0 \times 10^{-3}$, the other $\phi_0 = 1.0 \times 10^{-5}$ for the experiments. The colloid is initially stabilized by SiO^- groups on the surface of the particles. The pH was adjusted to $\geq$11 by addition of NaOH to provide enough OH^- ions needed to catalyze the formation of particle bonds. Aggregation was then initiated by addition of NaCl, which decreases the Debye–Hückel screening length, reducing the the repulsive barrier between the particles. The final salt concentration was 0.6 M. The interparticle bonds of the aggregates are believed to be siloxane bonds. For the sample with an initial volume fraction of $\phi_0 = 1.0 \times 10^{-3}$, we aggregated it up to about $\overline{R}$=0.5 micron, when gelation is still far away. The high concentration of colloidal particles increases the scattering intensity of the clusters when their size is still small compared with q^{-1}. This enables us to take reliable data at early times of the aggregation, when $q\overline{R}<1$. For the other sample, with $\phi_0 = 1.0 \times 10^{-5}$, the data is not used until $q\overline{R} \approx 1$, but the

aggregation can continue until $\overline{R}\approx 5$ microns without approaching gelation.

The polystyrene latex used had a=19 nm and was diluted to $\phi_0=6.7\times10^{-6}$. This colloid is stabilized by charged carboxylic acid groups on their surface. Aggregation was initiated by adding NaCl to a concentration of 0.2 M which decreases the Debye–Hückel screening length. The interparticle bond of the aggregates are due to Van der Waals interactions and steric entanglements.

As aggregation proceeded, data were taken repeatedly as a function of q by changing the angle of the detector. Caution was exercised to avoid differential sedimentation effects. Master curves were obtained for each colloid following the procedures described in the previous section. The kinetics were determined from the time dependence of the scaling parameter, $\overline{R}$. In addition, the static light scattering intensity was measured concurrently allowing the fractal dimension to be determined independently.

The normalization in the master curves removes all features specific to the individual colloids from the scaling curves. Thus there is no remaining adjustable parameters and they can be compared directly. In Fig. 6.11, we plot the three scaling curves obtained from the different colloids. The squares represent data from colloidal gold, the crosses represent data from colloidal silica, and the triangles represent data from polystyrene latex. The shape of all curves representing different colloids are indistinguishable. This is a strong evidence in support of the universality of RLCA. In addition, the behavior of the master curve is well predicted by the RLCA model, as shown by the solid curve which is the calculated master curve using τ=1.5. Furthermore, the static scattering from each colloid is also identical, as shown in Fig. 6.12. The three symbols (square, cross and triangle) represent the same colloids as before, and all the data were measured concurrently with the dynamic light scattering data when $q\overline{R}>1$. The measured fractal dimensions are: d_f=2.10 for gold, d_f=2.12 for silica, and d_f=2.13 for polystyrene.

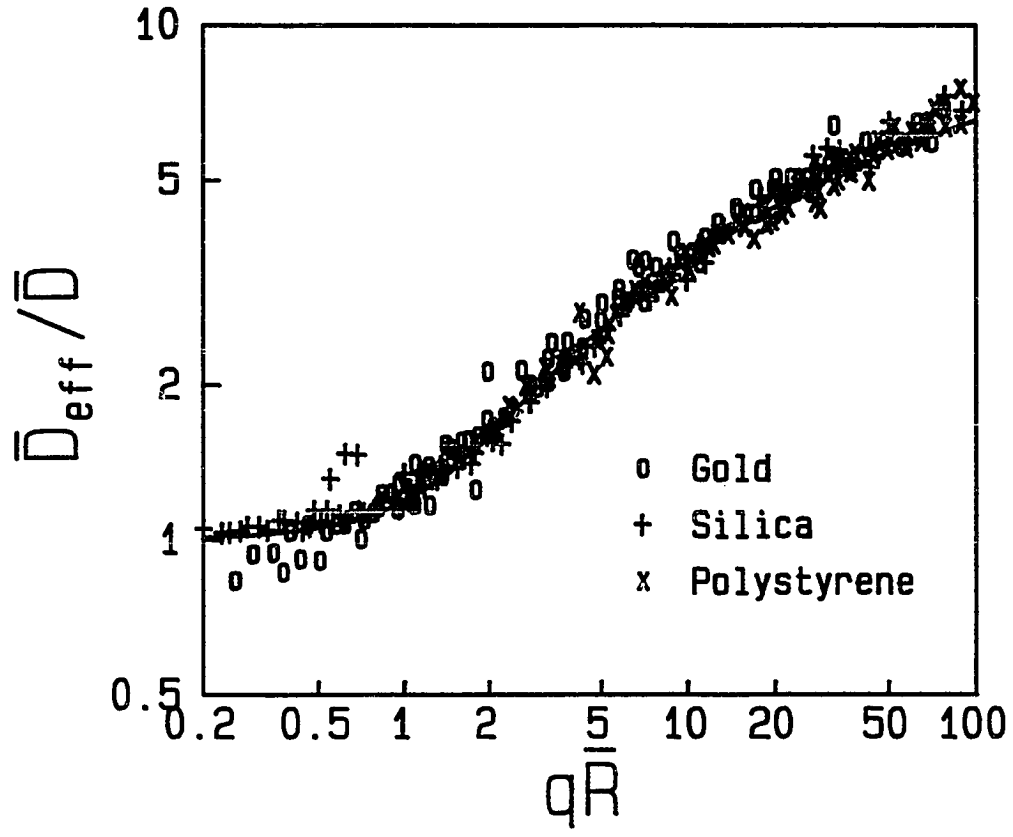

Fig. 6.11 Master curves for gold (o), silica (+), and polystyrene (×) for RLCA. The solid curve is the calculation with τ=1.5.

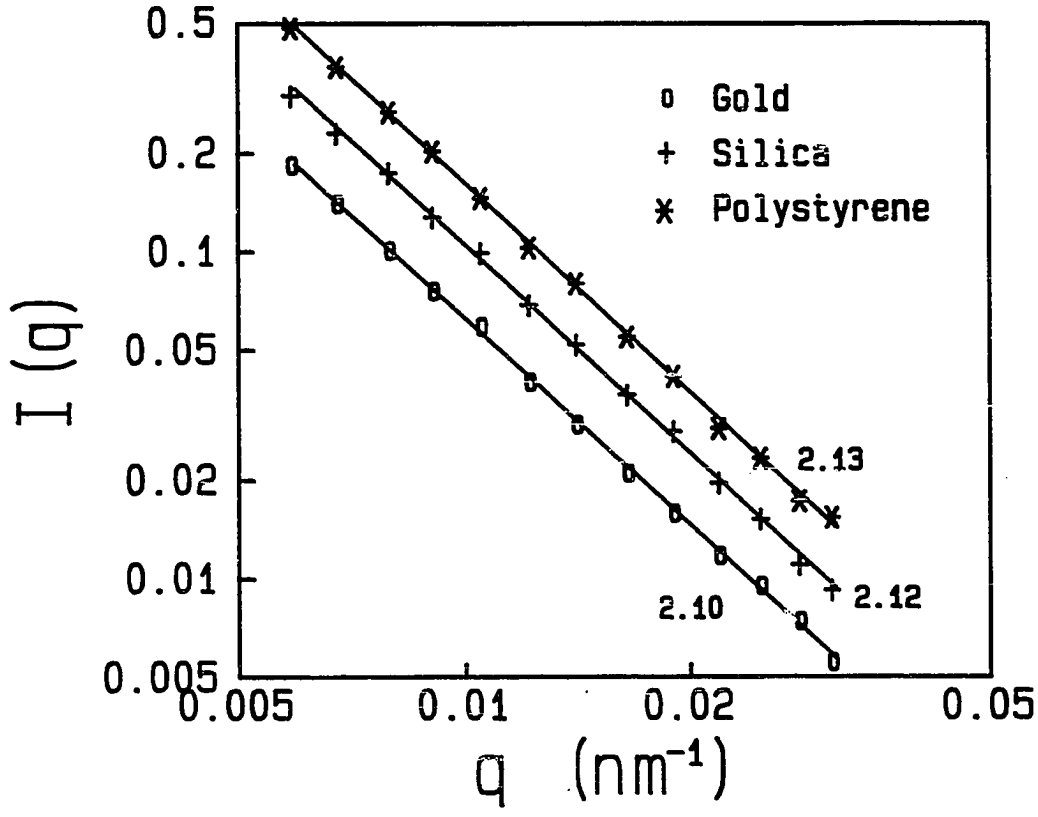

Fig. 6.12 Static light scattering from RLCA aggregates of gold (o), silica (+) and polystyrene (*). The measured fractal dimensions are: gold, d_f=2.10; silica, d_f=2.12; and polystyrene, d_f=2.13.

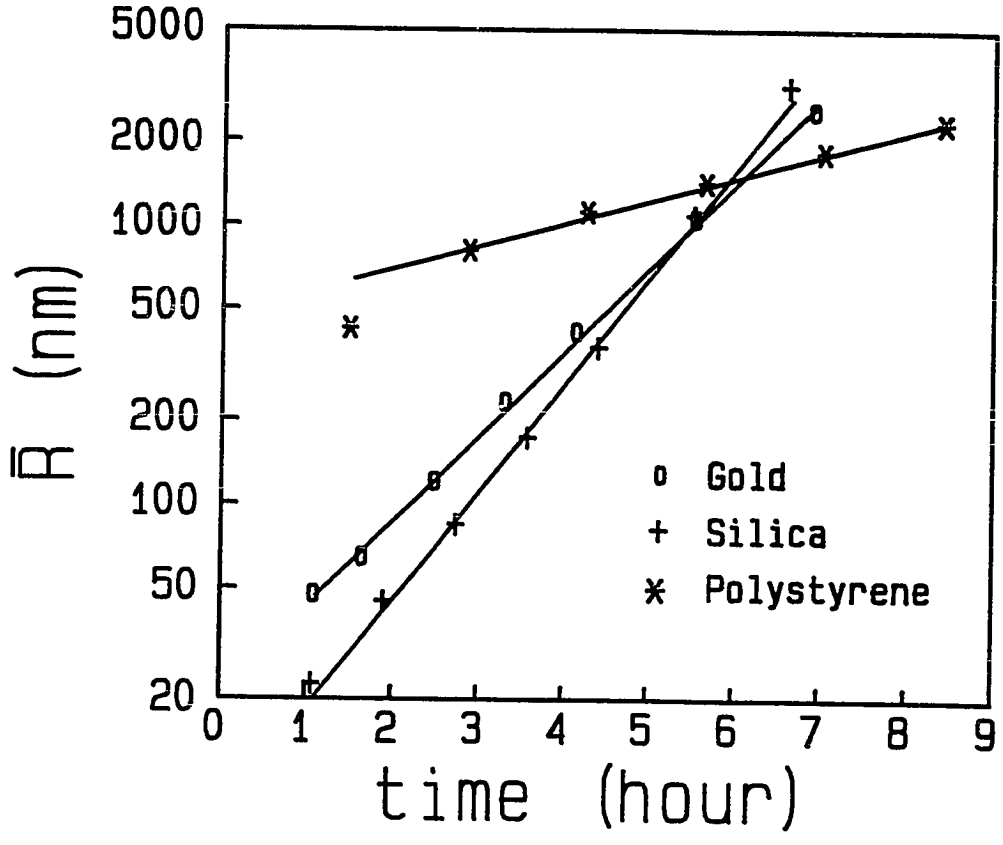

Fig. 6.13 Kinetics of RLCA aggregation for gold (o), silica (+) and polystyrene (*). The scale of $\overline{R}$ is logarithmic to show the exponential growth.

To within experimental error, these are identical, yielding $d_f \approx 2.11 \pm 0.02$ for all three colloids.

The growth kinetics of each colloid also had the same behavior, as shown in Fig. 6.13. The radius $\overline{R}$ obtained from the scaling is plotted as function of aggregation time t_a. All three colloids had an exponential growth, $\overline{R} \sim e^{t_a/t_0}$. The colloidal silica data were taken with the first sample, and it stops at $\overline{R} \approx 500$ nm. The different slopes show that they had different time constant t_0, which were determined by their initial sticking probability P and the particle concentration N_0.

The identical behavior of all the data shown for the different colloids provides striking evidence of the universality of the aggregation in RLCA regime. The existence of the master scaling curve is the consequence of the scaling properties of the aggregate structure, of the anisotropy of their structure, and the dynamic scaling of the cluster mass distribution. In addition, the shape of each scaling curve depends critically on the details of these features. The fact that the scaling curves have identical shape for each colloid implies that each of these features is identical, and is independent of the chemical details of the individual colloids. This therefore lends very strong support to the concept of the universal nature of reaction–limited colloid aggregation.

6.8 CONCLUSIONS

In this chapter, the process of reaction–limited colloid aggregation is studied using static and dynamic light scattering. We show that both scattering techniques can provide a measure of the aggregation process. We present a self–consistent description of static and dynamic light scattering from colloidal aggregates. Assuming a form of the cluster mass distribution, we determine the structure factor of the aggregates, and the effects of their rotational diffusion from the scattering results. By properly including these effects, our calculations are in excellent

agreement with the measurements. We have also measured the ratio of the hydrodynamic radius to the radius of gyration of individual clusters, giving β=1.0 for RLCA aggregates.

We study the effects of the power–law cluster mass distribution obtained in RLCA. The effects cause the dynamic scattering results to be sensitive to the behavior of clusters of all sizes. The q dependence of the first cumulant of the autocorrelation function cannot be simply expressed as $\Gamma_1 \sim q^{2+\alpha}$. Instead, the shape of the function $D_{\text{eff}}(q)=\Gamma_1/q^2$, depends critically on all the key features of the aggregation process: the distribution exponent τ, the effects of rotational diffusion, and the shape of the structure factor. A method is developed to scale the measured data onto a master curve, whose shape represents the whole q dependence in D_{eff}. In addition, the aggregation kinetics are obtained from the scaling. The master curves obtained from three completely different colloids: gold, silica, and polystyrene are all identical. This implies that each of these features is identical for the colloids: the cluster mass distribution, the structure factor, and the cluster anisotropy. The exponent obtained is τ=1.5±0.05; the aggregation kinetics all exhibit an exponential growth; and the fractal dimension measured by static light scattering is $d_f \approx 2.1$ for the colloids. These are in good agreement with the theoretical predictions of the RLCA model. These results provide striking evidence of the universality of colloid aggregation, and confirm that RLCA is a universal regimes.

REFERENCES

[1]D. W. Schaefer, J. E. Martin, P. Wiltzius and D. S. Cannell, *Phys. Rev. Lett.* **52**, 2371 (1984).

[2]D. A. Weitz, J. S. Huang, M. Y. Lin and J. Sung, *Phys. Rev. Lett.* **54**, 1416 (1985).

[3]M. Matsushita, Y. Hayakawa, K. Sumida and Y. Sawada, in *Proceeding of the First International Conference for Science on Form*, ed. Y. Kato and J. Toriwaki (KTK Scientific Publishers, Tokyo, 1986).

[4]J. S. Huang, J. Sung, M. Eisner, S. C. Moss and J. Gallas, *J. Chem. Phys.*, to appear.

[5]W. D. Brown and R. C. Ball, *J. Phys.* **A18**, L517 (1985).

[6]P. G. J. Van Dongen and M. H. Ernst, *Phys. Rev. Lett.* **54**, 1396 (1985).

[7]R. C. Ball, D. A. Weitz, T. A. Witten and F. Layvraz, *Phys. Rev. Lett.* **58**, 274 (1985).

[8]P. Meakin and F. Family, *Phys. Rev.* **A36**, 5498 (1987).

[9]Von Schultess, G. B. Benedek and R. W. de Blois, *Macromolecules*, **13**, 939 (1980).

[10]J. E. Martin and D. W. Schaefer, *Phys. Rev. Lett.* **53**, 2457 (1984).

[11]J. E. Martin and F. Layvraz, *Phys. Rev.* **A34**, 2346 (1986).

[12]D. A. Weitz and M. Y. Lin, *Phys. Rev. Lett.* **57**, 2037 (1986); or Chapter 3, this volume.

[13]P. Wiltzius, D. S. Cannell, D. W. Schaefer and J. E. Martin, *Bull. Am. Phys. Soc.* **30**, 268 (1985).

[14]D. A. Weitz, M. Y. Lin and J. S. Huang, in *Physics of Complex and Supermolecular Fluids*, ed. S. A. Safran and N. A. Clark (Wiley–Interscience, New York, 1987); also Chapter 2, this volume.

[15]For a general discussion of dynamic light scattering, see, e.g., B. J. Berne and R. Pecora, *Dynamic Light Scattering* (Wiley–Interscience, New York, 1976).

[16]see Chapter 4, this volume.

[17]G. Dietler, C. Aubert, D. S. Cannell and P. Wiltzius, *Phys. Rev. Lett.* **57**, 3117 (1986).

[18]E. Jakeman, in *Photon Correlation and Light Beating Spectroscopy*, ed. H. Z. Cummins and E. R. Pike (plenum, New York, 1974).

[19]H. M. Lindsay, R. Klein, D. A. Weitz, M. Y. Lin and P. Meakin, *Phys. Rev.* **A38**, 2614 (1988).

[20]see Chapter 5, this volume.

[21]R. C. Ball, D. A. Weitz and M. Y. Lin, unpublished.

[22]Z.–Y. Chen, P. Meakin and J. M. Deutch, *Phys. Rev. Lett.* **59**, 2121 (1987).

[23]P. Wiltzius, *Phys. Rev. Lett.* **58**, 710 (1987).

[24]P. N. Pusey, J. G. Rarity, R. Klein and D. A. Weitz, *Phys. Rev. Lett.* **59**, 2122 (1987).

Bibliography

Aubert, C and D. S. Cannell, *Phys. Rev. Lett.* **56**, 738 (1986).

Ball, R. C., D. A. Weitz, T. A. Witten and F. Layvraz, *Phys. Rev. Lett.* **58**, 274 (1987).

Berne, B. J. and R. Pecora, *Dynamic Light Scattering* (Wiley, New York, 1976).

Botet, R. and R. Jullien, *J. Phys. A: Math. Gen.* **17**, 2517 (1984).

Brown, W. D. and R. C. Ball, *J. Phys.* **A18**, L517 (1985).

Chandrasekhar, S., *Rev. Mod. Phys.* **15**, 1 (1943).

Chen, Z.–Y., P. Meakin and J. M. Deutch, *Phys. Rev. Lett.* **59**, 2121 (1987).

Cohen, R. J. and G. B. Benedek, *J. Phys. Chem.* **86**, 3696 (1982).

Creighton, J. A., C. G. Blatchford and M. G. Albrecht, *J. Chem. Soc. Faraday Trans. II* **75**, 790 (1979).

DeGennes, P. G., *Scaling Concepts in Polymer Physics* (Cornell Univ. Press, Ithaca NY, 1979).

Dietler, G., C. Aubert, D. S. Cannell and P. Wiltzius, *Phys. Rev. Lett.* **57**, 3117 (1986).

Dimon, P., S. K. Sinha, D. A. Weitz, C. R. Safinya, G. S. Smith, W. A. Varady and H. M. Lindsay, *Phys. Rev. Lett.* **57**, 595 (1986).

Enustun, B. V. and J. Turkevitch, *J. Am. Chem. Soc.* **85**, 3317 (1963).

Family, F. and D. P. Landau, editors, *Kinetic Aggregation and Gelation* (Elsevier, Amsterdam, 1984).

Faraday, M., *Phil. Trans. Roy. Soc.* London **A147**, 145 (1857).

Freltoft, T., J. K. Kjems and S. K. Sinha, *Phys. Rev.* **B33**, 269 (1986).

Friedlander, S. K. and C. S. Wang, *J. Coll. Interface Sci.* **22**, 126 (1966).

Hess, W., H. L. Frisch and R. Klein, *Z. Phys.* **B64**, 65 (1986). In Eq. (14) of this paper, the 4 should be replaced by 2.

Horisberger, M., *Gold Bull.* **14**, 90 (1981).

Huang, J. S., J. Sung, M. Eisner, S. C. Moss and J. Gallas, *J. Chem. Phys.* (1989), to appear.

Hurd, A. J. and W. L. Flower, *J. Colloid Interface Sci.*, **122**, 178 (1988).

Jakeman, E., in *Photon Correlation and Light Beating Spectroscopy*, ed. H. Z. Cummins and E. R. Pike (Plenum, New York, 1974).

Jullien, R., M. Kolb and R. Botet, in *Kinetics of Aggregation and Gelation*, ed. F. Family and D. P. Landau (Elsevier, Amsterdam 1984) p. 101.

Jullien, R., M. Kolb and R. Botet, *J. Phys. Lett.* (Paris) **45**, L211 (1984).

Kantor, Y. and T. A. Witten, *J. Phys. Lett.* **45**, L675 (1984).

Kirchner, F. and R. Zsigmondy, *Ann. Physik* **15**, 573 (1904).

Kolb, M., R. Botet and R. Jullien, *Phys. Rev. Lett.* **51**, 1123 (1983).

Kolb, M., *Phys. Rev. lett.* **53**, 1653 (1984).

Leyvraz, F., *Phys. Rev.* **A29**, 854 (1984).

Lindsay, H. M., R. Klein, D. A. Weitz, M. Y. Lin and P. Meakin, *Phys. Rev.* **A38**, 2614 (1988).

Lindsay, H. M., R. Klein, D. A. Weitz, M. Y. Lin and P. Meakin, to appear in *Phys. Rev.* **A** (1989).

Mandelbrot, B. B., *The Fractal Geometry of Nature* (Freeman, San Francisco, 1982).

Martin, J. E. and D. W. Schaefer, *Phys. Rev. Lett.* **53**, 2457 (1984).

Martin, J. E. and B. J. Ackerson, *Phys. Rev.* **A31**, 1180 (1985).

Martin, J. E. and F. Layvraz, *Phys. Rev.* **A34**, 2346 (1986).

Matsushita, M., Y. Hayakawa, K. Sumida and Y. Sawada, in *Proceeding of the First International Conference for Science on Form*, ed. Y. Kato and J. Toriwaki (KTK Scientific Publishers, Tokyo, 1986).

Meakin, P., *Phys. Rev. Lett.* **51**, 1119 (1983).

Meakin, P., Z.–Y. Chen and J. M. Deutch, *J. Chem. Phys.* **82**, 3786 (1985).

Meakin, P., T. Vicsek and F. Family, *Phys. Rev.* **B31**, 564 (1985).

Meakin, P. and F. Family, *Phys. Rev.* **A36**, 5498 (1987).

Meakin, P., in *Phase Transitions* **12**, ed. J. L. Liebowitz (Academic Press, New York, 1988).

Mie, G., *Ann. Physik* **25**, 377 (1908).

Mountain, R. G. and G. W. Mulholland, preprint.

Overbeek, J. T. G., *J. Coll. Interface. Sci.* **58**, 408 (1977).

Pefferkorn, E., C. Pichot and R. Varoqui, *J. Phys.* (France), **49**, 983 (1988).

Pusey, P. N., J. G. Rarity, R. Klein and D. A. Weitz, *Phys. Rev. Lett.* **59**, 2122 (1987).

Reerink, H. and J. T. G. Overbeek, *Discuss. Faraday Soc.* **18**, 74 (1954).

Schaefer, D. W., J. E. Martin, P. Wiltzius and D. S. Cannell, *Phys. Rev. Lett.* **52**, 2371 (1984).

Sinha, S. K., T. Freltoft and J. Kjems, in *Kinetic Aggregation and Gelation*, ed. F. Family and D. P. Landau (Elsevier, Amsterdam 1984) p. 87.

Turkevich, J., P. C. Stevenson and J. Hillier, *Trans. Discuss. Faraday Soc.* **11**, 55 (1951).

Verwey, E. J. W. and J. T. G. Overbeek, *Theory of the Stability of Lyophobic Colloids* (Elsevier, Amsterdam, 1948).

Van Dongen, P. G. J. and M. H. Ernst, *Phys. Rev. Lett.* **54**, 1396 (1985).

Vicsek, T. and F. Family, *Phys. Rev. Lett.* **52**, 1669 (1984).

Von Schulthess, G. K., G. B. Benedek and R. W. DeBlois, *Macromolecules* **13**, 939 (1980).

Von Smoluchowski, M., *Phys. Z.* **17**, 593 (1916).

Weitz, D. A. and J. S. Huang, in *Kinetics of Aggregation and Gelation*, ed. F. Family and D. P. Landau (Elsevier, Amsterdam 1984) p. 19.

Weitz, D. A. and M. Oliveria, *Phys. Rev. Lett.* **52**, 1433 (1984).

Weitz, D. A., J. S. Huang, M. Y. Lin and J. Sung, *Phys. Rev. Lett.* **53**, 1657 (1984).

Weitz, D. A., M. Y. Lin and C. J. Sandroff, *Surf. Sci.* **158**, 147 (1985).

Weitz, D. A., J. S. Huang, M. Y. Lin and J. Sung, *Phys. Rev. Lett.* **54**, 1416 (1985).

Weitz, D. A. and M. Y. Lin, *Phys. Rev. Lett.* **57**, 2037 (1986).

Weitz, D. A., M. Y. Lin and J. S. Huang, in *Physics of Complex and Supermolecular Fluids*, ed. S. A. Safran and N. A. Clark (Wiley–Interscience, New York, 1987).

Wiltzius, P., D. S. Cannell, D. W. Schaefer and J. E. Martin, *Bull. Am. Phys. Soc.* **30**, 268 (1985).

Wiltzius, P., *Phys. Rev. Lett.* **58**, 710 (1987).

Witten, T. A. Jr., and L. M. Sander, *Phys. Rev. Lett.* **47**, 1400 (1981).